Non-Hermitian Structures in Soft Matter

by

Abhijeet Melkani

A dissertation accepted and approved in partial fulfillment of the
requirements for the degree of
Doctor of Philosophy
in Physics

Dissertation Committee:
John Toner, Chair
Jayson Paulose, Advisor
Benjamín Aleman, Core Member
Laura Fredrickson, Institutional Representative

University of Oregon
Summer 2024

DISSERTATION ABSTRACT

Abhijeet Melkani

Doctor of Philosophy in Physics

Title: Non-Hermitian Structures in Soft Matter

Among the major advances in theoretical condensed matter physics in the past twenty years was to characterize topological insulators using the symmetry classes of Hermitian operators. These advancements were applied to various soft matter systems such as mechanical networks where they revealed the presence of topologically protected zero-frequency edge modes. They were also extended to Floquet operators (which occur in non-equilibrium settings) and non-Hermitian operators (occurring in systems with non-reciprocal couplings or subject to external gain/loss). In classical settings, such as in soft matter, non-Hermitian operators are ubiquitous and have revealed rich behavior such as odd elasticity/viscosity, skin effect, and nonreciprocal transitions across a variety of phenomenological systems.

This dissertation deals with using non-Hermitian physics to understand collective behavior in soft matter systems.

First, we consider a localization-to-delocalization phase transition when shear is applied to thermally fluctuating directed polymer chains. These chains cannot cross each other and are placed on a substrate consisting of a periodic arrangement of vertical grooves. We will characterize this phase transition using the properties of the diffusion operator governing the polymer configurations—this operator becomes non-Hermitian at nonzero shear.

Second, we consider networks of classical mechanical oscillators with spring stiffnesses that are modulated in a time-periodic manner. We find the conditions

for parametric resonance and one-way amplification to arise in these networks using the symmetries of the non-Hermitian Floquet operator governing the equations of motion. Specifically, we shall show how a clockwise moving wave in a ring of oscillators can be amplified while the counter-clockwise moving mode remains unamplified.

In investigating these physical systems, we also developed some techniques which are widely applicable. Specifically, we developed a formulation to study systems that are invariant after a combined translation in both space and time. Compared to conventional Floquet techniques, this formulation involves integration of the system dynamics for shorter periods avoiding extraneous degeneracies of eigenvalues. We also characterized the real-to-complex eigenvalue transition in parametrized pseudo-Hermitian matrices which is typically accompanied by a drastic change in the behavior of the underlying system.

This dissertation contains previously published as well as unpublished co-authored materials.

CURRICULUM VITAE

NAME OF AUTHOR: Abhijeet Melkani

GRADUATE AND UNDERGRADUATE SCHOOLS ATTENDED:

University of Oregon, Eugene, OR, USA
Indian Institute of Technology Bombay, Mumbai, Maharashtra, India

DEGREES AWARDED:

Doctor of Philosophy, Physics, 2024, University of Oregon
Master of Science, Physics, 2022, University of Oregon
Bachelor of Technology (Honours), Engineering Physics, 2019, Indian Institute of Technology Bombay

AREAS OF SPECIAL INTEREST:

Statistical physics & soft active matter
Information theory & machine learning
Geometry & topology

PROFESSIONAL EXPERIENCE:

Graduate Research Assistant, University of Oregon, 2019 – 2024
Graduate Teaching Assistant, University of Oregon, 2019 – 2024

GRANTS, AWARDS AND HONORS:

Sushil Jajodia Indian Student Scholarship, University of Oregon, 2023

PUBLICATIONS:

A. Melkani & J. Paulose, *Phys. Rev. E* **110**, 015003 (2024)

A. Melkani, *Phys. Rev. Res.* **5**, 023035 (2023)

A. Melkani, A. Patapoff, & J. Paulose, *Phys. Rev. E* **107**, 014501 (2023)

A. Melkani & S. J. van Enk, *Phys. Rev. Res.* **3**, 033060 (2021)

A. Melkani, C. Gneiting, & F. Nori, *Phys. Rev. A* **102**, 022412 (2020)

ACKNOWLEDGEMENTS

I thank my advisor Jayson Paulose for his mentorship and for supporting me, academically and otherwise, through the difficult phases of graduate school. Thank you for listening to me, trusting me, and encouraging me to explore different directions. Jayson's ability to see interesting science everywhere and his being open to all kinds of ideas is very inspiring. His grasp on very different seemingly unrelated systems and his ability to relate them via analogies has been useful in many situations. He has also been a great teacher in the various aspects of a researcher's skillset such as writing, presenting, and even managing files.

I am grateful to John Toner for being a great committee chair making sure I was doing well academically and emotionally. Thank you also for forwarding the many post-doc positions during my job search, for infecting everyone around you with an enthusiasm to figure things out, and for teaching me to not be afraid to ask stupid questions.

I am fortunate to have had worked with my former advisor Steven van Enk. His insistence on consistently polishing one's intuition by exploring situations where it seems to fail and by always trying to anticipate the results of calculations has been very influential to me. I also thank him for sharing his many random insights such as the observer-dependence of entropy, or how, in physics, we often implicitly assume that an exact solution to an approximate equation is also an approximate solution to the exact equation.

I also acknowledge the funding by National Science Foundation under Grant No. CMMI-2128671 and Grant No. DMR–2145766 which supported part of the work.

I thank all my labmates through the years: Pragalv, Wenqian, Nathan, Maxx, Ben, Scott, Noah, Alexander, Alena, Garret, Cody, Jasper, and Elise. It was fun working together, sharing office and lunch at Uniquely Chengdu. I especially thank Wenqian for the many scientific and non-scientific conversations, and Maxx for being a stalwart soft matter club comrade.

I thank all the people past, present, and future involved in the various departmental and union committees working to make graduate school better. This dissertation too, is after all, a product of unionized labour. I especially thank the 2023-2024 GTFF bargaining team members. I had a lot of fun and learnt a lot working with you all. The moment of contract ratification was one of the biggest highs of my time at UO and I have never been part of a more productive and multi-talented group.

I thank many people for their love and support during my time in graduate school. I thank my family, especially my sister, for their continual support. I thank high school friends (especially Arpit, Anirudh, Ankita, Manish), undergrad friends (especially Deepesh, Pranjal, Sowmya), international caucus friends (especially Onder, Santiago), soccer friends (especially JB, Mus'ab, Saumya, Saurabh, Yewelsew), food friends (especially Ciro, Julianne, Philip, Srinivas), movie night friends, conference friends, online friends, miscellaneous friends, and the various friends of friends.

Special thanks, of course, goes to Marium and Kali.

“There are decades where nothing happens; and there are weeks where decades happen” — Vladimir Ilyich Lenin (supposedly) on doing a PhD in physics (supposedly)

TABLE OF CONTENTS

APPENDICES

LIST OF FIGURES

Figure Page

Figure Page

CHAPTER I

INTRODUCTION

This thesis consists of two separate projects both of which have the common theme of applying methods of non-Hermitian matrices to the physics of soft matter. Soft matter may be defined as materials, or ordered structures of interacting parts, that are easily deformed by thermal fluctuations and external stresses [5, 6, 7, 8]. Typically we are interested in the collective behavior in these ordered structures, i.e., behavior occuring at scales much larger than the scale of the composing parts (such as the atoms and molecules). Soft matter is also characterized by the fact that quantum aspects are unimportant in modelling it since the thermal fluctuations and structural deformations kill any kind of quantum coherence.

Examples of soft matter include liquids, colloids, polymers, foams, gels, sand, and shells. Soft matter which has been driven out of equilibrium is commonly referred to as soft *active* matter [9, 10, 11]. For example, we may subject the static systems above to external fields or consider collections of self-propelled components such as in models of flocks, cytoskeletons, and other living systems. Apart from studying nature another aspect of soft matter is the design of *metamaterials*, i.e., structures whose midscale geometry endow them with long-distance properties different from the stuff they are made up of [6, 12, 13]. Altogether the boundaries of what soft matter consists of are stretched every year in both experimental and theoretical directions. The interplay of complex geometries, defects, activity, non-reciprocal interactions, stochasticity, etc. leads to a rich phenomenology typically occuring at many different scales.

The richness of phenomenology demands a rich set of techniques to model the behavior and indeed there are many different ways to ‘do’ soft matter physics. The most common and traditional one is to use fields which are continuous functions formed by coarse-graining the original degrees of freedom and which vary at mesoscopic scales. The equations of motion governing the effective degrees of freedom described by the fields may then be derived using hydrodynamic or statistical physics methods.

1.1 CLASSICAL-TO-QUANTUM MAPPING TO STUDY SOFT MATTER

Linear operators, such as those representable by matrices, are ubiquitous in the equations of motion describing many exact models of nature including in the field of soft matter. They also occur as effective models when a more fundamental model is linearized around a point of interest. Common examples of linear models are convection–diffusion equations, linearized elasticity, and all of canonical quantum mechanics. It is sometimes useful to map such a linear model to the Schrödinger equation inheriting techniques such as spectral analysis, band structure, fermionic statistics, etc. which simplify the analysis substantially. For example, directed polymers and flux lines in type-II superconductors can be modelled by a Schrödinger equation evolving in imaginary time [14, 15, 16]. Non-crossing of the polymer chains can be mapped to a quantum mechanical system with fermionic statistics and external shear is mapped to an imaginary magnetic flux term. Similarly, the frequency spectrum of a network of mechanical oscillators can be mapped to the quantum mechanical electronic spectrum of non-interacting electrons in a crystal [17, 18].

Canonical quantum mechanics deals predominantly with Hermitian matrices (matrices which equal their conjugate-transpose) acting on vectors living in a Hilbert space. Since Hilbert spaces are equipped with a norm and are complete, they are topological vector spaces in which topological notions like the openness and closedness of subsets are well defined. Topological ideas in quantum mechanics has led to a plethora of novel phenomena such as topological insulators, the integer quantum Hall effect, quantized pumps, etc. In many cases the topological indices governing the phenomena, and hence the phenomena itself, are robust to the presence of noise and disorder. Advances in these topological ideas in quantum mechanics were also quickly applied to those soft matter systems which can be modelled using linear operators. Some examples include edge currents in stochastic reaction networks [19] and edge modes in spring-mass networks [17].

1.1.1 Floquet techniques for dynamic systems

For linear non-equilibrium systems, such as the parametric oscillators considered in this dissertation, the system is mapped to a time-dependent Schrödinger equation, i.e.,

$$i\frac{d}{dt}|\Psi(t)\rangle = \mathcal{H}(t)|\Psi(t)\rangle. \tag{1.1}$$

The solution to this equation is

$$|\Psi(t)\rangle = U(t)|\Psi(0)\rangle, \tag{1.2}$$

where $|\Psi(0)\rangle$ is the initial state of the system and the time-propagation matrix $U(t)$ satisfies

$$i\frac{d}{dt}U(t) = H(t)U(t) \tag{1.3}$$

with the initial condition $U(0) = \mathbb{I}$ the identity matrix.

If the Hamiltonian is time-periodic, $\mathcal{H}(t+T) = \mathcal{H}(t)$, the time-propagation matrix for such a system obeys $U(t+T) = U(t)U(T)$. The matrix $U(T)$ is called the Floquet matrix. The long-time behavior of the system is given by $U(t = nT) = U^n(T)$ and is thus captured fully by the Floquet matrix which we can parametrize as $U(T) =$

$e^{-i\mathcal{H}_{\text{eff}}T}$ [1]. The eigenvalues of the effective Hamiltonian $\mathcal{H}_{\text{eff}}$ lies in the non-simply connected space $S^1 \sim (-2\pi/T, +2\pi/T]$ (see Fig. 1.1). This brings another pathway to realize topological behavior in linear systems and has led to phenomena such as Floquet topological insulators [20].

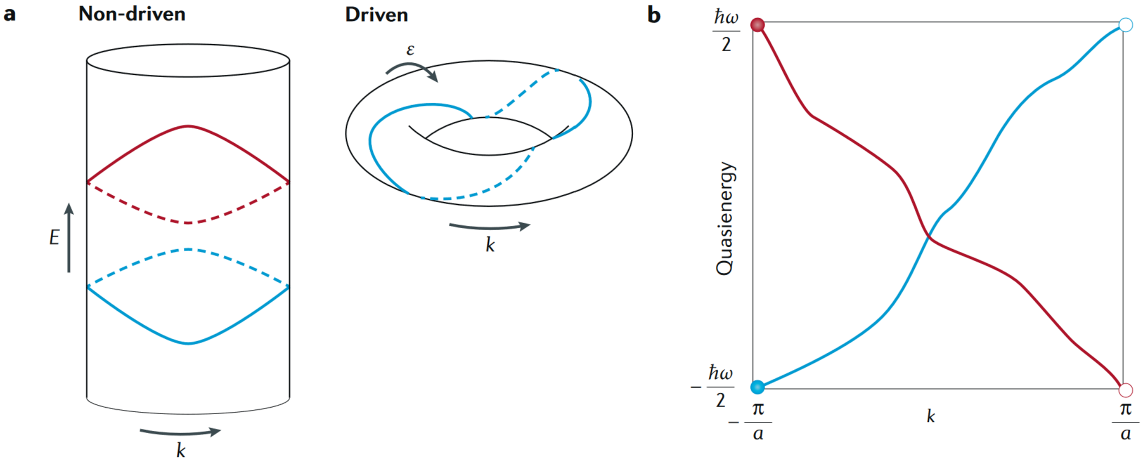

Figure 1.1. **a**, In a non-driven Hermitian system, the energy spectrum $E(k)$ is a real-valued function of the crystal momentum k. With periodic driving, the eigenvalues $\varepsilon(k)$ of the effective Hamiltonian are periodic and the Floquet bands may exhibit a winding as k traverses the Brillouin zone, $-\pi/a < k \leq \pi/a$. Here, a is the lattice constant of the system. **b**, A fully filled Floquet band with non-trivial winding can exhibit topologically protected quantized pumping in the adiabatic limit. Heuristically, the quantization of pumped charge follows from the fact that the average group velocity of a Floquet band, $\bar{v}_g$, is proportional to the quasienergy winding number W of the band, $\bar{v}_g = \frac{a}{2\pi\hbar}\oint \mathrm{d}k\frac{\mathrm{d}\varepsilon}{\mathrm{d}k} = a\frac{W}{T}$. Figure taken from Ref. [1].

1.2 An overview of non-Hermitian physics

The soft matter system under study may also be mapped to a quantum mechanical system with a non-Hermitian Hamiltonian. This is the subject of this thesis. Non-Hermitian operators are common when the underlying system has non-reciprocal couplings (such as in a system of sheared polymer chains) or external gain/loss (such as parametric oscillators). In fact, non-Hermitian Hamiltonians are being used as effective models for a variety of phenomena in photonics and condensed matter physics [2, 21] and come up naturally in the context of an open quantum system (a quantum-mechanical system which is not isolated but interacting with an external environment). These Hamiltonians are able to capture amplification, energy dissipation, probability fluxes, phase transitions and many other rich phenomena restricted by canonical QM postulates.

Let us review the major properties of non-Hermitian matrices which will play a major role in the succeeding chapters [21]. We denote a column vector by the ket $|v\rangle$ and the row vector which is its conjugate-transpose by the bra $\langle v| = |v\rangle^\dagger$.

1. *Properties of eigenvalues:* The eigenvalues of a non-Hermitian matrix may be complex-valued while those of a Hermitian matrix are always real-valued. The right and left eigenvectors of $\mathcal{H}$ are defined by $\mathcal{H}|R_i\rangle = \lambda_i|R_i\rangle$ and $\langle L_i|\mathcal{H} = \lambda_i\langle L_i|$. They share the same eigenvalues.

2. *Eigenvalue multiplicity:* If a Hermitian matrix, $\mathcal{H} = \mathcal{H}^\dagger$, has an eigenvalue λ_j repeated with multiplicity m_j then it also has a set of m_j corresponding independent eigenvectors. To be precise, let m_j^a be the number of times λ_j is repeated as a root in the characteristic polynomial, $\det(\mathcal{H}-\lambda\mathbb{I}_n) = 0$. Let m_j^g be the dimension of the null-space of the matrix, $\mathcal{H} - \lambda_j\mathbb{I}_n$. Then for a Hermitian matrix, the arithmetic and geometric multiplicities are equal, $m_j^g = m_j^a$. For a non-Hermitian matrix, $m_j^g \leq m_j^a$ in general.

3. *Exceptional and diabolical points:* Consider a parametrized non-Hermitian matrix $\mathcal{H}(\boldsymbol{k})$ with an eigenvalue degeneracy for the eigenvalue λ_j at $\mathcal{H}(\boldsymbol{k} = \boldsymbol{k}_0)$. If the arithmetic and geometric multiplicities are equal, $m_j^g = m_j^a$, then the point $\boldsymbol{k}_0$ in parameter space is called a *diabolical point.* If, on the other hand,

$m_j^g < m_j^a$, then the eigenvalue is called *defective*, and the point $\boldsymbol{k}_0$ is called an *exceptional point*.

The Riemann surface $\lambda(\boldsymbol{k})$ exhibits a branch point at the exceptional point (see Fig. 1.2). Upon encircling this exceptional point we reach a different Riemann sheet corresponding to a different eigenvalue. In a quasi-static regime this provides a topological mechanism to switch between eigenvectors [2]. There are ways to generalize this mechanism even in the absence of adiabaticity [22].

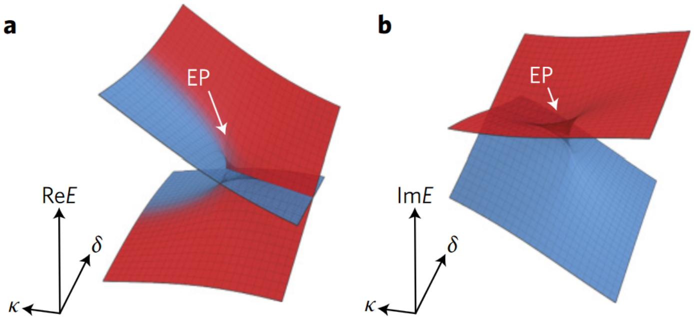

Figure 1.2. Riemann surfaces of the complex eigenvalues of the matrix $\mathcal{H} = \begin{pmatrix} \delta - ig & \kappa \\ \kappa & ig \end{pmatrix}$ versus the parameters (δ, κ). **a** shows the real part of the eigenvalues and **b** shows the imaginary part. This Hamiltonian models the physics of two sites with equal gain and loss set by the parameter g and coupled together with coupling κ. The energy difference between the sites is δ. The Hamiltonian exhibits an exceptional point when $\delta = 0$ and $\kappa = g$. Figure taken from Ref. [2].

4. *Diagonalizability:* A matrix $\mathcal{H}$ is diagonalizable if we can find an invertible matrix S and a diagonal matrix D such that $\mathcal{H} = SDS^{-1}$. If a non-Hermitian matrix has a defective degeneracy (is at an exceptional point), it is not diagonalizable and the most one can do is transform it into the unique Jordan normal form. That is a form in which all the entries in the lower triangle are zero.

5. *Eigenvectors:* For Hermitian matrices the right eigenstate and the left eigenstate are trivially related. For example, let $\mathcal{H}|\lambda\rangle = \lambda|\lambda\rangle$. Take the adjoint of both sides, $\langle\lambda|\mathcal{H}^\dagger = \lambda^*\langle\lambda|$ and use the properties of Hermitian matrices to show $\langle\lambda|\mathcal{H} = \lambda\langle\lambda|$. The right and the left eigenstates of $\mathcal{H}$ are then just adjoints of each other. Furthermore, the eigenvectors of a Hermitian matrix can always be chosen to be orthogonal to each other.

   For non-Hermitian matrices, the right eigenstate satisfies $\mathcal{H}|R_i\rangle = \lambda_i|R_i\rangle$ while the left eigenstate satisfies $\langle L_i|\mathcal{H} = \lambda\langle L_i|$ or equivalently $\mathcal{H}^\dagger|L_i\rangle = \lambda_i^*|L_i\rangle$. Orthogonality of eigenvectors is generalized to the concept of bi-orthogonality. That is, if the matrix is diagonalizable we can write it as $\mathcal{H} = \sum_j \lambda_j|R_j\rangle\langle L_j|$ with $\langle L_i|R_j\rangle = \delta_{ij}$.

1.2.1 Pseudo-Hermitian matrices

The systematic classification of the internal symmetries of Hermitian matrices to understand topological insulators led to a plethora of topological phenomena discovered in soft matter via versions of the quantum-classical mapping. Similarly, one may want to systematically classify the internal symmetries of non-Hermitian matrices and characterize the classes by their topological invariants. There are at least two main ways to do this.

One is to use K-theoretic methods analogous to those used in deriving the so-called 'tenfold way' for Hermitian matrices [23]. These methods, while conceptually difficult, provide a straightforward calculation of certain topological invariants. However, care must be taken to account for certain aspects of non-Hermitian matrices. For example, the notion of a bandgap in Hermitian matrices generalizes to either a point-gap or a line-gap depending on how one defines the separation between two bands of eigenvalues [24].

Another way is to use homotopy methods [25] which, while conceptually simpler, are much harder to compute partly because they capture more topological invariants compared to those accessible to K-theory. These additional topological invariants, which are not revealed by K-theory and which disappear on adding additional bands, are called fragile topological invariants [26]. In metamaterials and other soft matter contexts where a system with finite bands is an exact model and not an approximation, these fragile invariants might be physically relevant.

For the purposes of this dissertation, a 'coarser' classification of non-Hermitian matrices is enough. This is because (as we shall see later) the phenomena considered in this dissertation depends only on the real-to-complex transition of certain eigenvalues of the relevant matrix. Thus, we classify non-Hermitian matrices into three kinds: quasi-Hermitian if they only admit real eigenvalues, pseudo-Hermitian if they admit either real or complex-conjugate eigenvalues, and the rest which have no such constraints.

An alternate and more formal definition of pseudo-Hermitian matrices is the following. A matrix $\mathcal{H}$ is called pseudo-Hermitian if it satisfies $\mathcal{H} = G^{-1}\mathcal{H}^{\dagger}G$ for some invertible matrix G called the intertwining operator. G is not unique and can always be chosen to be Hermitian [27]. Similarly, $\mathcal{H}$ is called quasi-Hermitian if it satisfies $\mathcal{H} = G^{-1}\mathcal{H}^{\dagger}G$ for some invertible and positive-definite matrix G. These definitions are independent of the chosen basis and on an arbitrary similarity transform $\mathcal{H} \mapsto S\mathcal{H}S^{-1}$, we have $G \mapsto (S^{\dagger})^{-1}GS^{-1}$ as the new intertwining operator. Evidently, if G were Hermitian (and positive-definite), $(S^{\dagger})^{-1}GS^{-1}$ is also Hermitian (and positive-definite).

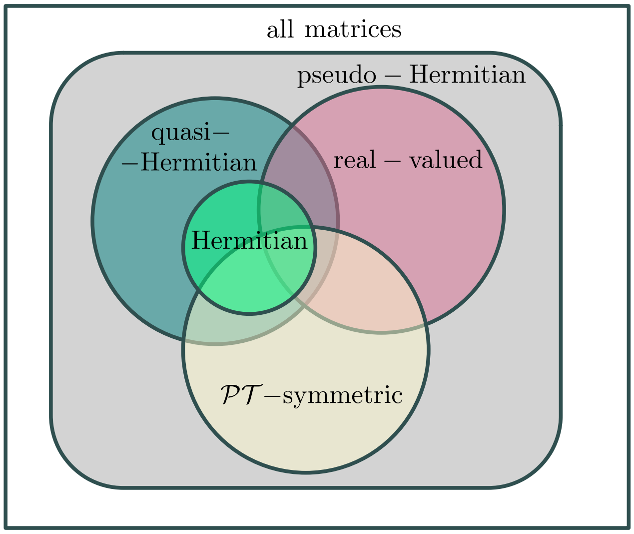

Figure 1.3. A family of matrices can be classified on the basis of whether they admit only real eigenvalues (quasi-Hermitian) or eigenvalues which are either real or come in complex conjugate pairs (pseudo-Hermitian). These definitions are basis-independent. For a given basis, we may also classify matrices according to whether they are Hermitian, $\mathcal{PT}$-symmetric, or real-valued. The former is a subclass of quasi-Hermitian matrices while the latter two are always pseudo-Hermitian.

Pseudo-Hermitian matrices are interesting, especially in the context of soft matter, because all real matrices are pseudo-Hermitian and every pseudo-Hermitian matrix can be basis-transformed to a real matrix (see **Chapter V**). The matrices occuring in soft matter are, of course, almost always real-valued. The real-to-complex eigenvalue transition in these matrices (called pseudo-Hermiticity breaking), by tuning some parameter, is typically accompanied by a drastic change in the behavior of the underlying system (such as the phase transition in the system of sheared polymer chains or the emergence of amplified modes in the parametric oscillator network). Typically, the parameter quantifies an external source of bias, amplification, or dissipation.

Since the eigenvalues of a pseudo-Hermitian matrix come in complex conjugate pairs, it is necessary for two real eigenvalues to meet and form a degeneracy for pseudo-Hermiticity breaking to occur. But can any degeneracy of two real eigenvalues λ_i and λ_j lead to pseudo-Hermiticity breaking? The answer is no. One computes the signature of the eigenvalue λ_j which is given by the sign of $\langle R_j | G | R_j \rangle$ where $|R_j\rangle$ is the corresponding right eigenvector. If λ_i and λ_j have the *same* signature, then they cannot collide and turn into complex conjugate eigenvalues [28, 29]. These conditions (elaborated in **Chapter V**) are useful to understand the conditions for parametric resonance to occur.

Now, quasi-Hermitian matrices can be similarity transformed to a Hermitian matrix. Write $G = R^\dagger R$ since it is positive-definite and use $S = R$ to transform basis such that $\mathcal{H} \mapsto R\mathcal{H}R^{-1}$ and $G \mapsto \mathbb{I}_n$. Thus, $R\mathcal{H}R^{-1}$ is Hermitian. As such, quasi-Hermitian matrices do not exhibit the exotic behavior of non-Hermitian matrices, such as complex-valued eigenvalues or defective degeneracies, and are thus arguably not very interesting.

With this background in non-Hermitian physics we are now ready to tackle some soft matter systems.

1.3 Diffusing directed paths as quantum mechanics in imaginary time

Many soft matter systems involve interacting lines that are stretched out along a preferred direction and undergo thermal fluctuations in the transverse direction. Examples include vortex lines in superconductors [15, 30], crystal step edges on vicinal surfaces [31], and polymers embedded in nematic liquid crystals [32]. The statistical mechanics of such systems falls under a class of models called directed polymer models. An early example of non-Hermitian physics in soft matter arose in a directed polymer model with a random potential [15]. In **Chapter II**, we investigate the non-Hermitian mechanics of directed polymers in periodic potential and uncover a new delocalization transition that can be understood using techniques from non-Hermitian quantum mechanics.

Consider a freely-jointed polymer chain (joint between sequential monomers is completely flexible) composed of many monomers, each of some fixed length b which is in the molecular scale. When set to float on the surface of a liquid this chain exhibits Brownian motion. At the scale of the individual monomers, the configuration of the chain at any instantaneous snapshot is highly jagged and irregular. However, the sheer size of these polymer chain macromolecules (each typically containing something like 10^3 to 10^5 atoms) simplifies the problem considerably. We can coarse-grain by averaging over the positions of a few neighboring monomers combining them into larger segments whose positions will be the new degrees of freedom [33]. This buries the microscopic degrees of freedom and makes the chain appear smoother such that any configuration can be parametrized using continuous differentiable functions as $\{x(\tau), y(\tau)\}$ where τ runs along the length of the chain.

Now, consider the polymer chain being pulled at its two ends via equal and opposite forces F directed along the $y-$axis. If the force is sufficiently strong, the probability of the chain to ever have overhangs or loops goes to zero. In this case we have a *directed* polymer chain which can be described succinctly by just $x(\tau)$ where $\tau \sim y$ now denotes the vertical coordinate. Furthermore, we place this chain on a substrate with potential energy per unit length given by $V(x)$. Because of Brownian motion, the motion of the chain is stochastic but we may define $\Psi(x, \tau)$ as the probability for the chain to pass through the point (x, τ). The equation of motion for this probability can be derived using a path integral approach (similar to quantum mechanics) and resembles the diffusion equation,

$$\frac{\partial \Psi(x,\tau)}{\partial \tau} = \left(\frac{1}{2\beta F}\frac{\partial^2}{\partial x^2} - \beta V(x)\right)\Psi(x,\tau). \tag{1.4}$$

The vertical direction τ acts as time and the diffusion constant is given in terms of the tension force as $\frac{1}{2\beta F}$.

Eq. (1.3) also describes magnetic flux lines passing through a type-II superconductor [15, 30]. When the term $V(x)$ is a disordered potential it accounts for the randomly positioned columnar defects in the superconductor and the vertically applied magnetic field acts as the tension force F on the flux line. In the absence of any shear force, the polymer chain configurations are vertically aligned on average. The disordered potential suppresses the diffusion of the chain (or the flux line) and makes it resistant to small amounts of applied shear (or a transverse component of the magnetic field). Extensive previous studies have considered the question of how much shear is required to make the polymer chain delocalize (i.e., for their averaged profiles to become non-vertical).

Shearing the chain is equivalent to subjecting its ends to equal and opposite transverse forces of strength $F\theta$ (see Fig. 2.1) which adds a bias term to its diffusion equation breaking the $x \mapsto -x$ symmetry,

$$\frac{\partial \Psi(x,\tau)}{\partial \tau} = \left(\frac{1}{2\beta F}\frac{\partial^2}{\partial x^2} - \theta\frac{\partial}{\partial x} - \beta V(x)\right)\Psi(x,\tau). \tag{1.5}$$

If we redefine variables by mapping $\tau \to it$, $\beta \to \frac{1}{\hbar}$, $F \to m$, and $F\theta \to g$, the equation can be written (upto an irrelevant constant term in the quantum Hamiltonian) as the time-dependent Schrödinger equation [15],

$$i\hbar\frac{\partial \Psi(x,t)}{\partial t} = \left(\frac{(p+ig)^2}{2m} + V(x)\right)\Psi(x,t). \tag{1.6}$$

We see that the Hamiltonian $\mathcal{H}(g)$ is non-Hermitian when g, which is proportional to the shear and which captures the amount of non-reciprocity in the system, is non-zero. In fact, this is one of the earliest examples of a non-Hermitian Hamiltonian used to model a soft matter system. For a symmetric potential $V(x) = V(-x)$, $\mathcal{H}(g)$

is in fact pseudo-Hermitian with the parity operator $\mathcal{P}$ which maps x to $-x$ being the intertwining operator.

Similar to quantum mechanics, we can find the eigenvectors $\Psi_n(x)$ of $\mathcal{H}(g)$ which satisfy $\mathcal{H}(g)\Psi_n(x) = \varepsilon_n \Psi_n(x)$. The solution to Eq. (1.3) is then $\Psi(x,\tau) = \sum_n c_n e^{-\varepsilon_n \tau}\Psi_n(x)$ where the coefficients c_n are determined by the boundary conditions (initial conditions in quantum mechanics). In the bulk of the system where τ is large, the eigenvector corresponding to eigenvalue with smallest real part is dominant and $\Psi(x,\tau) \sim c_0 e^{-\varepsilon_0 \tau}\Psi_0(x)$. The properties of the polymer system are then determined by the ground state of the Hamiltonian.

For a disordered system (the Hatano-Nelson model), the eigenvalues of the Hermitian matrix $\mathcal{H}(g = 0)$ are randomly distributed on the real axis of the complex plane. The current for such a disordered system is zero due to Anderson localization [34] (corresponding to the polymer chain being localized). In fact, Anderson was able to show that diffusion will be suppressed in a one-dimensional (Hermitian) quantum mechanical disordered system. However, when shear is applied, the non-Hermitian term proportional to g makes the eigenvalues gradually move off the real axis and gain an imaginary part. Eigenvectors corresponding to these eigenvalues delocalize. Eventually, at very large values of shear (or g), all the eigenvalues leave the real axis and trace out ovals in the complex plane.

Delocalization due to non-Hermiticity in a disordered system is well understood. In **Chapter II** we will consider a periodic potential $V(x+a) = V(x)$ with no disorder (see Fig. 2.1). For $g = 0$, the Hamiltonian is a simple model of an electron in a 1D crystal and the eigenvalues form bands on the real axis. When the shear is increased, the bands 'inflate' and form ovals in the complex plane. At a critical value of shear

$:= F\theta_c$, the ground-state band meets the band just above it removing the bandgap (see Fig. 2.3). Can this gap closure lead to a different mechanism for delocalization?

Using molecular dynamics simulations (by my collaborator Alexander Patapoff) and theoretical analysis we find that a single polymer chain in the system delocalizes at arbitrarily small shear. Its average tilt angle ϕ, measured by the slope of its average configuration in simulations and calculated as $\partial_\tau \langle x \rangle$ in theory, exactly equals the angle of tension θ. In the quantum system the tilt angle corresponds to the current in the system. These results make sense since a 1D crystal with a single electron (or indeed with any filling of electrons incommensurate with the number of potential energy grooves) is a conductor.

To make the system more interesting we add additional localizing terms. We do this by considering n polymer chains with non-crossing interactions between them. The system of non-crossing directed polymer chains maps to a quantum system of fermions [14] which allows us to access the physics of the bandgap. If we choose n to be commensurate with the number of potential energy grooves, we will have a 1D crystal with a filled band separated from the higher eigenvalues by a bandgap. Indeed the molecular dynamics simulations reveal that the system at commensurate filling remains localized for $\theta < \theta_c$ and delocalizes beyond this critical value of shear. Thus this transition is equivalent to an insulator-conductor transition by the closing of a bandgap.

The form of the Hamilonian in (1.6) shows that shear acts as an imaginary vector potential term corresponding to an imaginary magnetic flux line threading through the system with periodic boundary conditions. This suggests the use of a gauge transform which removes the vector potential term at the cost of changing the boundary condition of the eigenstates and making their (crystal) momentum

k complex-valued. With the problem mapped in this way, we are interested in the properties of the complex-valued function $\varepsilon_n(k)$ with k being a complex-valued number, i.e., the analytical continuation into the complex plane of the real-valued eigenvalue problem in regular Hermitian quantum mechanics. This problem was considered by Kohn and others [3, 35] leading to the many results which are universal irrespective of the form of the periodic potential (see **Chapter II**).

From a statistical physics perspective, we can understand the phenomena as following. For a system with incommensurate filling, one can have a chain lying partly in one groove and partly in the one next to it. This forms a kink in the chain configuration which has a small energetic cost (proportional to the amplitude of the potential energy) but provides a lot of entropy since the kink can move freely without any additional energy costs along the length of the chain. In this way the chain can also move from one free groove to another. However, for commensurate filling, the cost of the formation of a kink is drastically increased since part of the chain now has to share a groove with another chain decreasing the entropic fluctuations due to the non-crossing constraints. In the limit of infinitely long chains, the probability of a kink formation goes to zero and the system becomes rigid and loses ergodicity—a chain never leaves its initial groove.

1.4 NON-RECIPROCAL BEHAVIOR IN PARAMETRIC OSCILLATOR NETWORKS

Our next soft matter system is in the regime of classical mechanics where Newton's third law constrains interactions to be reciprocal, i.e., the force applied by particle A on particle B is equal and opposite to that applied by particle B on particle A. Previously, the frequency eigenvalue problem of static mechanical networks was mapped to the energy eigenvalue problem of non-interacting electrons in a crystal lattice leading to topologically protected edge states [17, 18]. However, these systems were always in the regime of equilibrium physics. One can make systems 'active' by subjecting them to external fields or fluxes of energy. Active metamaterials [36, 37] exhibit novel phenomena such as amplification of desired modes and one-way propagation of signals and waves. Typically this is accompanied or enabled by the breaking of reciprocity in these systems through directional modulation [38]. Here, we consider parametrically driven oscillators and recover the conditions for parametric resonance using the psuedo-Hermitian symmetry of the relevant linear operator. We also characterize the properties of systems modulated with a wave-like modulation using the space-time symmetry of such systems.

Specifically, in **Chapter III** we consider n coupled classical mechanical oscillators of equal masses with a stiffness matrix $K(t)$ that is time-periodic with period T. The matrix is additionally real-valued, symmetric, and positive-definite at all times. The time-dependence in this non-equilibrium system can allow it to gain or lose energy which will be the source of non-Hermiticity. The equations of motion of the oscillators are given by

$$i\frac{d}{dt}\begin{pmatrix}\boldsymbol{x}(t)\\ \boldsymbol{p}(t)\end{pmatrix} = \underbrace{-i\begin{pmatrix}0 & -\mathbb{I}_n\\ K(t) & 0\end{pmatrix}}_{\mathcal{H}(t)}\begin{pmatrix}\boldsymbol{x}(t)\\ \boldsymbol{p}(t)\end{pmatrix} \tag{1.7}$$

where $\boldsymbol{x}(t)$ and $\boldsymbol{p}(t)$ label the vector of positions and momenta, respectively, of the oscillators. The properties of the stiffness matrix render the quantum Hamiltonian $\mathcal{H}(t)$ quasi-Hermitian.

Before considering the non-equilibrium system let us first discuss the static case where $K(t) = K$. We can use $R = \begin{pmatrix} \sqrt{K} & 0 \\ 0 & i\mathbb{I}_n \end{pmatrix}$ to transform the equation to

$$iR\frac{d}{dt}\begin{pmatrix} \boldsymbol{x}(t) \\ \boldsymbol{p}(t) \end{pmatrix} = -iR\begin{pmatrix} 0 & -\mathbb{I}_n \\ K & 0 \end{pmatrix} R^{-1}R\begin{pmatrix} \boldsymbol{x}(t) \\ \boldsymbol{p}(t) \end{pmatrix} \tag{1.8}$$

$$i\frac{d}{dt}R\begin{pmatrix} \boldsymbol{x}(t) \\ \boldsymbol{p}(t) \end{pmatrix} = \begin{pmatrix} 0 & \sqrt{K} \\ \sqrt{K} & 0 \end{pmatrix} R\begin{pmatrix} \boldsymbol{x}(t) \\ \boldsymbol{p}(t) \end{pmatrix} \tag{1.9}$$

with a Hermitian Hamiltonian [18]. We used the commutation of R and $\frac{d}{dt}$ which would fail if the stiffness matrix were time-dependent.

Now that the mapping to Hermitian quantum mechanics is complete a number of techniques transfer over, most notably topological techniques that predict edge modes for Hamiltonians with the right internal symmetries [18]. We note that the transformation R is not unique and any decomposition of the form $K = QQ^T$ (rather than $K = \sqrt{K}.\sqrt{K}$) can provide the required transformation [18]. In isostatic lattices, a natural choice is to choose Q to correspond to the equilibrium matrix which relates spring tensions to displacements of the attached masses. Q and Q^T have more information than that provided by K and for instance allow for a characterization of self-stress states in the system [17]. A summary of these topological ideas as applied to static mechanical networks can be found in Ref. [12].

In our case, since the Hamiltonian is time-dependent a transformation to a Hermitian one is not possible. Since the dynamics for our non-equilibrium time-modulated system will be governed by a non-Hermitian linear operator, we will see interesting phenomena such as the amplification of modes. In fact, we will be able to amplify waves that only travel in one direction leading to the emergence of non-

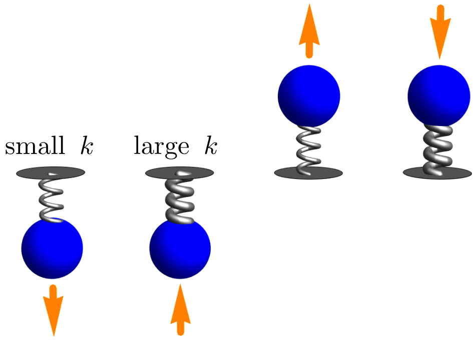

Figure 1.4. An oscillator of natural frequency ω with its spring stiffness being periodically modulated, $k(t) = k[1+\delta \cos \Omega t]$. If $\Omega = 2\omega$, as shown, the spring is stiffer whenever the mass moves towards its mean postion. For such a choice of parameters, energy is pumped into the oscillator and its amplitude grows exponentially with time.

reciprocal behavior. The phenomenon underlying the amplification of modes is that of parametric resonance.

Consider a single oscillator with natural frequency $\omega = \sqrt{\frac{k}{m}}$ and modulate its spring stiffness in a time-periodic manner: $k(t) = k[1 + \delta \cos \Omega t]$. If we choose the modulation frequency to be $\Omega = \frac{2\omega}{r}$ where r is any positive integer, we can choose initial conditions such that the oscillator's motion towards the mean position is in sync with the spring stiffness becoming stiffer (see Fig. 1.4). For such choice of parameters and initial conditions, the oscillator's amplitude will start to increase exponentially. This occurs because each time the oscillator is returning to its mean position the spring is stiffer pulling it harder and granting it more kinetic energy. On the other hand, each time the oscillator moves away from its mean position the spring is looser allowing it to gain more potential energy. In this manner, energy is pumped into the oscillator. These conditions for parametric resonance of a single oscillator can be explicitly calculated using different variations of perturbation theory [28, 39].

Next, let us consider the parametric resonance conditions for an arbitrary mechanical network. We integrate (1.4) to find the Floquet matrix $U(t = T)$ with initial conditions set to $U(t=0)=\mathbb{I}_n$. Writing $U(T)=e^{-i\mathcal{H}_{\text{eff}}T}$ we focus on the properties of the effective Hamiltonian $\mathcal{H}_{\text{eff}}$. The conditions for parametric resonance are then the conditions for the eigenvalues of $\mathcal{H}_{\text{eff}}$ to become complex-valued since that grants the oscillation frequency a non-zero imaginary part. We can find the latter by characterizing the internal symmetries of the effective Hamiltonian.

First, since the Floquet matrix $U(T)$ is purely real (the equations of motion in classical mechanics are real-valued), $\mathcal{H}_{\text{eff}}$ is purely imaginary. Second, $\mathcal{H}_{\text{eff}}$ is pseudo-Hermitian, $G\mathcal{H}_{\text{eff}}G^{-1}=\mathcal{H}_{\text{eff}}^{\dagger}$, where $G=iJ=i\begin{pmatrix}0 & \mathbb{I}_n\\ -\mathbb{I}_n & 0\end{pmatrix}$. This pseudo-Hermiticity arises from the symplectic structure of Hamilton's equations of motion (J is the symplectic form). Pseudo-Hermiticity implies that the eigenvalues of $\mathcal{H}_{\text{eff}}$ become complex-valued when two real eigenvalues of opposite signature, given by $\langle v|G|v\rangle$, collide. Tracking the formation of these unstable degeneracies is tractable at the small modulation limit. It leads to the result that parametric resonance occurs when $\Omega=\frac{\omega_i+\omega_j}{r}$ where ω_i and ω_j are any two natural frequencies of the unmodulated coupled system. The form of the amplified modes depends on the normal mode eigenvectors corresponding to the frequencies ω_i and ω_j.

From the perspective of designing interesting amplified modes in the system we can consider mechanical networks with an external symmetry. Specifically, consider a ring of n masses connected to each other with springs of stiffness g and constrained to move in the vertical direction. The masses are also connected to fixed positions on the ground with springs of stiffness k. Let us modulate the system such that the spring corresponding to the jth oscillator is given by $k_j(t)=k[1+\cos(\Omega t+j\frac{2\pi}{n})]$. This sets up a stiffness wave in the system breaking chiral symmetry. Numerical solutions show that by tuning the driving frequency Ω one can amplify travelling waves in one direction (say clockwise) while leaving the wave's chiral copy unamplified. We are able to do this regardless of the functional form of the parametric modulation suggesting that the additional external symmetry in the system is protecting certain modes from amplifying. Since the two modes are degenerate, in the absence of modulation, the results of the preceding discussion are not sufficient to provide an analytical understanding of this phenomena. To understand this analytically we need to develop a framework which improves the theoretical discussion above by capturing effects of this symmetry.

1.5 SPACE-TIME SYMMETRY

The symmetry of the modulated system comes from it being invariant after a translation by one oscillator in the direction of the stiffness wave followed by a time evolution of $\frac{T}{n}$ time units. Explicitly, for a ring of n oscillators, the Hamiltonian satisfies

$$\mathcal{H}(t) = S\mathcal{H}(t+T/n)S^{-1}, \tag{1.10}$$

where S is the matrix operator which cyclically shifts each oscillator's coordinates by one position in the direction of the stiffness wave. This equation implies that the time-propagation matrix satisfies

$$U(t+T/n) = S^{-1}U(t)SU(T/n), \tag{1.11}$$

which can be considered a generalization of Floquet's theorem (Floquet's theorem is recovered when $S = \mathbb{I}_{2n}$). In particular, we can factorize the Floquet matrix (using the fact that $S^n = \mathbb{I}_{2n}$)

$$U(T) = S^{-n}[SU(T/n)]^n = [SU(T/n)]^n. \tag{1.12}$$

We call the matrix $X_n := SU(T/n)$ the *space-time Floquet matrix.* The effective Hamiltonian defined by $SU(T/n) = e^{-i\mathcal{H}'_{\text{eff}}T}$ enjoys the same internal symmetries as the one defined using the Floquet matrix via $U(T) = e^{-i\mathcal{H}_{\text{eff}}T}$. However, since the map $M \mapsto M^3$ from the set of square matrices with complex numbers to itself is non-invertible, the space-time Floquet matrix X_n and the effective Hamiltonian $\mathcal{H}'_{\text{eff}}$ defined in terms of it provide more information about the system dynamics than the Floquet matrix $U(T)$ does.

By repeating our previous strategy of tracking the formation of unstable degeneracies where pseudo-Hermiticity breaking occurs at the limit of small modulation on $\mathcal{H}'_{\text{eff}}$ we find the conditions for parametric resonance for a space-time symmetric system (see **Chapter III**). The conditions for this selective one-way amplification are obtained exactly from the symmetries alone, independently of the functional form of the time-modulation. These conditions provide a simple way to engineer nonreciprocal transport and one-way amplification in non-Hermitian Floquet systems.

The above formulation of the space-time Floquet matrix is applicable widely to any linear system enjoying space-time symmetry [40, 41] beyond the mechanical systems we consider in detail. To demonstrate this generality consider a quantum mechanical system with a time-periodic Hamiltonian given by

$$\mathcal{H}(t) = \frac{p^2}{2\mu} + V_1 \cos\left(\frac{2\pi x}{b}\right) + V_2 \cos\left(\frac{2\pi p x}{mb} - \frac{2\pi t}{T}\right) \tag{1.13}$$

where m and p are positive integers. Since the system has discrete translational symmetry the Hamiltonian $\mathcal{H}(t)$ commutes with $S(mb)$ the operator which translates by length mb and can be block-diagonalized in the basis of Bloch states, $\mathcal{H}(t) = \oplus_{k \in (-\frac{\pi}{mb}, +\frac{\pi}{mb}]} \mathcal{H}(k, t)$.

The conventional way to analyze such a system would be to integrate the time-dependent Schrödinger equation for each block matrix $\mathcal{H}(k,t)$ up to the period T and determine the effective Hamiltonian from the Floquet matrix $U(k,t) = e^{-i\mathcal{H}_{\text{eff}}(k)T}$.

However, the system has the additional space-time symmetry which can simplify the analysis to one which involves integration of the system dynamics for less time and gets rid of extraneous folding and degeneracies in the band structure. First, we note that there exists an integer r_τ such that the Hamiltonian is invariant under $(x,t) \mapsto \left(x + r_\tau b, t + \frac{T}{m}\right)$ (see **Chapter IV**). The Floquet matrix can be factorized as

$$U(k,T) = X^m \left(k, \frac{T}{m}\right), \tag{1.14}$$

$$X\left(k, \frac{T}{m}\right) = e^{-ir_\tau kb} S(k, r_\tau b) U\left(k, \frac{T}{m}\right). \tag{1.15}$$

We call $X\left(k, \frac{T}{m}\right)$ the space-time Floquet matrix. Compared to a system with ring geometry, the space-time Floquet matrix has an additional factor of $e^{-ir_\tau kb}$ for a lattice geometry.

Again we define the effective Hamiltonian $\mathcal{H}'_{\text{eff}}(k)$ of the system by $e^{-i\mathcal{H}'_{\text{eff}}(k)\tau_0} := X(k,\tau_0)$ and denote its jth eigenvalue by $\omega_j(k)$. In this way we need to integrate the system dynamics only for time $\frac{T}{n}$ (rather than T for generic Floquet systems) which gets rid of extraneous folding and degeneracies in the band structure. The consequences of this general space-time formulation for lattice systems will be discussed in detail in **Chapter IV** where we apply it to gain insights on Thouless pumps beyond the adiabatic regime and on parametrically driven oscillator lattices where we design principles for broadband amplification.

CHAPTER II

DELOCALIZATION OF INTERACTING DIRECTED POLYMERS ON A PERIODIC SUBSTRATE: LOCALIZATION LENGTH AND CRITICAL EXPONENTS FROM NON-HERMITIAN SPECTRA

This work was done in collaboration with Alexander Patapoff and Jayson Paulose and published in Physical Review E as Ref. [42]. Alexander developed and implemented the numerical simulations and analyzed simulation data. Jayson designed and supervised the research, analyzed simulation data, and edited the manuscript. I performed the theoretical analysis and drafted the manuscript. Details on the numerical simulations, which I did not contribute to, are included in the chapter and its appendices to make the discussion complete.

2.1 Introduction

Non-Hermitian operators [21, 43] have been extensively used to describe the dynamics of a variety of quantum [2, 44, 45] as well as classical systems [46, 47, 48, 49]. They are ubiquitous in both exact and effective models of nature capturing gain/loss in open systems [2], dissipation [50], probability fluxes [19, 51], sensitivity to boundary conditions [52, 53, 54], and various other phenomena excluded by assumptions of Hermiticity. They also enable the description of new kinds of phase transitions and topological classifications beyond the existing Hermitian framework for condensed matter [24, 55, 56]. For example, when non-Hermitian systems are periodic in space, their excitations are described by complex-valued band structures [57] which support uniquely non-Hermitian properties such as exceptional points (branch points) [58]. The physical implications of non-Hermitian band effects have been explored in a wide range of classical systems [59, 60, 61, 62, 63].

In systems of many bodies—such as spin waves, electrons, polymer chains, and vortex lines—generic thermodynamic phases may be distinguished by the localization properties of probability densities throughout the bulk [64]. Here, non-Hermitian terms quantify the capacity of external forces and fields to generate fluxes of probability and information which can drive the system out of a localized phase [15, 51, 65, 66, 67]. Non-Hermitian delocalization has been extensively studied in models of thermally fluctuating lines under simultaneous tension and shear forces in the presence of randomly positioned columnar pinning sites [15, 65], which serve as effective models for magnetic vortex lines penetrating through type-II superconductors with columnar defects [30, 68, 69]. The statistical mechanics of fluctuating lines in d dimensions was mapped to the quantum-mechanical time evolution of bosons in $d-1$ dimensions, whose Hamiltonian becomes non-Hermitian when the lines are sheared in a direction transverse to the defect axes. The single-particle energy eigenstates, which are localized due to disorder, become delocalized when the strength of non-Hermitian terms exceed a threshold corresponding to a critical shear force [15]. The delocalization of the bosonic eigenstates manifests as a tilt in the average conformations of the lines relative to the columnar defects. This non-Hermitian delocalization transition survives in the presence of interactions [70, 71, 72, 73, 74, 75].

However, the simultaneous interplay of non-Hermitian drive, thermal fluctuations, interactions, and confinement due to spatial *periodicity*, as opposed to *disorder*, remains poorly understood. Prior works on non-Hermitian delocalization of magnetic vortices in periodic lattices of pinning sites operated in the tight-binding limit [76, 77, 78], thereby failing to capture dependencies on the form of the continuous potential [79]. Field-theoretic studies, which in turn derived their effective action from the tight-binding limit via a Hubbard-Stratonovich transformation, uncovered

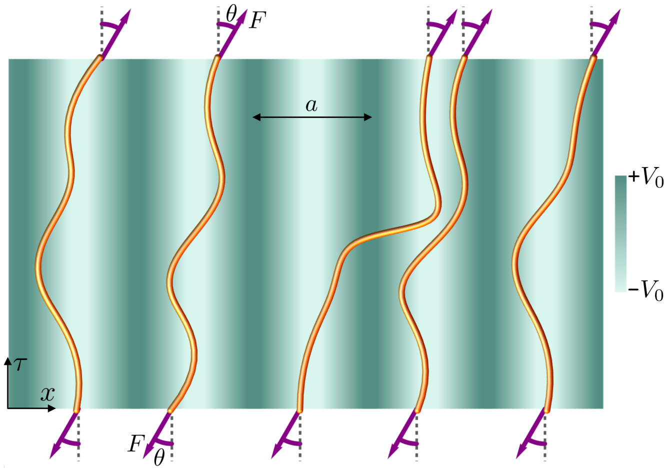

Figure 2.1. Schematic and description of our model system. Thermally fluctuating polymer chains (orange lines) with noncrossing constraints are subjected to a tension force F (purple arrows) on a two-dimensional substrate potential of strength $V(x)$ per unit length (green background). The potential, of amplitude V_0, is periodic (with period a) along the x direction and constant along the τ direction. The tension force, F, is applied to the ends of each chain at a specified force angle, θ, with respect to the τ-axis; the transverse component $F\theta$ of the tension is called the shear force. F is assumed to be large enough such that the chains do not double back on themselves and self-interactions of a chain with itself are avoided.

new thermodynamic phases in the Hermitian setting [80] whose non-Hermitian counterparts have been investigated using a mean-field model in 2+1-dimensions (the upper critical dimension) [81] but not in 1+1D. The form of the continuum equilibrium density profiles and their connection with spectral and topological features of non-Hermitian band structures was not elucidated in these prior studies.

In this work, we investigate non-Hermitian delocalization in a continuum statistical mechanical model with interactions, in which localization derives from a band-insulating state due to an underlying periodic potential. Specifically, we use classical molecular dynamics simulations and analytical calculations to study the effect of shear forces on a model of directed polymers confined to two dimensions and experiencing a smoothly varying periodic substrate potential (see Fig. 2.1 for a schematic and a description of our model). Directed polymers are thermally fluctuating chains that are extended along a preferred direction by an external field, which prevents self-interactions within chains. Besides describing superconductor vortices [30, 82], directed polymer models capture the statistical mechanics of semiflexible polymers embedded in liquid crystals [83] and wandering steps on vicinal surfaces of crystals [31]. All these systems share the property that the extended constituents cannot cross each other in space. Directed polymers with noncrossing interactions can be exactly solved [14, 16]; in our model, noncrossing interactions combine with the periodic potential to generate a state in which individual polymers are localized to distinct grooves [84]. Upon increasing the shear strength, the polymers collectively undergo a delocalization transition at a threshold force angle beyond which their average equilibrium conformations are tilted and no longer align with the substrate.

We map our model system of polymer chains to a one-dimensional (1D) quantum Hamiltonian with non-Hermitian drive caused by an imaginary vector-potential term. We find the average tilt of the many-body system, at arbitrary shear values and filling density of polymer chains, in terms of the complex non-Hermitian band structure [Eq. (2.27)] and show that the commensurate system undergoes a sharp transition in the thermodynamic limit. The delocalization transition corresponds to a gap closure in the complex non-Hermitian band structure associated with the substrate potential in the presence of shear forces. The exact value of the critical force angle at which the polymers delocalize is found in terms of the position of the branch point (exceptional point) in the spectrum [Eq. (2.20)] while the critical exponent by which the shear modulus diverges is determined by the order of the branch point and is universal for all periodic potentials [Eq. (2.29)]. The theoretical prediction of the critical force angle quantitatively agrees with the transition observed in our simulations.

Our theoretical predictions rely upon a gauge transformation which maps the non-Hermitian quantum system to a Hermitian system, albeit with altered boundary conditions that necessitate the use of complex-valued crystal momenta to describe the Bloch eigenfunctions of the periodic potential. Using this mapping, we show that the the complex-valued non-Hermitian band structure is the analytical continuation of the real-valued Hermitian band structure for complex momenta, which is well-studied in the context of surface states of finite crystals [3, 35] and which we make extensive use of. We also report preliminary evidence of a reentrant delocalization transition in the presence of both periodic potential and disorder, and explore possible connections with non-Hermitian topological pumps.

This article is structured as follows: In Sec. 2.2, we report properties of the equilibrium chain conformations observed in molecular dynamics simulations and numerically demonstrate a localization-delocalization transition. In Sec. 2.3.1, we derive the diffusion equation governing the probability density of the chains and map it to the Schrödinger equation with a non-Hermitian Hamiltonian. We find the eigenstates of the Hamiltonian in Sec. 2.3.2 and in Sec. 2.3.4 show that the delocalization threshold is captured by a branch point in the complex-valued band structure. We also verify the theoretical prediction with the results from simulations. We report a critical exponent associated with the delocalization transition in Sec. 2.3.5, preliminary results on a system with quenched substrate disorder in Sec. 2.4, and finally the relation to topologically quantized currents in Thouless pumps in Sec. 2.5. We discuss the implications of our results and potential future directions in Sec. 2.6.

2.2 Simulation results

We first report the results of Langevin dynamics simulations of a discretized version of the system depicted in Fig. 2.1, in which changes in equilibrium conformations at different filling fractions and force angles are readily visualized. We simulated thermally fluctuating chains of monomers confined to two dimensions using the open-source molecular dynamics software `HOOMD-Blue` [85] (see Appendix A.1 for implementation details). The chains are stretched out via a tension force applied to both ends, and experience a grooved substrate potential. Monomers repel each other with a short-ranged potential, and are linked to neighbors along the chain using stiff harmonic springs, to emulate polymers that cannot cross each other and are free to experience shape fluctuations. The substrate potential per unit length, $V(x)$, is periodic along the x direction and constant along the τ direction (shaded background in Fig. 2.1). The tension force, F, is applied to the ends of each chain at a specified force angle, θ, with respect to the grooves of the potential (the τ axis). The force angle is kept constant during each simulation run and quantifies the degree of shear experienced by the polymers. The effect of a finite temperature is incorporated by including viscous drag and introducing random forces on monomers whose strength is related to the desired temperature via a fluctuation-dissipation relation. After an equilibration period, monomer positions can be aggregated over statistically independent time points to obtain equilibrium density profiles of the fluctuating chains.

When the potential energy experienced by a single monomer is comparable to the thermal energy scale k_BT, a single polymer chain wanders across the simulation box with no preferred position [Fig. 2.2**a**]. Upon subtracting the center-of-mass motion of the chain from the monomer positions at each time step, the equilibrium density profile obtained by aggregating monomer positions over thousands of independent time steps (see Appendix A.1 for details) displays an overall tilt in the direction of the transverse shear force, as seen in Fig. 2.2**d**. The tilt angle ϕ, extracted from the difference in the average x positions from the density profiles near opposite ends of the chain, is seen to align with the force angle θ (Fig. 2.2**g**). This alignment shows that a single chain is free to tilt in response to the external tension and is not significantly confined by the substrate potential.

The polymer conformations are markedly different when the system is prepared at a commensurate filling of one polymer per groove of the periodic potential. At small force angles, the wandering of polymers in the multichain system is suppressed and each chain is localized to a distinct groove [Fig. 2.2**b**] [84] breaking ergodicity [86, 87]. The aggregated density profile shows that the chains remain vertically aligned even at nonzero shear, except for a small amount of bending near the ends [Fig. 2.2**e**]. Only at force angles larger than a threshold value, $:= \theta_\mathrm{c}$, do the chain conformations acquire a significant tilt along the entire length of the chain [Fig. 2.2**f**]. The threshold force angle is identified by a sharp increase both in the magnitude of the tilt ϕ and in the slope of the ϕ-θ relationship (numerical estimation of θ_c is discussed in Appendix A.2). At force angles much larger than the threshold, the chains align with the applied force [$\phi \approx \theta$, Fig. 2.2**g**]. At $\theta > \theta_\mathrm{c}$, not only do the chains display an abrupt tilt, they also drift back and forth across the substrate at equilibrium with no preferred center-of-mass location. This motion occurs via the diffusion of kinks that carry a chain over a potential peak to the adjacent valley [Fig. 2.2**c**]; the kink positions and motion must be coordinated across all chains to satisfy the noncrossing constraint [81].

In summary, the commensurate system exhibits two distinct equilibrium phases in simulations: a localized phase with untilted chain conformations confined to

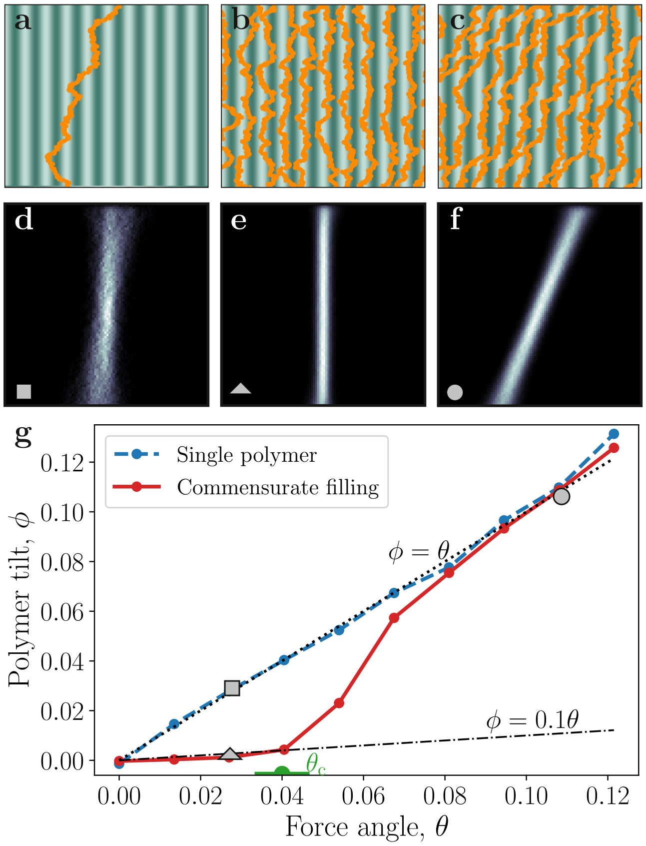

Figure 2.2. **a–c**, Snapshots of Langevin dynamics simulations of discretized polymer chains (points) on a periodic substrate potential (colormap same as in Fig. 2.1). Each chain has equilibrium length $40a$ and the simulation box has width $10a$; x and τ directions have different scales. **a**, Single polymer under low shear. **b, c**, Noncrossing polymers under commensurate filling (one chain per repeating unit of the substrate potential) under low (**b**) and high (**c**) shear. **d–f**, Aggregated density profiles of equilibrium chain conformations from simulations **a–c**. **g**, Tilt angle of the aggregated polymer conformations, ϕ, as a function of force angle, θ, as measured in simulations of a single polymer and of multiple polymers under commensurate filling. Gray symbols indicate the parameter values for panels **a–f**. Dotted line shows $\phi = \theta$. Critical force angle θ_c is estimated as the intersection of measured tilt–angle curve with $\phi = 0.1\theta$ (dash-dotted line; see Appendix A.2 for details). The spacing of simulated θ values provides the uncertainty in the estimate. From the commensurate curve, we obtain $\theta_c = 0.040 \pm 0.007$ (green symbol on θ axis).

individual potential grooves, and a delocalized phase in which chains are tilted in the direction of the applied force and wander across the substrate. To explain these phases, we map the density profiles of the classical equilibrium system to the quantum probability evolution of noninteracting fermions experiencing a periodic potential [84] in the presence of a non-Hermitian term due to shear [15]. The mapping has its roots in field-theoretic descriptions of the statistics of polymer melts [33, 88, 89, 90], but is simplified by the absence of self-interactions of each chain with itself—the tension is assumed to be large enough that each chain conformation is described by a single-valued function $x(\tau)$ and chains do not double back on themselves along the τ direction. This feature, which distinguishes *directed* polymer models from regular polymers, allows the corresponding quantum system to be exactly solved for some types of inter-polymer interactions [14, 16].

2.3 THEORETICAL ANALYSIS

2.3.1 Classical-quantum mapping

The chains of monomers depicted in Fig. 2.2**a**–**c** are rough at a microscopic scale set by the monomer size ℓ_0. Meanwhile, the potential energy varies at a scale set by the lattice constant a, which can be much larger than the monomer size. In the limit that $a \gg \ell_0$, the lattice-scale features of the chain conformations can be described using a coarse-grained model in which monomers are aggregated into mesoscopic segments. Each segment is small enough such that its local environment is more or less homogeneous, but large enough that its fluctuations obey Gaussian statistics [33]. This coarse-graining effectively smoothens out the monomer-scale roughness (as depicted schematically in Fig. 2.1) burying microscopic degrees of freedom in a multiplicative constant for the partition function (additive constant for the entropy) which does not affect the equilibrium properties.

For each polymer chain, labeled by the index $1 \leq n \leq N$, the instantaneous coarse-grained conformation is then specified by a smooth function $x_n(\tau)$ with $\tau \in [0, L]$ where L is the length of each polymer. The total energy, at small angles $\theta \ll 1$ and small chain slopes $\partial_\tau x_n \ll 1$, is [16, 30, 69, 81]

$$E = \sum_{n=1}^{N} \int_0^L d\tau \biggl(\frac{F}{2} (\partial_\tau x_n - \theta)^2 + V(x_n) + \sum_{n' \neq n} |c| \delta(x_n - x_{n'}) \biggr). \tag{2.1}$$

The first term in the integrand captures the energy cost of the chain deviating from a straight line aligned with the force direction. For the coarse-grained description to hold, the transverse fluctuations due to thermal energy at the monomer scale must be small compared to the lattice spacing. The energy associated with a deflection of order δ over a length ℓ_0 is order $F(\delta/\ell_0)^2 \times \ell_0 \sim F\delta^2/\ell_0$. The typical deflection δ_{th} due to thermal fluctuations is obtained by balancing this energy against the thermal energy scale $k_B T$, which gives $\delta_{\text{th}} \sim \sqrt{k_B T \ell_0 / F}$. In all our simulations, parameters are chosen such that $\delta_{\text{th}} \ll a$.

The second term in Eq. (2.1) implements the position-dependent substrate potential, where $V(x)$ is the potential energy per unit length of the chain experienced at position x. The coarse-grained description in the theory and the microscopic description in simulations are matched by setting $V = V_{\text{m}}/\ell_0$, where V_{m} is the potential energy experienced by each monomer.

The last term in Eq. (2.1) incorporates interactions among chains, which are assumed to be entirely local so that chain segments interact only when $x_n(\tau) = x_{n'}(\tau)$ [16]. In this work, the only interaction we will consider is that polymers cannot cross each other, which is implemented by taking the limit $|c| \to \infty$. As pointed out by de Gennes [14], for noncrossing polymers we can use Girardeau's mapping [91] to eliminate the interaction term from the energy and absorb its effect into the boundary conditions of the probability density functions describing the polymers. We will exploit this feature in the theoretical treatment below (see Eq. (2.7)). In simulations, the noncrossing condition is implemented by including extremely stiff contact forces among monomers whose radius is ℓ_0, so that monomers cannot pass through the gaps between pairs of monomers on other chains. Prior work on a related system [84] showed that when ℓ_0 is small, the statistics of such monomer chains quantitatively match theoretical expectations from idealized noncrossing lines.

We now derive a Schrödinger-like equation governing the probability weights associated with the chain conformations at thermal equilibrium. Our approach augments the continuum treatment of shear-free ($\theta = 0$) directed polymers in Refs. [14, 16] to include the effects of a periodic substrate potential [84] and of shear forces following the Hatano-Nelson model [15, 65]. Consider the conformation of any one of the N polymer chains, $x(\tau')$, and assume it is pinned at two points, $\tau' = 0$ and $\tau' = \tau$, so that $x(0) = x_0$ and $x(\tau) = x_\tau$. The energy of the fragment between the points is denoted by $E[x; 0, \tau]$. The partition function of this fragment can be written as a path integral [92] over all paths obeying the pinning constraints,

$$\Psi(x_\tau, x_0, \tau) = \int_{(x_0,0)}^{(x_\tau,\tau)} \mathcal{D}x \exp(-\beta E[x; 0, \tau]), \tag{2.2}$$

where ($\beta = 1/k_B T$). By considering the change in the partition function between the vertical coordinates τ and $\tau + \epsilon$ in the limit $\epsilon \to 0$ (see details in Appendix A.3), we find that it satisfies the following diffusion equation:

$$\frac{\partial \Psi(x, \tau)}{\partial \tau} = \left(\frac{1}{2\beta F} \frac{\partial^2}{\partial x^2} - \theta \frac{\partial}{\partial x} - \beta V(x) \right) \Psi(x, \tau), \tag{2.3}$$

where the linear differential operator in the brackets will take the role of a Hamiltonian upon mapping to quantum mechanics. The partition function $\Psi(x_\tau, x_0, \tau)$ with some modifications will help us retrieve the probability distribution $p(x, \tau)$ of finding the point τ along the chain at horizontal coordinate x.

The transformation from Eq. (2.2) to Eq. (2.3) is formally similar to the transformation from the Feynman path integral, $\int \mathcal{D}x \exp(iS[x]/\hbar)$, to the Schrödinger formalism in quantum mechanics. Indeed, if we redefine variables by mapping $\tau = it$, $\beta = \frac{1}{\hbar}$, $F = m$, and $F\theta = g$, Eq. (2.3) maps to the time-dependent Schrödinger equation,

$$i\hbar\frac{\partial\Psi(x,t)}{\partial t} = \left(\frac{(p+ig)^2}{2m} + \frac{g^2}{2m} + V(x)\right)\Psi(x,t) \tag{2.4}$$

$$\equiv \left(\mathcal{H}(g) + \frac{g^2}{2m}\right)\Psi(x,t), \tag{2.5}$$

where $p = -i\hbar\frac{\partial}{\partial x} = -\frac{i}{\beta}\frac{\partial}{\partial x}$. The nonzero shear component of the forces on the chains manifests itself as an imaginary vector potential $ig = F\theta$ [15]. We identify the Hamiltonian to be $\mathcal{H}(g)$ shifted by a constant, $\frac{g^2}{2m}$; where $\mathcal{H}(g)$ is the continuum version of the periodic Hatano-Nelson Hamiltonian which has been well-studied in the tight-binding limit [77].

The procedure can be repeated for the full many-body system with the path integral now involving all possible conformations of the N chains. The mapped many-body quantum system then has a Hamiltonian [16, 65],

$$\mathbf{H} = \sum_{n=1}^{N}\left(\frac{(p_n+ig)^2}{2m} + \frac{g^2}{2m} + V(x_n) + \sum_{n'\neq n}|c|\delta(x_n - x_n')\right), \tag{2.6}$$

where $p_n = -i\hbar\frac{\partial}{\partial x_n} = -\frac{i}{\beta}\frac{\partial}{\partial x_n}$. This Hamiltonian describes a one-dimensional system of N quantum particles in a periodic potential $V(x)$ acted upon by a common imaginary vector potential ig. Now, we impose the restriction $|c| \to \infty$, which corresponds to the noncrossing interaction. In this limit, the interaction term can be absorbed into the boundary conditions of the many-body wave function [14] using Girardeau's mapping [91] which effectively maps bosons with contact repulsion to *non*-interacting fermions. By considering only fermionic many-body wavefunctions, the noncrossing condition is automatically satisfied. The many-body Hamiltonian then becomes a sum of single-body terms,

$$\mathbf{H} = \sum_{n=1}^{N} \left(\mathcal{H}_n(g) + \frac{g^2}{2m} \right). \tag{2.7}$$

The statistics of N noncrossing, fluctuating lines has been mapped to a quantum mechanical problem of noninteracting fermions, each experiencing the same periodic scalar potential V and constant imaginary vector potential ig.

2.3.2 Eigenstates and ground-state dominance

Besides simplifying the description of many-body densities which automatically satisfy the noncrossing condition, the mapping to quantum mechanics motivates the use of a spectral expansion to represent the solution to Eq. (2.3). A general solution to a linear differential equation such as Eq. (2.3) can be written as a superposition of eigenfunctions $\Psi_m(x)$ of the Hamiltonian,

$$\Psi(x,\tau) = \sum_m c_m e^{-\beta(\varepsilon_m + \frac{F\theta^2}{2})\tau} \Psi_m(x), \tag{2.8}$$

where

$$\mathcal{H}(g)\Psi_m(x) = \left(\frac{(p+ig)^2}{2m} + V(x) \right) \Psi_m(x) = \varepsilon_m \Psi_m(x) \tag{2.9}$$

for some quasienergy eigenvalue ε_m, and c_m are constants fixed by the initial condition $\Psi(x,0)$. We will index the eigenfunctions in increasing order of the real part of the quasienergy, $\operatorname{Re}\varepsilon_{m'} > \operatorname{Re}\varepsilon_m$ for $m' > m$. As the coordinate along the polymer increases from $\tau = 0$, the amplitudes of eigenstates relative to the "ground state" ($m = 0$) decay exponentially as $e^{-\beta \operatorname{Re}(\varepsilon_m - \varepsilon_0)\tau}$. Far from the boundary, the polymer's profile is dominated by the ground-state wave function of the time-independent

Hamiltonian with the lowest real component of ε_m,

$$\Psi(x,\tau) \sim e^{-\beta(\varepsilon_0+\frac{F\theta^2}{2})\tau}\Psi_0(x),$$

a situation termed *ground state dominance* [93]. Ground state dominance holds in the interior of polymers with lengths that satisfy $L \gg 1/[\beta(\mathrm{Re}\,\varepsilon_1 - \mathrm{Re}\,\varepsilon_0)]$; the lower the real energy gap between the lowest two quasienergies, the longer the polymer needs to be.

To describe the density profiles of polymers away from the ends, we also need the contribution to the partition function of a polymer being pinned at $x(L) = x_L$ and propagating *downwards*. We will write this partition function contribution as,

$$\widetilde{\Psi}(x_\tau, x_L, \tau) = \int_{(x_L,L)}^{(x_\tau,\tau)} \mathcal{D}x \exp(-\beta E[x;\tau,L]). \tag{2.10}$$

The diffusion equation obeyed by $\widetilde{\Psi}$ is obtained by rotating the coordinate system $(x,\tau) \to (-x,-\tau)$ in Eq. (2.3), leading to

$$\frac{\partial\widetilde{\Psi}(x,\tau)}{\partial\tau} = \left(-\frac{1}{2\beta F}\frac{\partial^2}{\partial x^2} - \theta\frac{\partial}{\partial x} + \beta V(x)\right)\widetilde{\Psi}(x,\tau). \tag{2.11}$$

On repeating the quantum mapping, and assuming an even potential, $V(-x) = V(x)$, we get,

$$-i\hbar\frac{\partial\widetilde{\Psi}(x,t)}{\partial t} = \left(\frac{(p-ig)^2}{2m} + \frac{g^2}{2m} + V(x)\right)\widetilde{\Psi}(x,t) \tag{2.12}$$

$$= \left(\mathcal{H}(g)^\dagger + \frac{g^2}{2m}\right)\widetilde{\Psi}(x,t). \tag{2.13}$$

Note the reversed sign of time. We now expand $\widetilde{\Psi}$ using the eigenfunctions of $\mathcal{H}(g)^\dagger$ as $\widetilde{\Psi}(x,\tau) = \sum_m \tilde{c}_m e^{-\beta(\tilde{\varepsilon}_m+\frac{F\theta^2}{2})(L-\tau)}\widetilde{\Psi}_m(x)$, where

$$\mathcal{H}(g)^\dagger\widetilde{\Psi}_m(x) = \left(\frac{(p-ig)^2}{2m} + V(x)\right)\widetilde{\Psi}_m(x) = \tilde{\varepsilon}_m\widetilde{\Psi}_m(x)$$

and the coefficients $\tilde{c}_m$ are fixed by the boundary condition at $\tau = L$.

Although $\mathcal{H}(g) \neq \mathcal{H}(g)^\dagger$ because of the non-Hermiticity induced by a finite force angle, the eigenfunctions and eigenvalues of the Hamiltonians in Eq. (2.4) and

Eq. (2.12) are closely related. A diagonalizable non-Hermitian Hamiltonian can be written as [21]

$$H = \sum_n \lambda_n |R_n\rangle\langle L_n|, \tag{2.14}$$

where the right eigenstates, $|R_n\rangle$, and the left eigenstates, $\langle L_n|$, form a biorthonormal basis, $\langle L_i|R_j\rangle = \delta_{ij}$. By taking the conjugate transpose of the above equation, we get

$$H^\dagger = \sum_n \lambda_n^* |L_n\rangle\langle R_n|.$$

We identify $\Psi_m(x) = \langle x|R_m\rangle$ and $\widetilde{\Psi}_m(x) = \langle x|L_m\rangle$ such that $\tilde{\varepsilon}_m = \varepsilon_m^*$ and $\int dx\, \widetilde{\Psi}_m^*(x)\Psi_n(x) = \delta_{mn}$. Now, since $\mathcal{H}(g)$ (as well as $\mathcal{H}(g)^\dagger$) is real-valued, its eigenstates are either real with real eigenvalues, or come in complex-conjugate pairs. Using this, we choose to index the eigenstates $\widetilde{\Psi}_m(x)$ such that,

$$\int_0^{L_x} dx\, \widetilde{\Psi}_m(x)\Psi_n(x) = \delta_{mn} \quad \text{and} \quad \tilde{\varepsilon}_m = \varepsilon_m \tag{2.15}$$

In particular, the ground state has a real eigenvalue even for the non-Hermitian problem [65], and far from the upper end of the polymer we obtain

$$\widetilde{\Psi}(x,\tau) \sim e^{-\beta(\varepsilon_0 + \frac{F\theta^2}{2})(L-\tau)}\widetilde{\Psi}_0(x).$$

The polymer density is expressed in terms of the two partition function contributions as

$$p(x,\tau) = \frac{1}{Z}\Psi(x,x_0,\tau)\widetilde{\Psi}(x,x_L,\tau), \tag{2.16}$$

where $Z = \int dx\, \Psi(x,x_0,\tau)\widetilde{\Psi}(x,x_L,\tau) = \Psi(x_L,x_0,L)$ is the full partition function of the chain with end points $(x_0,0)$ and (x_L,L) and is therefore independent of the x and τ coordinates. While $p(x,\tau)$ can be expanded in terms of the eigenfunctions $\Psi_m(x)$ and $\widetilde{\Psi}_m(x)$, we operate in the limit of long polymer chains where the density far from the ends is dominated by the ground state:

$$p(x,\tau) \sim \Psi_0(x)\widetilde{\Psi}_0(x). \tag{2.17}$$

These quantities are readily translated to the corresponding many-body quantities. Using Girardeau's mapping [91], the many-body eigenstate, $\Psi(\boldsymbol{x}) = \Psi(x_1, x_2, ..., x_N)$, of the Hamiltonian in Eq. (2.6) is the Slater determinant of the single-body wave functions Eq. (2.19) (see Appendix A.4 for details). The Slater determinant ensures that $\Psi(x_1, x_2, ..., x_N) = 0$ whenever any $x_i = x_j$, thus enforcing the noncrossing condition. The associated energy, is the sum of the single-particle eigenenergies of states in the Slater determinant, $\boldsymbol{\varepsilon} = \sum_i \varepsilon_i$. The many-body ground state, which determines the polymer profiles away from the ends, is therefore the Slater determinant of the lowest N single-particle eigenstates. The analogue of Eq. (2.17) for the many-body probability density over the polymer chain coordinates $\boldsymbol{x} = (x_1, x_2, \ldots, x_N)$ at any τ as,

$$p(\boldsymbol{x}; \tau) = \frac{1}{Z} \Psi(\boldsymbol{x}, \tau) \widetilde{\Psi}(\boldsymbol{x}, \tau) \sim \Psi_0(\boldsymbol{x}) \widetilde{\Psi}_0(\boldsymbol{x}). \tag{2.18}$$

2.3.3 Imaginary gauge transformation and the delocalization transition

The problem of finding the polymers' density profile has reduced to finding the lowest N eigenstates of the Hamiltonian Eq. (2.9) (ordered by the real part of the quasienergy). To do so, we use the fact that if $\Psi'(x)$ is an eigenstate of the shear-less Hamiltonian, $\mathcal{H}(g = 0) = \frac{p^2}{2m} + V(x)$ with eigenvalue ε, then $\Psi(x) = e^{\frac{gx}{\hbar}} \Psi'(x) = e^{F\beta\theta x} \Psi'(x)$ is an eigenstate of $\mathcal{H}(g)$ with the same eigenvalue. (This is analogous to a gauge-transformation of the vector-potential [94].)

When $V(x)$ is periodic, Bloch's theorem applies and the eigenfunctions $\Psi'_k(x)$ should be of the form $e^{ikx} u_k(x)$ with $u_k(x)$ having the same periodicity as the potential, i.e., $u_k(x + a) = u_k(x)$. However, to ensure that $\Psi(x)$ is physical (in particular that it obeys periodic boundary conditions) we must choose k to be complex such that $\mathrm{Im}(k) = g/\hbar = F\beta\theta$ to cancel out the 'gain factor' $e^{\frac{g}{\hbar}x} = e^{F\beta\theta x}$. The single-particle, normalizable eigenstates of $\mathcal{H}(g)$ are then

$$\Psi(x) = \Psi_k(x) = e^{i\,\mathrm{Re}(k)x} u_k(x), \tag{2.19}$$

with $k = \mathrm{Re}(k) + iF\beta\theta$. Such Bloch waves with complex k have been used to describe the evanescent surface states of a finite crystal [35, 95, 96] and more recently to elucidate the non-Hermitian skin effect [54, 97].

The essential physics of the nonzero tilt angle for polymer conformations is captured in the localization, or lack thereof, of the fermionic ground states constructed from the Bloch waves. A superposition of N Bloch waves is generically delocalized through the whole lattice and has equal weight on all unit cells. The equilibrium density profile of the polymer far from the ends is therefore uniform across the system: the polymer wanders freely and visits each groove with equal probability over long times. The wandering polymer aligns its conformation to the force angle to minimize its free energy, leading to a conformational tilt which grows with tilt angle as observed in simulations.

An exception to the generic delocalized state occurs under commensurate filling of one polymer per groove of the periodic potential. At zero shear, appropriate superpositions of the Bloch waves can be used to construct an alternate basis for the lowest band, consisting of a set of Wannier functions

$$\Phi'_j(x) = \Phi'(x - ja),$$

each centered on the jth unit cell of the periodic potential and exponentially localized in the x direction, $\Phi'(x) \sim \exp(-\lambda|x|)$ [3, 98]. Here, $\lambda > 0$ is an inverse localization length determined by features of the *complex* band structure $\varepsilon(k)$.

Once we have identified an exponentially localized set of basis states, the mechanism of how shear causes delocalization can be framed in a very general manner using the imaginary gauge transformation [65, 66]. Consider a many-body Hermitian (shear-free) system, $\boldsymbol{H}(g=0)=\sum_n \frac{p_n^2}{2m}+V(\boldsymbol{x})$. The potential energy, $V(\boldsymbol{x})$, might be either periodic (as in the current problem), or disordered, or both. It may even have possible interaction terms. Regardless of the localization mechanism, if the many-body ground-state of the shear-free system $\boldsymbol{\psi}'(\boldsymbol{x};g=0)$ is exponentially localized, the effective eigenstate of each polymer chain dies off away from its mean/typical position as $\Psi'(x)\sim\exp(-\lambda|x|)$ where $\lambda>0$ is the many-body inverse localization length [98, 99]. Using the gauge transformation, we see that in the presence of shear, the many-body (right) ground-state is $\boldsymbol{\psi}(\boldsymbol{x};g)=e^{F\beta\theta\sum_n x_n}\boldsymbol{\psi}'(\boldsymbol{x};g=0)$. The gauge transform is permissible as long as $e^{F\beta\theta x}\Psi(x)$ is well-behaved, i.e., it still must satisfy the periodic boundary conditions. This condition is met as long as $\lambda>F\beta\theta$. The critical shear at which delocalization happens is then $F\theta_c=\frac{\lambda}{\beta}$ (compare with the conductivity expression in Ref. [100]). If the density profiles of chains in the shear-free many-body ground state $\boldsymbol{\psi}'(\boldsymbol{x};g=0)$ fall off faster than exponentially with distance from the mean chain position [for example, as a Gaussian profile $\psi'(x)\sim\exp(-\lambda^2x^2)$ which decays faster than any exponentially decaying function at large enough x], then no amount of shear will delocalize the system. By contrast, if the localization is weaker than an exponential falloff (for example, as a power-law decay with distance from the mean position), then an infinitesimal amount of shear is sufficient to delocalize the system.

Finding the localization length in the Hermitian problem is, thus, equivalent to finding the critical shear in the non-Hermitian problem. Conversely, finding the critical shear, either experimentally or theoretically, in the non-Hermitian system is equivalent to finding the localization length in an exponentially localized Hermitian system. In our specific system, this localization length is precisely that of the Wannier functions at commensurate filling, which we explicitly calculate in Sec. 2.3.4. Interestingly, the effect of the shear force on the polymer density profiles themselves is minimal in the localized phase. Observing that the right eigenstate in the non-Hermitian system falls off as $\sim e^{F\beta\theta x}\exp(-\lambda|x|)$, the inverse localization length in the sheared system appears to be $\lambda - F\beta\theta$. This is, however, the inverse localization length of the right eigenstate only. The polymer's probability profile consists of the product of both the right and the left eigenstate [Eq. (2.16)]. The left eigenstate of $\mathcal{H}(g)$ is the right eigenstate of $\mathcal{H}(g)^\dagger = \mathcal{H}(-g)$ which suffers an opposite gauge transformation. The inverse localization length of the polymer density profiles under shear, obtained by multiplying the left and right ground states [Eq. (2.17)], is then the same as that of a system without shear ($\theta = 0$). Away from the polymer ends, non-Hermiticity does not affect polymer density profiles in the localized phase [66].

We note that the gauge transformation of a localized non-Hermitian system to a localized Hermitian system is not possible in a tight-binding (discrete) model such as the lattice-based Hatano-Nelson model with a periodic potential [77]. Indeed, there is no similarity transformation that maps a generic non-Hermitian matrix with complex eigenvalues to a Hermitian matrix. A key difference between discrete and continuum models is that boundary conditions are part of the operator itself in the former but not in the latter. For the continuum model, we have to adjust the boundary conditions of the mapped Hermitian system to ensure the original non-Hermitian system has periodic boundary conditions. When the many-body non-Hermitian phase is localized, the Hermitian phase is localized as well, and we can retain periodic boundary conditions ensuring the mapped Hamiltonian is Hermitian as well as self-adjoint. In the delocalized phase, we are forced to place special nonperiodic boundary conditions in the mapped Hermitian problem such that the operator is no longer self-adjoint. A continuum Hermitian operator with an infinite-dimensional Hilbert space can have complex eigenvalues if it is not self-adjoint [101, 102]; this fact explains the complex eigenenergies in our system even though it can be mapped to a Hermitian Hamiltonian. The gauge transformation also allows us to make use of the well-studied properties of the analytical continuation of the Hermitian spectrum [3] which is essentially the spectrum of the Hermitian operator under modified (nonperiodic) boundary conditions.

Having identified the mechanism for delocalization in the system under commensurate filling, we now turn to analyzing the energy spectrum, $\varepsilon(k)$, to determine the value of the critical force angle; we also compute the tilt angle of the polymers from the corresponding eigenfunctions.

2.3.4 Non-Hermitian gap closure and critical shear

At finite shear, the quasienergies of the eigenstates become complex-valued since the Hamiltonian is non-Hermitian, $\mathcal{H}(g)^\dagger = \mathcal{H}(-g) \neq \mathcal{H}(g)$. The complex energy bands, $\varepsilon_n(k)$, can be regarded as distinct Riemann sheets over the complex k plane of a multivalued complex function $\varepsilon(k)$ [3, 4, 35] with each sheet corresponding to a particular band. (When used with an argument k, the expression $\varepsilon_n(k)$ denotes the nth energy band associated with the periodic potential; bands are ordered according to the real part of the energy.) While the bands are separated for real k, adjacent sheets meet at branch points of $\varepsilon(k)$ which occur at complex k: The nth sheet meets the $(n+1)$th sheet at wave-vector values $k_n = \pm\frac{\pi}{a} \pm i\frac{\mu_n}{a}$, where the dimensionless numbers μ_n, which quantify the distances of the branch points from the real k axis,

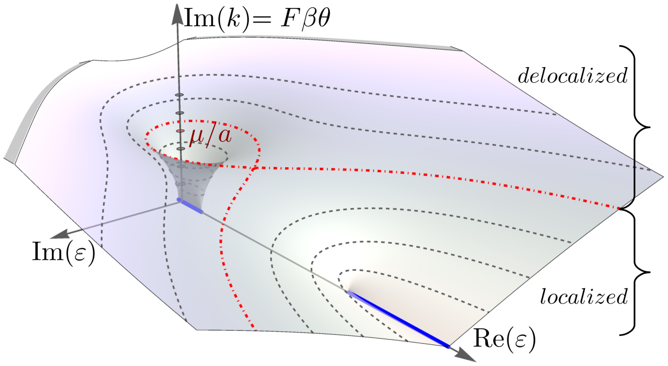

Figure 2.3. The (complex-valued) energies, ε, of the Hamiltonian $\frac{p^2}{2m} + V(x)$, where $V(x)$ is periodic, as a function of the imaginary component of the Bloch wave-vector, Im(k), the value of which is set by the shear force $F\theta$ and temperature β in the polymer system. When Im(k) $= 0$, the energies are real and form separate bands (shown in blue). As the shear force is increased Im(k) increases and the energies form complex-valued ovals (grey dotted contours). At the critical value of Im(k) $= \mu/a$ the ground-state oval meets the first excited band and a commensurate filled crystal is no longer a band insulator. This is the delocalization mechanism exhibited by the polymer system. While the complex energies shown here have been computed for the specific potential $V(x) = V_0 \cos(2\pi x/a)$, with $V_0 = 1$ (see Appendix A.5 for computation details), this behaviour is generic for even one-dimensional potentials with $V(x) = V(-x)$ and are expected to hold with some modifications for nonsymmetric periodic potentials as well [3, 4].

are determined by the potential function $V(x)$. The values of μ_n will determine the value of the critical shear in our system.

In the polymer model, commensurate filling ensures that the quantum particles completely fill the groundstate energy band $\varepsilon_0(k)$. At $F\theta = 0$, when there is no shear, the energies are real and there is a finite gap between the groundstate band and the higher band. At nonzero shear force $F\theta$, the bands become complex-valued and turn into ovals in the complex plane. As $F\theta$, and therefore Im(k), increases, these oval energy bands grow in size (Fig. 2.3) and the separation between bands $\varepsilon_0(k)$ and $\varepsilon_1(k)$ is reduced as the branch point at k_0 is approached (Fig. 2.3). When the shear force equals the branch point value, $F\beta\theta = \mu_0/a$, the ground state energy band meets the higher band. The energy gap closes and the system at commensurate filling is now

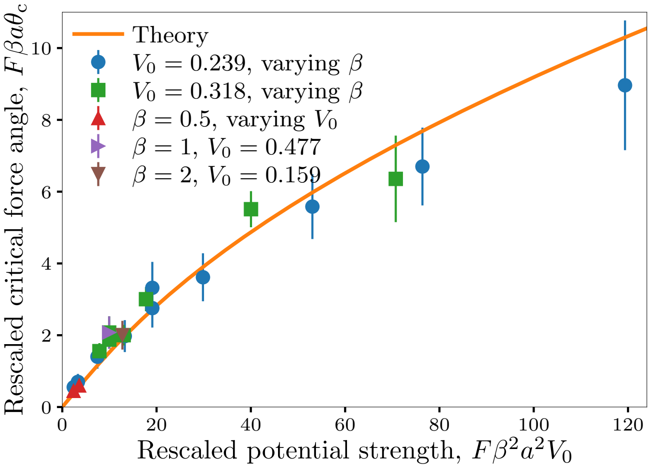

Figure 2.4. Critical force angles measured from simulations with different potential amplitudes and temperatures, rescaled by the energy and force scales governing the underlying Schrödinger equation [Eq. (2.21)]. Symbols are labeled according to the parameter which is kept constant in distinct sets of simulations. The other parameters are $F = 20$, $a = 1$, $N = 10$ in simulation units. Error bars show uncertainty in the critical force estimate due to the finite sampling resolution of applied shear forces. Solid curve shows the theoretical prediction, Eq. (2.20).

a conductor that enables probability flows driven by the imaginary vector potential. These probability flows manifest themselves as tilts in the polymer density profiles, Fig. 2.2.

The critical angle of force, θ_c, at which the polymers acquire a collective tilt (Fig. 2.2) is therefore predicted to be

$$\theta_c = \frac{\mu_0}{F\beta a}. \tag{2.20}$$

Notably, the value of μ_n is sensitive to the details of the continuous periodic potential; its dependence on the energy gap or the amplitude of the potential energy is nonuniversal [103, 104]. This subtlety is not captured by tight-binding studies of the complex band structure [77], which gloss over the details of the periodic potential and suggest that θ_c should scale with the energy gap in a universal manner.

One can transform x to the dimensionless coordinate $r = x/a$ (where a is the lattice constant) in Eq. (2.9). Upon rescaling the wavefunction to a new variable $\Psi'_n(r) \equiv \Psi_n(r)e^{-F\beta\theta ar}$ we get,

$$-\frac{1}{2}\frac{\partial^2}{\partial r^2}\Psi'_n(r) + V_0F\beta^2a^2V'(r)\Psi'_n(r) = \varepsilon_nF\beta^2a^2\Psi'_n(r), \tag{2.21}$$

where V_0 is the amplitude of the periodic potential and $V'(r) \equiv V(r)/V_0$. For a particular functional form of the rescaled potential $V'(r)$, the system is then governed by two dimensionless quantities: the dimensionless shear force, $F\beta\theta a$ and the generalized potential strength, $V_0F\beta^2a^2$. In Fig. 2.4 we report measurements of θ_c from molecular dynamics simulations in which the parameters β and V_0 were varied for our choice of potential $V'(r) = \cos(2\pi r)$. We find that delocalization thresholds from simulations covering a broad range of parameter values collapse onto a narrow region in the force angle-potential strength plane when rescaled according to the quantum mapping. Furthermore, the rescaled critical force angles are consistent with the theoretical prediction of the localization-delocalization transition—the branch point distance μ_0 at the given potential amplitude [Eq. (2.20)]. The agreement does not involve any fitting parameters, and is robust to changes in the numerical estimation of the critical force angle from simulations (see Appendix A.2).

Although we only considered a system with commensurate filling in our simulations, the non-Hermitian band structure also determines the delocalization behavior for other filling densities $f = N/M$ (where $M = L_x/a$ is number of unit cells) of the polymers. When f is noninteger the polymers are expected to be generically delocalized because there is no energy gap separating the last occupied single-particle state from the first unoccupied state. By contrast, when f is an integer the system exhibits a transition from a localized to delocalized state at a critical force angle given by $\frac{\mu_f}{F\beta a}$.

The delocalization transition due to closure of the non-Hermitian energy gap is also apparent in the behaviour of the wave functions for filled bands. We can write the many-body wave function of the commensurate system as a real-valued Slater determinant of Wannier functions defined on the ground state band (see Appendix A.4). The Wannier functions of the nth band, at zero shear, are also known to depend on the branch point locations μ_n: their spatial profiles fall off as $\sim \exp(-\mu_n x/a)$ at large x [3, 98]. Delocalization of the wavefunctions is then linked to the threshold at which the "gain factor" $e^{\frac{gx}{\hbar}}$ exceeds the falloff $e^{\frac{\mu_n x}{a}}$, recovering the prediction for the critical angle, $\mu_n/a = g_c/\hbar = F\beta\theta_{\mathrm{c}}$.

The exponential falloff of the Wannier functions is known to include a power-law prefactor [105]: the complete functional form for the large-x behavior is $\Phi'(x) \sim x^{-\alpha}\exp(-\mu_n x/a)$ for the shear-free system. Right at the transition point, the gain factor cancels the exponential decay and it is the power-law falloff that survives. The exponent for the falloff, α, is derived from the analytic properties of $\varepsilon(k)$ for 1D periodic potentials, is known to be universal, and equals 3/4 [105]. This feature provides a critical exponent for the phase transition—at the critical point, the polymers' probability density in the bulk is expected to fall off as $\rho(x) \sim [e^{\frac{g_c x}{\hbar}}\Phi'(x)]^2 \sim x^{-3/2}$, independently of the details of the periodic potential.

2.3.5 Critical exponent of diverging shear modulus

In the vicinity of the branch points of the energy surface, the imaginary part of the energy is known to vary as as $\varepsilon(k) \sim |\operatorname{Im}(k) - \operatorname{Im}(k_n)|^{1/2}$ [35]. This dependence suggests a universal divergence in the shear response of the system near the critical force angle. We can define the shear modulus, Γ, of the system as the applied stress, $F\theta/a$, divided by the resulting strain, ϕ. Fig. 2.2 shows that for a commensurate system, $\Gamma = F\theta/(a\phi)$ equals F/a at $\theta \gg \theta_\mathrm{c}$. As θ approaches θ_c from above, ϕ decreases faster than θ so that θ/ϕ, and hence Γ, diverges as $\theta \to \theta_\mathrm{c}$. For commensurate filling we therefore expect,

$$\phi \propto \begin{cases} 0 & \text{if } \theta \ll \theta_\mathrm{c}, \\ (\theta - \theta_\mathrm{c})^\eta & \text{if } \theta \sim \theta_\mathrm{c}, \\ \theta & \text{if } \theta \gg \theta_\mathrm{c}, \end{cases} \tag{2.22}$$

for some critical exponent η which we find to be $\frac{1}{2}$ in the following.

The tilt of the polymer chains, ϕ, can be measured by the averaged slope of the polymer configurations,

$$\phi(\tau) \sim \overline{\langle \partial_\tau x_n \rangle} = \frac{1}{N} \sum_{n=1}^{N} \int_0^{L_x} d\boldsymbol{x}\, x_n \frac{\partial p(\boldsymbol{x}, \tau)}{\partial \tau}, \tag{2.23}$$

where the overline denotes averaging over the N polymers. The tilt, $\phi(\tau)$, depends on the coordinate τ because of the influence from the initial conditions at $\tau = 0$ and $\tau = L$. Indeed in Fig. 2.2**e,f** we see that the polymers' density profile shows a small amount of bending near the ends. We will be interested in the value of ϕ in the bulk of the polymer system, that is at large values of τ and $L - \tau$. In this regime, the ground state dominance applies such that $(\Psi, \widetilde{\Psi}) \to (\Psi_0, \widetilde{\Psi}_0)$ and we find that the local tilt angle, $\phi(\tau)$ becomes a constant (see Appendix A.6.1 and Refs. [15, 65]),

$$\phi \sim \overline{\langle \partial_\tau x_n \rangle} = -\frac{1}{NF} \frac{\partial \boldsymbol{\varepsilon}_0}{\partial \theta}. \tag{2.24}$$

Here, $\boldsymbol{\varepsilon}_0$ is the many-body groundstate energy which is the sum of the lowest N single-body energies,

$$\boldsymbol{\varepsilon}_0 = \sum_{i=1}^{N} \varepsilon_i. \tag{2.25}$$

At commensurate filling and large N, the sum of single-particle energies that yields the many-body groundstate energy can be written in the form of an integral over the

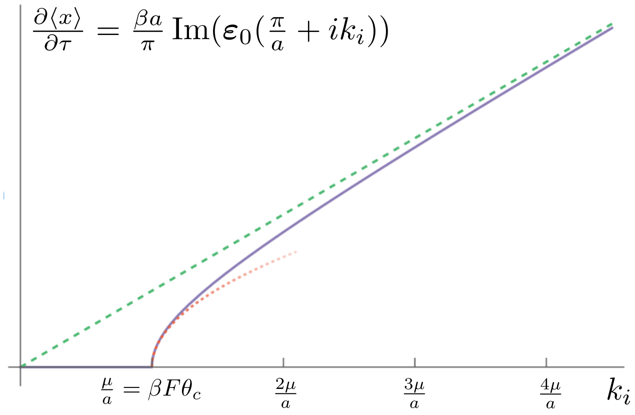

Figure 2.5. The theoretically predicted ϕ vs. θ graph for a commensurate polymer system. By Eq. (2.29), the tilt of the polymer chains, at shear value of $F\theta$ and temperature $1/\beta = k_BT$, is given by $\frac{\beta a}{\pi}\,\mathrm{Im}\,\varepsilon(k)$ with $k = \frac{\pi}{a} + iF\beta\theta := \frac{\pi}{a} + ik_i$. Shown is the numerically computed value of this expression (blue solid line) for a cosine potential, $V(x) = \cos(2\pi x/a)$. The green dashed line is $\phi = \theta = \frac{k_i}{F\beta}$, to which the tilt asymptotically tends to at large shear; the red dotted curve is $c(k_i - \frac{\mu}{a})^{\frac{1}{2}}$, demonstrating the critical exponent is $\frac{1}{2}$ (the value of c is set by fitting). As predicted, the tilt is exactly zero below the critical shear [Eq. (2.29)].

complex-valued energy band $\varepsilon_0(k)$:

$$\boldsymbol{\varepsilon}_0 = \int_C \frac{dk}{2\pi/(Na)}\,\varepsilon_0(k) = \int_C \frac{dk}{2\pi/(Na)}\;\mathrm{Re}(\varepsilon_0(k)), \tag{2.26}$$

where the complex contour C is the line segment connecting $k = -\pi/a + i\beta F\theta$ to $k = \pi/a + i\beta F\theta$ at constant $\mathrm{Im}(k) = \beta F\theta$. In the last step, we used the fact that since the single-body eigenvalues are either real or occur in complex conjugate pairs, the many-body ground state energy for a filled band is guaranteed to be real.

Using Eq. (2.24), the average tilt angle far away from the polymer ends is given by

$$\begin{aligned}\phi = -\frac{1}{NF}\frac{\partial\boldsymbol{\varepsilon}_0}{\partial\theta} &= -\frac{1}{NF}\int_C \frac{dk}{2\pi/(Na)}\,\frac{\partial\,\mathrm{Re}(\varepsilon_0(k))}{\partial\theta} \\ &= -\frac{\beta a}{2\pi}\int_C dk\,\frac{\partial\,\mathrm{Re}(\varepsilon_0(k))}{\partial\,\mathrm{Im}(k)}.\end{aligned} \tag{2.27}$$

Note that the line element dk involves variations only in $\mathrm{Re}(k)$, so we can safely apply the derivative to the integrand. We now use the fact that the complex energy function corresponding to the lowest band, $\varepsilon_0(k)$, is a Riemann sheet of a multivalued function $\varepsilon(k)$ and is analytic everywhere away from the branch points at $k_0 = \pm\frac{\pi}{a} \pm i\frac{\mu_0}{a}$ which are encountered only when $\theta = \theta_{\mathrm{c}}$ [3]. As a result, away from the critical angle the Cauchy-Riemann equations for the analytic function $\varepsilon_0(k)$ can be used to rewrite Eq. (2.27) as

$$\begin{aligned}\phi &= \frac{\beta a}{2\pi}\int_C dk\,\frac{\partial\,\mathrm{Im}(\varepsilon_0(k))}{\partial\,\mathrm{Re}(k)} \\ &= \frac{\beta a}{2\pi}\left[\mathrm{Im}\left(\varepsilon_0\left(\frac{\pi}{a}+i\beta F\theta\right)\right) - \mathrm{Im}\left(\varepsilon_0\left(-\frac{\pi}{a}+i\beta F\theta\right)\right)\right], \\ &= \frac{\beta a}{\pi}\,\mathrm{Im}\left(\varepsilon_0\left(\frac{\pi}{a}+i\beta F\theta\right)\right). \end{aligned} \tag{2.28}$$

In the last line we used the fact that $\varepsilon_0(-k^*) = \varepsilon_0^*(k)$ since the Hamiltonian is real [3].

Now for $\theta < \theta_c$, the integration contour C traces a complete loop of the closed oval corresponding to the lowest band in Fig. 2.3, such that $\varepsilon_0(k)$ evaluates to the same value at the endpoints of the contour and the value of the integral, Eq. (2.27), is identically zero. For $\theta > \theta_c$, the closed oval corresponding to the lowest band 'opens up' by merging with the higher band. The size of the opening along the $\mathrm{Im}(\varepsilon)$ direction is proportional to the acquired tilt via Eq. (2.28). Near the branch point, $k_0 = \pi/a + iF\beta\theta_c$, it is known that $\mathrm{Im}\left(\varepsilon_0\left(\frac{\pi}{a}+i\beta F\theta\right)\right)$ behaves like $\sqrt{\theta-\theta_c}$ since the branch point is always of order one [3]. Finally, for very large values of θ, the momentum term of the Hamiltonian dominates the potential term and we can show that $\mathrm{Im}\left(\varepsilon_0\left(\frac{\pi}{a}+i\beta F\theta\right)\right) = \frac{\pi\theta}{\beta a}$.

These calculations rely only on the analytic properties of $\varepsilon(k)$ for one-dimensional periodic potentials and on the existence of a gap between the lowest band and higher bands. We stress that while the location of the branch point in the complex momentum plane (i.e., the value of μ_0) depends on system details, its existence and the order of the branch point are independent of the specifics of the periodic potential [3, 4, 35]. Therefore, the critical exponent of 1/2 is universal for all substrate potentials that are periodic along the x direction and constant along the τ direction. The details of the calculation linking the branch point structure to the polymer conformations can be found in Appendix A.6.2 along with figures of the complex band-structure for a cosine potential and a calculation of the tilt for arbitrary filling (see Eq. (A.15) in Appendix A.6.2).

In summary, we have established that for a commensurate system, the polymer tilt angle is determined by the complex-valued lowest energy band and behaves as

$$\phi = \frac{\beta a}{\pi} \operatorname{Im}\left(\varepsilon_0\left(\frac{\pi}{a} + i\beta F\theta\right)\right) = \begin{cases} 0 & \text{if } \theta < \theta_{\rm c}, \\ c(\theta - \theta_{\rm c})^{\frac{1}{2}} & \text{if } \theta \gtrsim \theta_{\rm c}, \\ \theta & \text{if } \theta \gg \theta_{\rm c}, \end{cases} \tag{2.29}$$

for some constant of proportionality, c, which depends on the specifics of the periodic potential. Fig. 2.5 shows this theoretical prediction, numerically computed from the complex band structure of a cosine potential as used in our simulations (solid line). The tilt exhibits the expected functional forms near the critical point (dotted line) and at large force angles (dashed line).

In the simulations performed for this paper, the polymer chains had a length of $40a$ while the horizontal length of the simulation box was $10a$, too limited to extract a critical exponent from the tilt angle measurements. We leave a numerical verification of the predicted divergence exponent for future work.

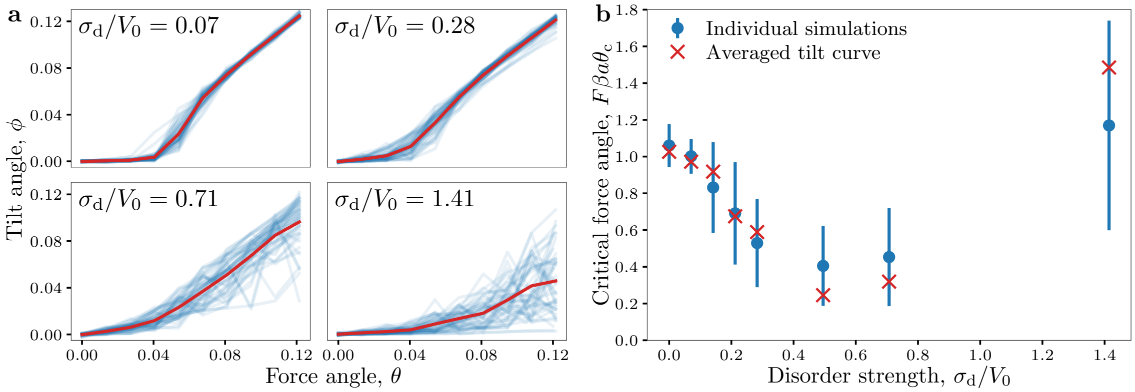

Figure 2.6. **a**, Tilt vs. force angle measurements from simulations with different disorder strengths ($V_0 = 0.239$, $F = 20$, $\beta = 1$, $N = 10$). Each panel shows curves from 50 independent random realizations of potentials (thin blue curves). The thick curve shows the average of all tilt values for each applied force angle. All panels have the same value ranges for the θ and ϕ axes. **b**, Dependence of the critical force angle on disorder strength. Discs with error bars show the average and standard deviation of θ_c measured from the 50 independent disorder realizations at each value of σ_d. Crosses show θ_c measured from the average tilt [thick curves in panel **a**].

2.4 EFFECTS OF QUENCHED SUBSTRATE DISORDER

The present model of fluctuating lines under shear was originally introduced to study the competition between non-Hermitian delocalization and *Anderson* localization [15] of the polymers due to disorder in the substrate potential. We now investigate the interplay of our band-insulator localization mechanism with Anderson localization by introducing a random component to the substrate potential $V(x)$ which is constant along the τ direction (see Appendix A.1 for implementation details). The disorder strength was quantified using the root mean square amplitude σ_d of the random potential $V_d(x)$ added to the periodic substrate, $\sigma_d \equiv \sqrt{\int_0^{Ma} dx\, [V_d(x)]^2 / Ma}$. At each disorder strength, multiple independent realizations of the random disorder potential were simulated; the results are shown in Fig. 2.6. While outcomes varied among independent runs for a given disorder strength because of the finite system size [blue curves in Fig. 2.6**a**], we find that the mean critical force varies nonmonotonically with disorder strength, first falling and then increasing (Fig. 2.6**b**). A similar trend was obeyed by critical force angles extracted from the averaged ϕ–θ curve obtained by averaging the measured tilt angles across all independent realizations (red curves and symbols in Fig. 2.6).

These observations can be explained by considering the separate effects of disorder on the bandgap and on the localization properties of the single-particle eigenstates. Numerical studies of the lattice Hatano-Nelson model with a periodic potential [77] have shown that small amounts of disorder reduced the real-valued energy gap between bands along the $\mathrm{Re}(\varepsilon)$ axis without affecting the extended nature of the Bloch eigenstates near the band edges. As a result, we expect low levels of disorder to shift the delocalization transition to smaller shear values due to the reduction of the bandgap. For a given shear value, however, all single-particle eigenstates become localized at high-enough disorder due to Anderson localization, and the many-body fermionic ground state would also be localized even in the absence of an energy gap between unoccupied and occupied states [106]. Higher values of tilt are necessary to drive the non-Hermitian delocalization of the single-particle eigenstates at large disorder, leading to an increase in the threshold shear value. The non-monotonic behavior is consistent with a switch in the dominant localization mechanism, from band-insulator physics at low disorder to Anderson localization of single-particle eigenstates at high disorder.

The non-monotonic variation in localization with disorder strength implies that for some values of the force angle, the system undergoes two transitions as the disorder is increased. Consider a commensurate system with a force angle maintained at a value for which the polymers are localized in the absence of disorder. The system can be driven into a delocalized state by increasing the substrate disorder beyond the disorder-driven gap closure. If the disorder level is increased even further, then the polymers will eventually recover their vertical confinement due to Anderson localization of the single-particle eigenstates. This mechanism represents a non-Hermitian version of a reentrant localization transition, reminiscent of similar phenomena in Hermitian systems [107, 108, 109] and in biased Brownian motion under periodic potentials with weak disorder [110].

2.5 Relation to topologically quantized transport

Since the force angle θ is shared among all polymers in the system, the transverse component of the tension can be eliminated by rotating the coordinate system so that the τ axis aligns with the tension direction. In this rotated frame, the potential energy grooves are no longer aligned with τ, giving rise to a substrate potential which depends on both x and τ, and the corresponding quantum system becomes time-dependent. That is, the energy functional in the rotated frame is

$$E = \sum_{n=1}^{N} \int_0^L d\tau \left(\frac{F}{2} (\partial_\tau x_n)^2 + V(x_n + \theta\tau) \right), \tag{2.30}$$

with the interaction terms omitted since they can be absorbed into the fermionic statistics. Prior work on a shear-free version of the directed polymer model with substrate potentials varying in both axes uncovered topological phenomena enabled by thermal fluctuations and noncrossing interactions [84]. In this section, we outline the possibility and the potential complications in realizing topologically protected chain conformations enabled by non-Hermitian spacetime-periodic potentials.

Upon performing the classical-quantum mapping as before, the quantum Hamiltonian for each fermionic particle acquires a time-dependence in the potential,

$$\hat{H} = \frac{p^2}{2m} + V(x + igt/m). \tag{2.31}$$

and the partition function of the chain satisfies the following equation [111]:

$$\frac{\partial\Psi(x,\tau)}{\partial\tau} = \left(\frac{1}{2F\beta}\frac{\partial^2}{\partial x^2} - \beta V(x+\theta\tau)\right)\Psi(x,\tau). \tag{2.32}$$

The potential is periodic in space (with period a) and along the imaginary time axis (with period a/θ), making Eq. (2.32) a Floquet partial differential equation [112]. The equation can also be derived by changing variables from (x,τ) to $(x',\tau') = (x+\theta\tau,\tau)$ in Eq. (2.3).

At small values of θ, the Hamiltonian varies slowly in time so we can use the quantum adiabatic theorem to describe the evolution of the probability density along the vertical axis. It is known that a 1D quantum system with a potential varying slowly in time exhibits a current which is quantized to multiples of the Chern number. This is called the quantized adiabatic pump or Thouless pump [113]. In the polymer system, this mechanism translates to the tilt of the polymers at commensurate filling being proportional to the Chern number of the lowest band of the spacetime-periodic potential [84], which equates to one for a sliding potential of the form $V(x,\tau) = V(x+\theta\tau)$ [113]. Each polymer contour, on average, shifts to the right by one lattice step for each period in the τ direction, which corresponds to the the polymer profiles being tilted by an angle θ away from the vertical direction and following the potential grooves exactly. This topological tilt matches the commensurate conformations observed at low force angles in simulations.

In the rotated frame, the delocalization transition is triggered by increasing the tilt of the grooves relative to the vertical (tension) direction beyond a threshold angle. Past the transition, chains do not follow the grooves but instead align themselves closer to the vertical direction. The Chern number of the substrate potential no longer dictates the alignment of the polymers, and the transition can be interpreted as a non-Hermitian breakdown of the topological adiabatic pump.

We have not achieved a quantitative understanding of this delocalization transition in the rotated frame, where no gap closure is apparent. The instantaneous spectrum of the time-dependent Hamiltonian in the rotated frame,

$$\left(\frac{1}{2F\beta}\frac{\partial^2}{\partial x^2} - \beta V(x+\theta\tau)\right)\Psi(x,\tau) = \varepsilon(\tau)\Psi(x,\tau), \tag{2.33}$$

can be found by replacing $x + \theta\tau \rightarrow x'$. This gives us

$$\left(\frac{1}{2F\beta}\frac{\partial^2}{\partial x'^2} - \beta V(x')\right)\Psi(x'-\theta\tau,\tau) = \varepsilon(\tau)\Psi(x'-\theta\tau,\tau), \tag{2.34}$$

so that $\Psi(x'-\theta\tau,\tau)$ is a Bloch state $e^{ik(x'-\theta\tau)}u_k(x'-\theta\tau)$ for the Hermitian Hamiltonian $\frac{1}{2F\beta}\frac{\partial^2}{\partial x'^2} - \beta V(x')$ and $\varepsilon(\tau)$ is the corresponding real-valued energy with no dependence on θ or τ. In other words, the instantaneous spectrum of the time-dependent Hamiltonian in the rotated frame, Eq. (2.31), does not exhibit a gap closure at any value of g so an alternative mechanism for an abrupt transition at a threshold force angle is needed. One possible mechanism is a breakdown in adiabaticity due to mixing with the higher bands when the potential varies so quickly in the vertical direction that ground-state dominance no longer applies. In this limit, we must consider the Floquet spectrum of the Hamiltonian, which describes the evolution of eigenstates over full periods in the vertical direction [114]. The breakdown of adiabaticity and corresponding delocalization could be triggered by the appearance of a Floquet exceptional point [115] at a threshold force angle.

2.6 Discussion

In summary, we have described a new non-Hermitian delocalization transition in a statistical mechanical system of polymer chains. The transition occurs from an insulator-like localized state created via a periodic potential and noncrossing interactions, and is driven by transverse forces that generate non-Hermitian terms under a mapping to a solvable quantum Hamiltonian. We found that the delocalization of the polymer chains is caused by a gap closure in the complex non-Hermitian band structure. We derived the exact value of the critical shear in terms of the branch point structure of complex energy bands of the Hamiltonian. We also found that the critical exponent by which the shear modulus diverges is given by generic properties of the branch point. We have investigated the localization due to the combined effect of both periodicity and disorder and uncovered preliminary evidence that while disorder favours localization at high values, it encourages *de*localization at lower values. Finally, we mapped the system to a 1D non-Hermitian Thouless pump, whose breakdown triggers the delocalization transition.

Our work shows that non-Hermitian band physics [57] and phase transitions driven by exceptional points [116], both typically associated with driven systems, can be realized in a purely classical equilibrium setting. The directed polymer model studied here serves as a test-bed for exploring non-Hermitian physics that is straightforward to describe and visualize, and which admits exact solutions even in the presence of thermal fluctuations and interactions. Our model and analytical framework be generalized to more complex potentials [117, 118] and interactions [119], as well as disorder models that could harbor new many-body localization phenomena [120]. The gauge transformation that links the spectrum of our system to the analytic continuation of band structures to complex-valued crystal momenta [3, 35] could provide insights into non-Hermitian delocalization in systems where localization is caused by disorder or interactions. Higher-dimensional generalizations of our system, which generate particles with exotic statistics under the classical-quantum mapping [121], could be used to probe the non-Hermitian physics of composite fermions.

A promising avenue for further investigation involves analyzing the system in a rotated frame which aligns the τ axis with the net force direction rather than the potential grooves. In this frame, the corresponding quantum system becomes time-dependent, opening up the possibility of realizing non-Hermitian topological phenomena [55, 57] due to adiabatic pumping of the underlying probability distributions [84, 111]. Delocalization in the rotated frame could provide a manifestation of Floquet exceptional point physics [115] in a classical model. The introduction of disorder, which enables unique non-Hermitian topological indices based on winding numbers [122, 123], provides yet another target for future studies.

While we have focused on the theoretical description of a model polymer system in our work, the transition we have uncovered could potentially be realized in a variety of fluctuating-line systems. The 1+1D statistical mechanics of vortex lines has previously been measured in type-II superconductors in a slab geometry [82]. The substrate potential for the vortices can be controlled by patterning the superconducting properties via techniques such as focused ion beam milling [124] or masked ion irradiation [125]. In this system, the localized state at nonzero tilt angle signifies a misalignment between the external magnetic field direction (the direction of applied tension) and the direction of the internal magnetization (carried by the vortices, which are aligned to the potential grooves)—a transverse Meissner effect [69], owed to band insulator physics rather than disorder. Other experimental candidates include artificial polymer-like fluctuating chains assembled from mesoscopic monomers such as colloids [126, 127] and nanoparticles [128], which can be confined to planar substrates and subjected to patterned electromagnetic or chemical forces.

CHAPTER III

SPACE-TIME SYMMETRY AND NON-RECIPROCAL PARAMETRIC RESONANCE IN MECHANICAL SYSTEMS

This work was published in Physical Review E as Ref. [129]. Compared to the journal text there are a few changes in this version.

3.1 Introduction

Parametric resonance—the injection of energy into an oscillator through periodic time-modulation of a system parameter—is a fundamental physical mechanism that compromises the stability of mechanical structures [28, 39] but can also be exploited to amplify electrical [130, 131] and mechanical [132, 133, 134] signals. When combined with nonlinear oscillator dynamics, parametric resonance underpins the working principles of classical time crystals [135, 136], coherent Ising machines [137, 138, 139], quantum microwave amplifiers [140], and other mechanical and NEMS-based devices [141, 142, 143]. Engineering parametric resonances by patterning system parameters in space and time pave a route towards active metamaterials with tunable signal processing capabilities [36, 144].

For a single oscillator, the existence of parametric resonances is governed by Hill's equation [145] (the Mathieu equation being a special case [146, 147]), which predicts resonances at modulation time-periods that are near integer multiples of half the oscillator's natural time period [28, 148]. In contrast, the resonance conditions for arbitrary systems of coupled parametric oscillators are sensitive to the modulation phases on individual oscillators [149, 150, 151]. Resonances are typically revealed only after a numerical or perturbative calculation of the Floquet matrix (the time-evolution operator over one modulation period).

Here, we derive the resonance conditions of coupled parametric oscillators by harnessing recent advances in the symmetry analysis [21] and topological classification [24, 56, 152] of non-Hermitian quantum systems. In doing so, we extend previous work on the topological classification of static mechanical systems via classical-quantum mapping [17, 18, 21] to time-dependent systems by using non-Hermitian and Floquet techniques. Specifically, we establish parametric resonance as an example of a real-to-complex eigenvalue transition or pseudo-Hermiticity breaking [29, 153] in the Floquet matrix. Our resonance conditions are formulated in terms of the symmetries obeyed by the time-modulated system and thus do not rely on specific functional forms of the parametric modulation. Furthermore, we demonstrate that the static limit of the Floquet matrix, which can be evaluated exactly from the unmodulated system, is sufficient to reveal these conditions.

Upon including external symmetries, the space of potential outcomes for parametric resonance is significantly enriched. The effect of static external symmetries (such as discrete translation symmetry) is straightforward—vector spaces associated with different symmetry eigenvalues decouple, thereby further constraining the spectra and their topological classification [17, 18]. However, time-modulated systems can admit space-time symmetries [154] in which the system remains invariant after combined discrete translations in space and time. For such a symmetry, the time-dependent Hamiltonian no longer splits into decoupled blocks. Instead, we identify a general framework in terms of an operator combining spatial translation with time evolution, that captures more information about the system dynamics than the Floquet matrix does, to analyze the dynamics of space-time symmetric systems.

We demonstrate the utility of this operator, which we term the *space-time Floquet matrix*, by applying it to a ring of coupled parametric oscillators satisfying space-time

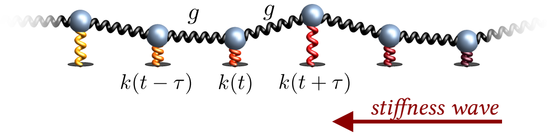

Figure 3.1. A system of n oscillators (shown with random displacements) of unit mass connected to their nearest neighbours via springs of stiffness g (black springs) and to the ground with a spring of stiffness $k_j(t) = k[1+\delta f(t+j\tau)]$ (colored springs). Here, j indexes the oscillators, k is the grounding stiffness in the absence of time-modulation, δ sets the modulation strength, $f(t)$ is a T-periodic function, and τ is the modulation offset between nearest neighbours. We assume periodic boundary conditions in the system. When $\tau = \frac{T}{n}$, the system enjoys space-time symmetry, i.e., it is invariant after a translation by one position in the leftwards direction followed by a time evolution of τ time units. Equivalently, a stiffness wave travels in the direction of decreasing j (from dark red to yellow).

symmetry (Fig. 3.1). We show that several normal modes of the unmodulated ring are protected by symmetry from resonating at frequencies where parametric modulation would naively be expected to occur. For example, the lowest-frequency or ground-state mode of the unmodulated system has frequency ω, the natural frequency of the individual oscillators. Yet, the smallest time-period of modulation at which the ground-state normal mode becomes resonant is $T = n\pi/\omega$ (rather than the resonance period $T = \pi/\omega$ of each oscillator), where n is the number of oscillators in the ring. For a large system, the ground state is effectively protected from parametric resonance in a space-time modulated system.

The space-time Floquet matrix also determines the conditions for amplification of one-way propagating modes. In the ring of oscillators, wavelike modes occur in degenerate pairs which travel in opposite directions. We show that the traveling-wave parameter modulation amplifies these counterpropagating modes at different frequencies, thereby breaking left-right symmetry. The conditions for this selective one-way amplification are obtained exactly from the symmetries alone, independently of the functional form of the time-modulation. These conditions provide a simple way to engineer nonreciprocal transport [38] and one-way amplification [151, 155] in non-Hermitian Floquet systems.

Our results provide a theoretical framework, based on non-Hermitian and Floquet symmetries, to design collective mechanical states with interesting resonance and transport properties. Potential applications include sensing [156, 157, 158], active signal processing [36, 134, 142, 143, 144, 159], and computing [137, 138]. In addition, the space-time Floquet matrix provides an exact framework for analyzing all systems with space-time symmetry [40, 155, 160], beyond the mechanical systems that are the focus of this work.

This paper is structured as follows. In **Section 3.2** we analyze the internal symmetries of linear classical mechanical systems. We begin by developing a framework for static systems in **Section 3.2.1** which we then generalize to time-dependent systems in **Section 3.2.2**, identifying the conditions for parametric resonance. The effects of external symmetries are analyzed in **Section 3.3**, specifically translational symmetry (**Section 3.3.1**) and space-time symmetry (**Section 3.3.2** and **Section 3.3.3**). We discuss the significance of our results and possible future directions in **Section 3.4**.

3.2 NON-HERMITIAN FLOQUET THEORY OF PARAMETRIC OSCILLATORS

We describe the stability and mode structure of coupled parametric oscillators aided by the symmetries and topological structures that have been identified in non-Hermitian and Floquet quantum systems [24, 56, 152]. Since these techniques apply to systems that are first-order in time, we use a Hamiltonian formulation of the dynamics of coupled oscillators, which we first describe for oscillators with static parameters before generalizing to the time-dependent case. Different variants of the time-independent formulation below have appeared in Refs. [18, 29, 161].

3.2.1 Time-independent case

Consider n coupled classical mechanical oscillators of equal masses (set to 1). Denote the positions of the oscillators by $\boldsymbol{x} = \{x_1, x_2, \ldots, x_n\}^T$ such that the potential energy of the system is $\boldsymbol{x}^T \cdot K \cdot \boldsymbol{x}$ where K is the stiffness matrix (a.k.a. the dynamical matrix). The stiffness matrix is real and symmetric, with real eigenvalues Ω_i^2 and corresponding eigenvectors (normal modes) $\boldsymbol{q}_i$ satisfying

$$K\boldsymbol{q}_i = \Omega_i^2 \boldsymbol{q}_i. \tag{3.1}$$

In the absence of dissipation or velocity-dependent forces, the equation of motion of the oscillators is

$$i\frac{d}{dt}\begin{pmatrix} \boldsymbol{x}(t) \\ \boldsymbol{p}(t) \end{pmatrix} = -i\begin{pmatrix} 0 & -\mathbb{I}_n \\ K & 0 \end{pmatrix}\begin{pmatrix} \boldsymbol{x}(t) \\ \boldsymbol{p}(t) \end{pmatrix} \tag{3.2}$$

where $\boldsymbol{p} = \{p_1, p_2, \ldots, p_n\}^T$ denotes the momenta of the oscillators. While we disregard friction and velocity-dependent forces such as the Lorentz force or gyroscopic forces here, in Appendix B.1 we show that the results below generalize as long as the friction is uniform for all oscillators and the velocity-dependent forces have no explicit time dependence.

Eq. (3.2) defines the quantum Hamiltonian

$$H = -i\begin{pmatrix} 0 & -\mathbb{I}_n \\ K & 0 \end{pmatrix} \tag{3.3}$$

in terms of the classical stiffness matrix. When the Hamiltonian is time-independent the equation can be solved by substituting $\begin{pmatrix} \boldsymbol{x}(t) \\ \boldsymbol{p}(t) \end{pmatrix} = e^{-i\omega t}|v\rangle$, where $|v\rangle$ is a time-independent column-vector, to get

$$\omega|v\rangle = H|v\rangle, \tag{3.4}$$

an eigenvalue equation. The eigenvectors are

$$|v_i^{\pm}\rangle = \begin{pmatrix} \boldsymbol{q}_i \\ -i\omega_i^{\pm}\boldsymbol{q}_i \end{pmatrix} \tag{3.5}$$

with eigenvalues

$$\omega_i^{\pm} = \pm\Omega_i. \tag{3.6}$$

The partners $|v_i^+\rangle$ and $|v_i^-\rangle$ are associated with the same normal mode $\boldsymbol{q_i}$ but differ in the phase relationship between position and velocity.

The Hamiltonian H, generically, has two internal symmetries. First, since classical mechanics is real-valued, by our choice of notation we have $H^* = -H$ such that its eigenvalues are either purely imaginary or come in pairs with oppositely signed real parts. Second, H is pseudo-Hermitian, $GHG^{-1} = H^\dagger$, where

$$G = iJ = i\begin{pmatrix} 0 & \mathbb{I}_n \\ -\mathbb{I}_n & 0 \end{pmatrix} \tag{3.7}$$

is the intertwining operator which is Hermitian as well as unitary. This pseudo-Hermiticity (a generalization of $\mathcal{PT}$ symmetry [162]) arises from the symplectic structure of Hamilton's equations of motion [29] (J is the symplectic form). Pseudo-Hermiticity implies that the eigenvalues of H are either real or come in complex-conjugate pairs.

Taking the two symmetries together, H must either have pairs of oppositely signed eigenvalues which are purely real or purely imaginary, or it must have quadruplets of eigenvalues with non-zero real as well as imaginary parts forming sets of the form,

$\{\lambda, -\lambda, \lambda^*, -\lambda^*\}$. We will show that these facts hold true even in the time-dependent case.

For the energy of the system to be non-negative, the stiffness matrix K is constrained to be positive-definite (in the absence of zero-frequency modes, also called zero modes). While this constraint does not introduce any additional non-Hermitian internal symmetries, it enforces the eigenvalues $\omega_i^{\pm} = \pm\Omega_i$ to be purely real. The Hamiltonian H can now be transformed, via a non-unitary similarity transformation, to a Hermitian matrix enabling the use of the Hermitian topological classification for conservative mechanical systems [18]. This transformation requires taking the square-root of the matrix K; possible complications due to branch-points are avoided if zero modes are excluded. In the language of the Hermitian topological classification, the two symmetries noted above are mapped to the Hermitian time-reversal symmetry and the Hermitian chiral symmetry respectively [18].

In the presence of zero modes, an alternate strategy is to use the equilibrium matrix, which links displacements to strains, in place of the dynamical matrix [12, 17]. In either case, the topological classification in terms of Hermitian matrices is not applicable to either time-dependent systems or dissipative systems where the frequency eigenvalues are not constrained to be purely real. Non-Hermitian symmetries, as used in this work, are arguably more useful since they generalize easily, as we shall see below, to such non-conservative systems [59, 161, 163]. In the GBL classification scheme of non-Hermitian Hamiltonians [56], the first internal symmetry we identified corresponds to the K symmetry: $H = \epsilon_k k H^* k^{-1}, k k^* = \eta_k \mathbb{I}$ with $\epsilon_k = -1$ and $\eta_k = +1$. The second internal symmetry corresponds to the Q symmetry: $H = \epsilon_q q H^\dagger q^{-1}, q^2 = \mathbb{I}$ with $\epsilon_q = +1$.

A real eigenvalue of a pseudo-Hermitian matrix H with intertwining operator G can be classified by its Krein signature, which is given by the sign of $\langle v|G|v\rangle$ [28, 29, 164]. Here $|v\rangle$ is the corresponding eigenvector of H and $\langle v| = |v\rangle^\dagger$ the conjugate-transpose of the eigenvector. Upon tuning some parameter in the matrix, these real eigenvalues can collide on the real axis and turn into complex-conjugate eigenvalues (a phenomenon known as pseudo-Hermiticity breaking) only if they have opposite signatures [29]. The collision typically marks a singularity in the eigenvalue spectrum called an exceptional point, at which the matrix becomes non-diagonalizable [162]. Pseudo-Hermiticity breaking is typically accompanied by drastic changes in the behavior of a physical system. Examples include the emergence of amplified/damped modes in $\mathcal{PT}$-symmetric systems [2] and unusual phase transitions driven by exceptional points [15, 42, 74, 116]. In the mechanical system under consideration, pseudo-Hermiticity breaking generates one or more frequencies with positive imaginary component, corresponding to amplified or unstable modes.

To find the Krein signature of each eigenvalue of our Hamiltonian, we compute

$$\langle v_i^\pm|G|v_i^\pm\rangle = \begin{pmatrix} \boldsymbol{q}_{\boldsymbol{i}}^* & +i\omega_i^\pm \boldsymbol{q}_{\boldsymbol{i}}^* \end{pmatrix} G \begin{pmatrix} \boldsymbol{q}_i \\ -i\omega_i^\pm \boldsymbol{q}_i \end{pmatrix} = \pm 2|\boldsymbol{q}_i|^2\Omega_i, \tag{3.8}$$

which shows that the eigenspaces corresponding to $|v_i^+\rangle$ have positive signature while those corresponding to $|v_i^-\rangle$ have negative signature. Physically, these two signatures are distinguished by whether the momenta are lagging behind or ahead of the positions (or, in the case of parametric modulation, whether they are in phase or out of phase with the modulation). In the absence of dissipation or parametric modulation, eigenvalues of different signatures can meet only at the origin, i.e. at $\omega = 0$. Indeed the zero modes (or floppy modes) govern the instability of static mechanical systems [17].

The Krein classification of eigenvalues can be performed even for a time-dependent system and will be crucial for the determination of the conditions for parametric resonance.

3.2.2 Time-dependent case via Floquet theory

We now consider the effect of modulating the system parameters—specifically, the spring stiffnesses—so that the stiffness matrix $K(t)$ is time-dependent. The equations of motion now take the form of the time-dependent Schrödinger equation,

$$i\frac{d}{dt}\begin{pmatrix}\boldsymbol{x}(t)\\ \boldsymbol{p}(t)\end{pmatrix} = -i\begin{pmatrix}0 & -\mathbb{I}_n\\ K(t) & 0\end{pmatrix}\begin{pmatrix}\boldsymbol{x}(t)\\ \boldsymbol{p}(t)\end{pmatrix} = H(t)\begin{pmatrix}\boldsymbol{x}(t)\\ \boldsymbol{p}(t)\end{pmatrix}. \tag{3.9}$$

The solution to this equation is

$$\begin{pmatrix}\boldsymbol{x}(t)\\ \boldsymbol{p}(t)\end{pmatrix} = U(t)\begin{pmatrix}\boldsymbol{x}(0)\\ \boldsymbol{p}(0)\end{pmatrix}, \tag{3.10}$$

where $\begin{pmatrix}\boldsymbol{x}(0)\\ \boldsymbol{p}(0)\end{pmatrix}$ are the initial conditions of the oscillators and the time-propagation matrix $U(t)$ satisfies

$$i\frac{d}{dt}U(t) = H(t)U(t) \tag{3.11}$$

with the initial condition $U(0) = \mathbb{I}_{2n}$.

The spectrum of the time-propagation matrix exhibits features inherited from the internal symmetries satisfied by $H(t)$. First, the condition $H^*(t) = -H(t)$ implies that the time-propagation matrix is real,

$$U^*(t) = U(t). \tag{3.12}$$

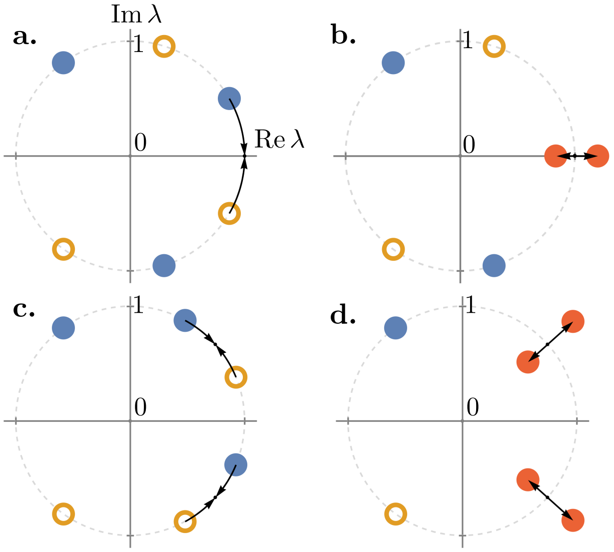

Figure 3.2. Pseudo-Hermiticity breaking in the spectrum of the time-propagation matrix $U(t)$. **a.** Representative spectrum for a system with three degrees of freedom, with all eigenvalues of $U(t)$ lying on the unit circle. These eigenvalues form pairs $\{\lambda = 1/\lambda^*, \lambda^* = 1/\lambda\}$ with positive (solid, blue) and negative (hollow, yellow) Krein signature. Upon tuning a parameter of the system, isolated eigenvalues move along the unit circle (solid arrows). **b.** When a pair of eigenvalues of opposite Krein signature collide, they can move off the unit circle (solid, red), signifying pseudo-Hermiticity breaking. They are constrained to lie on the real axis to satisfy $\{\lambda = \lambda^*, 1/\lambda = 1/\lambda^*\}$. **c.** Same as **a,** but with two pairs of eigenvalues colliding away from the real axis. **d.** After pseudo-Hermiticity breaking, the two colliding pairs move off the unit circle as a quartet of four distinct values $\{\lambda, \lambda^*, 1/\lambda, 1/\lambda^*\}$.

As a result, its eigenvalues are either purely real or they come in complex-conjugate pairs. Second, the symplecticity condition, $GH(t)G^{-1} = H^\dagger(t)$, gives [165]

$$U^{-1}(t) = G^{-1}U^\dagger(t)G. \tag{3.13}$$

This symmetry ensures that eigenvalues of $U(t)$ come in reciprocal pairs (or are either of $+1$ or -1). The two symmetries together require that the eigenvalues of $U(t)$ appear in sets of the form $\{\lambda, \lambda^*, 1/\lambda, 1/\lambda^*\}$.

Analogous to the time-independent case, we note that the matrix $M(t) := i\log[U(t)]$ satisfies the pseudo-Hermiticity condition $GM(t)G^{-1} = M^\dagger(t)$. The eigenvectors $|v_i\rangle$ of $M(t)$ are the same as that of $U(t)$ while the corresponding eigenvalue is $i\log(\lambda_i)$ which is real if λ_i lies on the unit circle of the complex plane. Thus, each eigenvalue λ_i of $U(t)$ which lies on the unit circle can be assigned a Krein signature according to the sign of $\langle v_i|G|v_i\rangle$ where $|v_i\rangle$ is the corresponding eigenvector of $U(t)$. Upon smoothly varying any parameter that affects $U(t)$ (such as any spring stiffness in the stiffness matrix or the time variable itself), isolated eigenvalues of $U(t)$ on the unit circle cannot move off it unless two eigenvalues of opposite Krein signature collide [28]. The collision signifies pseudo-Hermiticity breaking in $M(t)$ which we equivalently refer to as pseudo-Hermiticity breaking in $U(t)$. Two examples of such pseudo-Hermiticity breaking transitions are shown schematically in Fig. 3.2**a–b** and Fig. 3.2**c–d**.

We now restrict the parametric modulation to be periodic in time with time period T, so that $K(t+T) = K(t)$. By Floquet's theorem, the behavior of the system at time scales much longer than the modulation period is determined by the eigenvalues (also called *Floquet multipliers*) $\lambda_i(T)$ of the *Floquet matrix* $U(T)$ (see Appendix B.2 for details on Floquet methods). In particular, when a system is initialized with the ith eigenvector $|v_i\rangle$ of $U(T)$ (called a *Floquet eigenvector*) at $t = 0$, its state at integer multiples of the time period is $\begin{pmatrix} \boldsymbol{x}(mT) \\ \boldsymbol{p}(mT) \end{pmatrix} = U^m(T)|v_i\rangle = \lambda_i^m|v_i\rangle$. Eigenvalues of $U(T)$ that lie off the unit circle correspond to modes that grow or decay exponentially with time and indicate parametric resonances.

The pseudo-Hermiticity breaking structure sketched in Fig. 3.2 can be used to identify conditions for the existence of parametric resonances when the strength of the parametric modulation is small, i.e., when $K(t) = K_0 + \delta K_1(t)$ with $K_1(t+T) = K_1(t)$ and $\delta \ll 1$. In the limiting case, the eigenvalues of $U(t;\delta \to 0) \sim e^{-iHt}$ are $e^{\mp i\Omega_i t}$ where $\pm\Omega_i$ are precisely the eigenvalues of the time-independent Hamiltonian in Eq. (3.3), with Krein signatures identified in Eq. (3.8). As time advances, the eigenvalues of $U(t)$ with positive (negative) Krein signature move clockwise (counter-clockwise) along the unit circle (see Fig. 3.3**b** for an example involving a system with two degrees of freedom). Eigenvalues of opposite Krein signature coincide when $e^{-i\Omega_i t} = e^{+i\Omega_j t}$ for some i and j (the case of $i = j$ included), which occurs when

$$t = r\frac{2\pi}{\Omega_i + \Omega_j} \tag{3.14}$$

where r (here and throughout the paper) denotes an arbitrary positive integer. Since such collisions are the precursor to the eigenvalues moving off the unit circle, they are termed unstable degeneracies.

When parametric modulation is turned on ($\delta > 0$) the eigenvalues of $U(t;\delta)$ are approximately equal to those of $U(t;\delta \to 0)$ by continuity [1]. Generically (in the absence of additional symmetries inhibiting them), they move off the unit circle at values of time near the unstable degeneracies, Eq. (3.14). If the system is parametrically modulated with such time-periods, these eigenvalues moving off the unit circle would precisely be the Floquet multipliers. Thus parametric resonance is expected whenever the modulation time-period T satisfies Eq. (3.14) for small modulation strengths. As the modulation strength increases, resonances will be present for a range of modulation time-periods around $r\frac{2\pi}{\Omega_i+\Omega_j}$ that grows with δ [28]. As Fig. 3.2**b** and **d** illustrate, parametric resonances occur in pairs with one Floquet multiplier moving outward from the unit circle signaling amplification ($|\lambda(T)| > 1$) whereas its partner moves inward signaling damping ($|\lambda(T)| < 1$).

The collision of eigenvalues associated with partners of the same normal mode, eg. $e^{-i\Omega_i t} \to e^{+i\Omega_i t}$, occurs on the real axis at values of time $t \sim r\frac{\pi}{\Omega_i}$. At even values of r, the eigenvalues meet at $+1$ (Fig. 3.2**a**), and the frequencies of the nascent

---

[1] Continuity of $U(t;\delta)$ as a function of δ is a consequence of the continuity of $H(t;\delta)$ as a function of δ (see Section II.1.3 of Ref. [28])

amplified/damped modes are locked to the modulation frequency (see Appendix B.2). At odd values of r, the collision happens at a value of -1, and the frequency of the modes is locked to double the modulation frequency. These two cases typically lead to tangent (saddle-node) bifurcations and period-doubling bifurcations, respectively, when nonlinearity is added to the system [166]. If the eigenvalues associated with different normal modes meet, the collision of a pair of eigenvalues ($e^{-i\Omega_i t} \rightarrow e^{+i\Omega_j t}$ for example) is accompanied by a collision of the complex-conjugate eigenvalues, i.e., $e^{+i\Omega_i t} \rightarrow e^{-i\Omega_j t}$ (as shown schematically in Fig. 3.2**c**). We note that for a single oscillator with natural frequency Ω, the resonance condition from Hill's equation of $T = r\pi/\Omega$ is recovered.

Since parametric resonance corresponds to pseudo-Hermiticity breaking in $U(T)$, many techniques and phenomena in the theory of pseudo-Hermitian matrices carry over to the mechanical system under study. For example, stable phases (regions in a parameter space where all eigenvalues lie on the unit circle) of the Floquet matrix can be characterized topologically by the ordering of eigenvalues of positive and negative signature along the unit circle (compare Fig. 3.2**a** to Fig. 3.2**c**). It is impossible to traverse from one stable phase to a stable phase with a different ordering of eigenvalues without encountering an unstable degeneracy [29]. Such topological phases may be harnessed for topologically protected behavior and the preparation of novel dynamical phases with no static analogs [167, 168]. Additionally, the boundaries, in parameter space, separating a stable phase from an amplified phase form lines or surfaces of exceptional points where eigenvectors of the Floquet matrix coalesce [29]. These symmetry-protected exceptional points may be useful in the design of mechanical sensors [169] or in realizing topologically protected transport [170] and mode switching [22].

3.3 EFFECT OF EXTERNAL SYMMETRIES

In the previous section, we linked the existence of parametric resonances to the formation of degeneracies in the Floquet matrix in the limit of vanishing parameter modulation. This led to the resonance condition of Eq. (3.14) which is necessary, but not sufficient, for resonance to occur. While a generic stiffness modulation with time period T satisfying Eq. (3.14) is expected to lead to a resonance, the functional form of the time-modulation could be fine-tuned for a particular system to avoid resonances with any of its modes. We expect these cases to occupy isolated points in the space of possible modulation functions, whose existence would be revealed by numerical evaluation of the Floquet exponents or by higher-order perturbation theory. However, if we can identify external symmetries that prevent resonances from occurring, then we can rule out resonances for *any* modulation that satisfies these external symmetries, without relying on fine-tuning. The effect of external spatial and space-time symmetries on the parametric resonances of time-modulated features is addressed in this section. While we focus on a model system of a ring of parametrically modulated oscillators for concreteness, the observations we make apply generally to time-modulated systems that satisfy spatial and space-time symmetries.

Consider the ring of oscillators in Fig. 3.1. They are confined to oscillate in the vertical direction through the action of grounding springs of stiffness $k_j(t) = k[1 + \delta f(t + j\tau)]$ and connected to their nearest neighbours via springs of zero rest length and static stiffness g [2]. Here, $f(t)$ is an arbitary periodic function with period T and unit amplitude, and $0 \leq \tau < T$ quantifies the phase-shift in the modulation as

---

[2] The choice of zero rest length ensures that the spring applies a vertical restoring force of magnitude $g\Delta x$ when its ends have a relative displacement of Δx. Alternatively, springs under uniform tension ga, where a is the separation of the two oscillators, also give rise to vertical restoring forces of the same magnitude.

we move from one oscillator to the next. Our chosen modulation sets up a stiffness wave which travels from the jth oscillator to the $(j-1)$th oscillator over time (a direction we shall refer to as leftwards).

In the static limit $\delta \to 0$, this ring of oscillators has discrete translational symmetry. The normal mode frequencies of the unmodulated system are $\pm\Omega(\kappa_1), \ldots, \pm\Omega(\kappa_n)$ where κ_j is the jth Bloch wavevector set by the system size and the periodic boundary conditions. According to the discussion in **Section 3.2.2**, upon turning on the parametric modulation we generically expect parametric resonance whenever the time-period of modulation T is tuned to $T = r\frac{2\pi}{\Omega(\kappa_i)+\Omega(\kappa_j)}$ for some pair of normal mode frequencies. We will consider two different kinds of symmetries and how they influence these conditions for parametric resonance.

3.3.1 Discrete spatial symmetry in a modulated system ($\tau = 0$)

When the system is modulated at $\tau = 0$, each oscillator undergoes the same modulation and the system retains translational symmetry at every point in time. We can still apply Bloch's theorem to block-diagonalize the time-dependent Hamiltonian. The Floquet multipliers associated with the blocks corresponding to different Bloch wave-vectors decouple from each other. As a result, parametric resonance only occurs at time periods equal to $T = r\frac{\pi}{\Omega(\kappa_i)}$, but not at $T = r\frac{2\pi}{\Omega(\kappa_i)+\Omega(\kappa_j)}$ with $i \neq j$. At finite modulation amplitudes, the resonances open up a range of wave-vectors in the vicinity of the resonant κ_i for which the corresponding Bloch waves become unstable [134, 155].

In fact, this decoupling due to symmetry is a general phenomenon [29, 171]. Let g_i be the elements of the group representation corresponding to a symmetry present in the system. Then $H(t)$ commutes with g_i at all times t and they share a common eigenbasis. Now, for typical spatial symmetries (viz. rotation, translation, inversion, etc.) the elements g_i take the form $\begin{pmatrix} A & 0 \\ 0 & A \end{pmatrix}$ where A is some invertible square matrix (i.e., the matrices g_i act on the positions and momenta in an equivalent manner). Any matrix of such form embodies a canonical transformation and hence commutes with the intertwining operator G. Thus, $H(t)$ and G can be block-diagonalized in the eigenbasis of the elements of the group representation. The system is then reduced to a set of uncoupled block matrices, each of which inherit the symmetries discussed in **Section 3.2.2**.

3.3.2 Space-time symmetry in a modulated system ($\tau = T/n$)

When the modulation at each oscillator is shifted in time by $\tau = \frac{T}{n}$ with respect to the oscillator on its left, the system enjoys space-time symmetry [40, 41, 154]. That is, the system is invariant after a translation by one position in the leftwards direction followed by a time evolution of τ time units. Explicitly, the Hamiltonian satisfies

$$H(t) = SH(t + T/n)S^{-1}, \tag{3.15}$$

where S is the matrix operator which cyclically shifts each oscillator's coordinates by one position in the direction of the stiffness wave, i.e., to the left (see Appendix B.3).

For such symmetries, there is no way to block-diagonalize the time-dependent Hamiltonian. Nevertheless, we shall see that the system is still protected from parametric resonance at certain frequencies. Eq. (3.15) implies that the time-propagation matrix satisfies (see Appendix B.3)

$$U(t + T/n) = S^{-1}U(t)SU(T/n), \tag{3.16}$$

which can be considered a generalization of Floquet's theorem (Floquet's theorem is recovered when $S = \mathbb{I}_{2n}$). In particular, we have (using the fact that $S^n = \mathbb{I}_{2n}$)

$$U(T) = S^{-n}[SU(T/n)]^n = [SU(T/n)]^n. \tag{3.17}$$

The matrix $X_n := SU(T/n)$, which we term the space-time Floquet matrix, enjoys the same internal symmetries discussed in **Section 3.2.2**, i.e., it is real and satisfies $X_n^{-1} = G^{-1}X_n^\dagger G$. (The latter equation relies on the fact that S commutes with G by the arguments in **Section 3.3.1**.) As Eq. (3.17) shows, the Floquet matrix can be recovered from the space-time Floquet matrix. We shall see below that the space-time Floquet matrix X_n provides more information about the system dynamics, such as protected degeneracies and one-way amplification conditions, than the Floquet matrix $U(T)$ does.

3.3.21 Protected degeneracies and avoided resonances. It is possible for the Floquet matrix to have unstable degeneracies (where eigenvalues of opposite Krein signature collide) that do not arise in the space-time Floquet matrix X_n. Crucially, such a degeneracy in the Floquet matrix cannot develop into a parametric resonance (where Floquet multipliers move off the unit circle), as it would imply an instability in $X_n = [U(T)]^{1/n}$ without a corresponding degeneracy. To see this explicitly, consider the eigenvalues $\mu(T/n)$ of the space-time Floquet matrix in the limit $\delta \to 0$ when $X_n = SU(T/n) \sim Se^{-iHT/n}$. These eigenvalues are $e^{i\kappa_j}e^{\mp i\Omega(\kappa_j)T/n}$ and parametric resonance occurs when

$$e^{i\kappa_j}e^{+i\Omega(\kappa_j)T/n} = e^{i\kappa_k}e^{-i\Omega(\kappa_k)T/n} \tag{3.18}$$

for some Bloch wave-vectors indexed by j and k. These conditions are more restrictive than the general condition, Eq. (3.14), which only considered internal symmetries.

For instance, consider the typical method of parametrically amplifying a mode indexed by κ_i by modulating the system at $2\Omega(\kappa_i)$, i.e. modulation time period set to $T = \pi/\Omega(\kappa_i)$ which satisfies Eq. (3.14) with $r = 1$. As we saw in **Section 3.2.2**, the underlying mechanism is the collision of eigenvalues of $U(T)$ associated with the two partners of the ith normal mode of the unmodulated system. However, for the space-time symmetric modulation, the collision of eigenvalues of X_n is dictated by Eq. (3.18), which singles out

$$T = r\frac{\pi n}{\Omega(\kappa_i)}$$

corresponding to modulation frequencies tuned to $\frac{2\Omega(\kappa_i)}{n}, \frac{2\Omega(\kappa_i)}{2n}, \ldots$. When the system size is large ($n \gg 1$), any possible instabilities due to the collision of two partners of the same normal mode will be protected from amplification. This is because the first possible resonance occurs at modulation frequency tuned to $\frac{2\Omega(\kappa_j)}{n}$, and amplification at a such higher order resonance is generically much weaker [172].

As a concrete example, consider the case of $n = 2$ oscillators in Fig. 3.3 modulated in a space-time symmetric manner, which corresponds to a modulation phase difference of π. Its two normal modes are the bonding mode where the two masses move in tandem ($\omega_1 = \sqrt{k}$) and the anti-bonding mode where they move opposite to each other ($\omega_2 = \sqrt{k + 2g}$) as illustrated in Fig. 3.3**a**. In the $\delta \to 0$ limit, the spectrum of $U(t)$ exhibits unstable degeneracies at $t = r\frac{\pi}{\omega_1}$, $t = r\frac{\pi}{\omega_2}$, and $t = r\frac{2\pi}{\omega_1+\omega_2}$ (red dots in Fig. 3.3**b** show the degeneracies when $r = 1$), suggesting that the anti-bonding mode (for example) should resonate at modulation time-periods of $T = r\frac{\pi}{\omega_2}$. However, the degeneracies in $SU(t/2)$ (Fig. 3.3**c**) occur at $t = 2r\frac{\pi}{\omega_1}$, $t = 2r\frac{\pi}{\omega_2}$, and $t = (2r-1)\frac{2\pi}{\omega_1+\omega_2}$ and thus the correct resonance condition for the anti-bonding mode is modulation at $T = r\frac{2\pi}{\omega_2}$. Similarly, resonance due to the bonding mode coupling with the anti-bonding mode occurs at modulation time-periods $T = (2r-1)\frac{2\pi}{\omega_1+\omega_2}$ in contrast to the prediction of $T = r\frac{2\pi}{\omega_1+\omega_2}$ from the Floquet matrix degeneracies. When the system is modulated at frequencies where parametric resonance is forbidden by the space-time symmetry, the Floquet matrix exhibits diabolic point degeneracies.

The above resonance conditions hold in the limit of weak modulation, $\delta \to 0$. At finite values of the modulation strength, a region of parametric resonance opens up over a finite range of modulation frequencies in the neighborhood of the resonances predicted above, similar to the "instability tongues" of the Mathieu oscillator [147]. The size of the region, and the strength of the resonance (i.e., the distance of the non-unitary eigenvalue of $U(T)$ from the unit circle), will depend on the specific functional form of the time-dependent modulation. These features are demonstrated in Appendix B.4, where we connect our theoretical analysis to numerically determined resonance regions for specific realizations of the time-modulation function in the $n = 2$ space-time symmetric system.

3.3.22 Amplification of one-way travelling modes.

The space-time Floquet matrix can also uncover the conditions for parametric resonance to occur selectively for modes that travel in one direction along the ring. For a fixed Bloch wave-vector $0 < \kappa_j < \pi$, the modes associated with $\Omega(\kappa_j)$ and $-\Omega(-\kappa_j)$ travel in the direction of the stiffness wave while the modes $-\Omega(\kappa_j)$ and $\Omega(-\kappa_j)$ travel in the opposite direction. (Note that $\Omega(\kappa_j) = \Omega(-\kappa_j)$ due to the $\mathcal{T}$-symmetry of the Hermitian system at $\delta \to 0$ [18].) When the pair $\Omega(\kappa_j)$ and $-\Omega(-\kappa_j)$ are coupled by the modulation, it leads to a pair of amplified and damped modes travelling in the leftwards direction whereas the rightwards travelling modes remain unamplified. Via Eq. (3.18), this coupling happens when the corresponding eigenvalues of X_n collide, which occurs at modulation time-periods equal to

$$T = n\frac{\pi(r-1)+\kappa_j}{\Omega(\kappa_j)}. \tag{3.19}$$

By contrast, the right-wards moving modes (opposite to direction of stiffness wave) amplify at

$$T = n\frac{\pi r-\kappa_j}{\Omega(\kappa_j)}. \tag{3.20}$$

Remarkably, these two time-periods are different (except for the modes at wavevector $\kappa_j = \pi/2$). Thus, equations (3.19) and (3.20) provide simple criteria, using the symmetries of a system alone, to determine the conditions for the amplification of one-way travelling modes. Furthermore, one can control which direction of signal propagation is amplified just by tuning the modulation frequency in a space-time modulated system.

As a concrete example, consider the system of three oscillators whose normal modes in the absence of modulation are illustrated in Fig. 3.4**a**. The space-time symmetric modulation generates a travelling wave in the clockwise sense when the masses are viewed from above. The ground state mode, in which all masses oscillate in phase, resonates at a modulation frequency of $2\omega_1/3$ according to the analysis of **Section 3.3.21**; the resonance at $2\omega_1$ is avoided even though it is the strongest resonance of an isolated individual oscillator. The remaining two normal modes are degenerate and correspond to travelling waves in the clockwise (mode 2) and counterclockwise (mode 3) sense. The space-time symmetric modulation breaks the degeneracy between these modes, as can be seen by following the eigenvalues of $SU(t/3)$ (Fig. 3.4**d**–**g**). At $t = 0$, each mode contributes one eigenvalue at $e^{2\pi i/3}$ and one of opposite Krein signature at $e^{-2\pi i/3}$ (Fig. 3.4**d**). As time advances, eigenvalues with different signatures travel in opposite clock senses, and the first pair of eigenvalues to collide are those from mode 3 (the mode propagating in the opposite direction as the stiffness wave) at $t = \pi/\omega_2$ (Fig. 3.4**e**). This value is obtained from Eq. (3.20) with $r = 1$ and $\kappa = -2\pi/3$. The eigenvalues corresponding to the clockwise-propagating mode 2 collide at $t = 2\pi/\omega_2$, obtained from Eq. (3.19) with $r = 1$ and $\kappa = 2\pi/3$ (Fig. 3.4**g**).

These degeneracies in the spectrum of $SU(t/3)$ dictate the parametric resonances experienced by the travelling-wave modes when the system is periodically modulated. When the modulation time-period is $T = \pi/\omega_2$ (modulation frequency twice the natural frequency of the travelling modes), only mode 3 experiences parametric resonance, contributing an amplified and a damped Floquet eigenvector. The evolution of the oscillators when initialized to the Floquet eigenvectors are numerically computed and shown in Fig. 3.4**b**. Since the eigenvalues collide at -1, the oscillatory component of these modes has a time period of twice the modulation period, which corresponds to the period of the original normal mode. Mode 2, however, resonates at a different modulation period of $T = 2\pi/\omega_2$ (modulation frequency same as the mode frequency), with the eigenvalues colliding at $+1$, such that the period of the resulting oscillations equals the original mode periods (Fig. 3.4**c**). The strength of amplification of this mode, quantified by the rate of change of the amplitude, is much weaker than that of the counterclockwise-propagating mode in Fig. 3.4**b**, since it is a higher-order resonance.

To summarize, when the system is modulated at twice the natural frequency of the degenerate travelling modes, only the mode travelling in opposite direction to the stiffness wave (mode 3) resonates. At modulation frequency tuned to equal the natural frequency, the other mode in the degenerate pair (the previous mode's chiral partner) resonates. These conditions are predicted by Eq. (3.19) and Eq. (3.20).

The identification of one-way amplification in the ring of oscillators by the space-time Floquet matrix illustrates how it can predict the form of the resonant modes even when the normal modes are degenerate. We note that the eigenvectors of X_n are also eigenvectors of the Floquet matrix. The converse, however, is true only when the Floquet multipliers are all non-degenerate. Consider again the three oscillator system in Fig. 3.4. Since it has degenerate normal mode frequencies, the choice of the orthogonal normal mode basis vectors, and thus of the Floquet vectors in the static limit, is arbitrary. Even though the degeneracy structure of the Floquet matrix correctly predicts some parametric resonances, such as $T = \frac{2\pi}{\omega_2}$, it does not identify which mode in the degenerate normal mode subspace will experience amplification/decay. The eigenvectors of the space-time Floquet matrix, however, are non-degenerate and single out the two travelling modes as the physically relevant basis vectors for describing parametric amplification in the time-modulated system.

The breaking of chiral symmetry in the amplified modes is an example of reciprocity breaking in the system: wave propagation at the chiral resonances is highly asymmetric between the clockwise and counter-clockwise directions. This non-reciprocity would manifest as an asymmetry in the response of the other two masses when one mass is externally driven at the oscillatory frequency of the amplified mode. Non-reciprocity of vibrational waves away from parametric resonances has been proposed and observed in three-port acoustic circulators [37, 173]. In these prior works, the non-reciprocal response was due to a splitting in the oscillation frequencies of the clockwise and counter-clockwise modes due to a traveling-wave modulation. In our system, not only do the oscillation frequencies (related to the phase of the Floquet multipliers, see Appendix B.2) move away from each other, but the frequency of one of the traveling-wave modes becomes complex (signifying amplification) while the other remains real. This represents a qualitatively different form of reciprocity breaking tied to one-way amplification, which could be used to engineer mechanical amplifiers with favorable noise characteristics [132, 174].

3.3.3 Generalization to arbitrary space-time symmetric modulation

So far, we considered space-time symmetric modulation in the ring of coupled parametric oscillators with the specific phase shift $\tau = T/n$. We now briefly address general modulation patterns obtained by considering other values of τ.

If the phase shift is incommensurate with the periodic boundary conditions, i.e., $n\tau \bmod T \neq 0$, then the system hosts defects in the space-time modulation pattern and will be outside the scope of this work. Such a system may be analyzed using the theory of non-Hermitian Floquet defects and may exhibit the skin effect [175, 176].

To retain periodic boundary conditions, we must have $n\tau \bmod T = 0$, or equivalently $\tau = \frac{p}{q}T$ where p and q are positive integers with no common factors and q divides n. This constraint allows for the following two cases. First, if $q = n$, then our present analysis can still be applied to such a system, eg. $n = 7$ oscillators with a phase shift of $\tau = \frac{3}{7}T$. Explicitly, the Floquet matrix will now be factorized as $U(pT) = U(T)^p = [SU(\tau)]^n = [SU\left(\frac{p}{n}T\right)]^n$.

Second, we may have $q < n$, eg. $n = 24$ oscillators with a phase shift of $\tau = \frac{5}{8}T$. Such a system exhibits both the static translational symmetry at all times as well as space-time symmetry, i.e., it is a Floquet-Bloch lattice of n/q supercells each with q oscillators. Now the basis of vectors which are invariant on a translation by one oscillator (viz. the eigenvectors of S) not only diagonalize S, they also block-diagonalize the time-dependent Hamiltonian (since they are, in particular, also invariant on a translation by n/q oscillators). In such a basis, the matrices $H(t)$,

$U(t)$, and S in Eq. (3.15) and Eq. (3.16) are all block-diagonal and thus the space-time symmetry procedure can be applied to each block individually. Thus, while our framework is still applicable, the interplay of space-time symmetry with a Brillouin zone generates additional structure, such as winding numbers and bandgaps [40], which lie outside the scope of the current work and will be the subject of a future paper.

3.4 Discussion

In this work, we identified the non-Hermitian internal symmetries of the evolution operators governing the dynamics of a time-dependent linear classical mechanical system. Using these internal symmetries, which arise from the real-valuedness and symplecticity of the equations of motion, we derived the parametric resonance conditions for arbitrary periodically modulated coupled oscillator systems. These conditions are heralded by the collision of eigenvalues of opposite signature in the spectrum of the Floquet matrix—which can be exactly solved in the static limit.

We then examine systems with external symmetries, especially combined space-time symmetries. By proposing a new framework for space-time symmetric systems, in terms of the space-time Floquet matrix, we find the conditions for these protected degeneracies (which lead to modes that are protected from parametric resonance and do not exhibit amplification or decay). These conditions are formulated from the symmetries of the system alone without relying on the functional form of the modulation.

While protected degeneracies have been observed in the Floquet spectra of quantum as well as classical systems with time-modulated parameters (in the two-oscillator system [139, 150, 177, 178] and in space-time symmetric lattices [154]), their origins were not fully understood previously. We show that protected degeneracies form when the space-time Floquet matrix, which captures the long-time behavior of a space-time symmetric system, is raised to an integer power to get the ordinary Floquet matrix. If distinct eigenvalues of the former matrix become degenerate in the latter, they are protected from resonance.

Furthermore, our framework allows us to solve for the conditions for one-way amplification in a system with periodic boundary conditions, such as a ring of oscillators. Remarkably, these conditions show that one can control which direction of signal propagation is amplified simply by tuning the modulation frequency in a space-time symmetric system, representing a strong breaking of reciprocity in the system dynamics. Amplification of one-way modes has been seen in non-Hermitian Floquet systems before in both numerics [151, 179] and experiments [180]. Our analysis, specifically through Equations (3.19) and (3.20), provides general conditions for the existence of one-way amplification in terms of the mode structure in the static limit. In contrast to approaches such as in Ref. [181], we do not rely on any particular forms of the modulation function to generate directional amplification. Indeed, all of our analysis depends only on the symmetries of the system and applies to arbitrary functional forms of the time modulation. Our framework for space-time symmetry is applicable to all systems, Hermitian as well as non-Hermitian, with such symmetry [182].

We expect the insights provided by our theoretical study to enable the engineering of amplification, unidirectional transport, as well as protected eigenvalue degeneracies in space-time modulated materials. Since the onset of parametric resonance is triggered by an exceptional degeneracy [29], our results can also be used to engineer sensing [169] and mode-switching devices [22] based on exceptional-point physics.

The one-way amplified modes could also serve as the basis for limit cycles that do useful mechanical work in the presence of nonlinearities [183]. The formulation based on the space-time Floquet matrix shows that space-time symmetric systems may be used to realize non-trivial n-root analogs of systems with topologically protected states [184, 185]. Other promising directions for future work include a detailed analysis of the interplay of space-time symmetry with band structures in systems where the space-time modulation leads to a lattice of supercells, and the influence of open boundary conditions which can cause dramatic changes in non-Hermitian spectra [54].

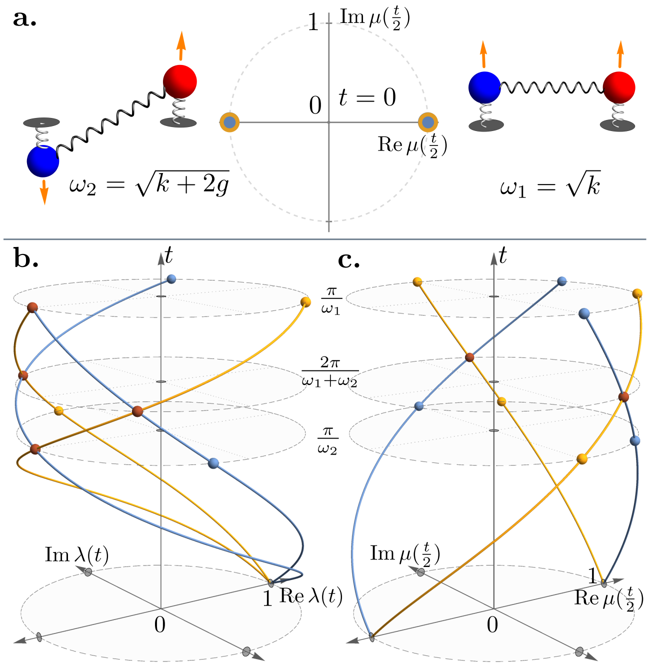

Figure 3.3. Dimer ($n = 2$) with space-time symmetry. **a.** Snapshots showing displacement and velocity of each mass in the anti-bonding (left) and bonding (right) modes. Each mode contributes a pair of eigenvalues with opposite Krein signature to the spectrum of $SU(t/2)$ (center), shown as a blue disc and a yellow circle at $\mu = +1$ (bonding mode) and at $\mu = -1$ (anti-bonding mode) when $t = 0$. We consider the static limit $\delta \to 0$ to find the conditions of parametric resonance. **b.** As time increases, the eigenvalues $\lambda(t)$ of $U(t) = e^{-iHt}$ of positive (negative) signature, shown in blue (yellow), move clockwise (counter-clockwise) along the unit circle starting from $\lambda(t=0) = +1$. Unstable degeneracies (red points) form at times equal to $\frac{\pi}{\omega_2}$, $\frac{2\pi}{\omega_1+\omega_2}$, and $\frac{\pi}{\omega_1}$ (and their integer multiples). **c.** For a space-time symmetric modulation, the correct conditions for resonance are given by the matrix $SU(t/2) = Se^{-iHt/2}$ whose eigenvalues are $\mu(t/2)$. As the spectrum of $SU(t/2)$ evolves with time, unstable degeneracies occur only at $t = \frac{2\pi}{\omega_1+\omega_2}$. At $t = \frac{\pi}{\omega_2}$ and $t = \frac{\pi}{\omega_1}$, even though the eigenvalues $\lambda(t) = [\mu(t/2)]^2$ are degenerate (at -1), the eigenvalues $\mu(t/2)$ are not (the corresponding values are $+i$ and $-i$).

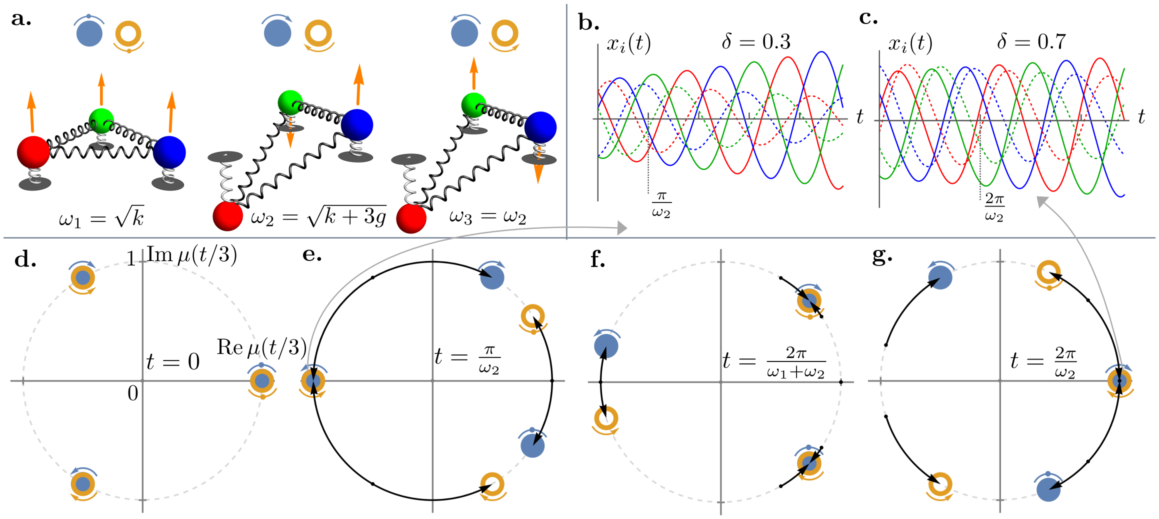

Figure 3.4. Trimer ($n = 3$) with one-way propagating modes. The space-time symmetric modulation corresponds to a travelling wave of stiffness for the grounding springs with the maximum stiffness cycling in order of colors $R \to G \to B$ (clockwise). **a.** Snapshots showing representative displacements and velocities of the masses for the three normal modes in the $\delta \to 0$ limit: a mode with all three masses oscillating in phase (left), and two degenerate travelling-wave modes with $\kappa = \pm 2\pi/3$—one travelling clockwise in the same direction as the stiffness wave (center), and the other travelling counter-clockwise (right). Symbols above the modes denote corresponding eigenvalues in panels **d–g**, colored by Krein signature as in Fig. 3.2. **b.** Numerically computed time traces of the oscillator positions when initialized to the amplified (continuous curve) and damped (dotted curve) Floquet eigenvectors (we used $k = 10$, $g = 3$, $\delta = 0.3$, $T = \frac{\pi}{\omega_2}$, and $f(t) = \cos(2\pi t/T)$). At this resonance, only the counterclockwise propagating mode resonates (peak follows $R \to B \to G$ with time). **c.** Same as **b**, (but at $T = \frac{2\pi}{\omega_2}$ and $\delta = 0.7$) for which only the clockwise mode experiences resonance. **d.–g.** Eigenvalues $\mu(t/3)$ of $SU(t/3) = Se^{-iHt/3}$ in the static limit $\delta \to 0$ at values of time (labels) for which pairs of eigenvalues with opposite Krein signature collide.

CHAPTER IV

USING SPACE-TIME SYMMETRY TO DESIGN TOPOLOGICAL PHASES

This chapter reports preliminary investigations of the topological features of Floquet bands for crystals exhibiting space-time symmetry. In the previous chapter we identified such a symmetry in a ring of oscillators modulated with a traveling wave modulation and developed a framework to study such a system. Part of this chapter will involve this framework to lattices.

4.1 Introduction

Here, we develop a framework to study space-time symmetric linear systems which is more powerful than the conventional Floquet framework.

4.2 System

We consider systems with space-time symmetry [40, 41, 154] as well as periodic boundary conditions (PBC). This combination generically gives rise to discrete translational symmetry in the system. We will frame our discussion in terms of an example system of a 1D lattice with PBC and a Hamiltonian given by

$$\mathcal{H}(t) = \frac{p^2}{2m} + V(x,t). \tag{4.1}$$

The system has discrete translational symmetry with n repeating supercells—when $n = 1$ we have a ring rather than a periodic lattice. The system has space-time symmetry if it satisfies

$$V(x+b, t+\tau) = V(x,t). \tag{4.2}$$

That is, a traveling wave with velocity $v = \frac{b}{\tau}$ modulates the system. The displacement b may be positive or negative, depending on the direction of the travelling wave [1], with $|b|$ being the shortest length for which such an equation may be written. The time-step τ is taken to be positive.

If the system size is $L = mn|b|$, where m is a positive integer, periodic boundary conditions require that $V(x,t) = V(x+mnb,t) = V(x,t-mn\tau)$. Thus $V(x,t)$ is required to be a time-periodic function with some time-period T whose general form is $T = \frac{m}{p}\tau$, with p a positive integer coprime with m [2].

Space-time symmetry together with periodic boundary conditions endows the system with discrete translational symmetry since $V(x+mb,t) = V(x,t-pT) = V(x,t)$. The system is then a lattice consisting of n supercells and invariant under a discrete translation $(x,t) \mapsto (x+a,t)$ where $a := m|b|$.

Using the commensurateness condition on T and τ we now define $\tau_0 > 0$ via

$$\tau_0 := \frac{T}{m} = \frac{\tau}{p}. \tag{4.3}$$

A space-time symmetric system's long-time behavior is fully captured by numerical integration of the system's equations of motion up to time equalling $\tau_0 = \frac{T}{m}$ (see Eq. (4.7)). This is in contrast to a generic Floquet (time-periodic) system which requires a numerical integration up to the time period T. Using Bézout's identity we

---

[1] The sign of b is chosen such that the associated τ is smaller. For example, the equation $V(x+b,t+\tau) = V(x,t)$ implies that $V(x,t) = V(x-b,t-\tau) = V(x-b,t+\frac{m-p}{p}\tau)$. We require that $\frac{m-p}{p} > 1$. If $\frac{m-p}{p} < 1$, we reverse the direction of b. If $2p = m$ (which only occurs when $m = 2$ and $p = 1$), the choice of sign of b does not matter as the left-right symmetry is unbroken and there is no traveling wave modulation.

[2] The integer p can always be chosen to be smaller than m which we will assume is the case. If p is larger than m replace p with $p \bmod m$.

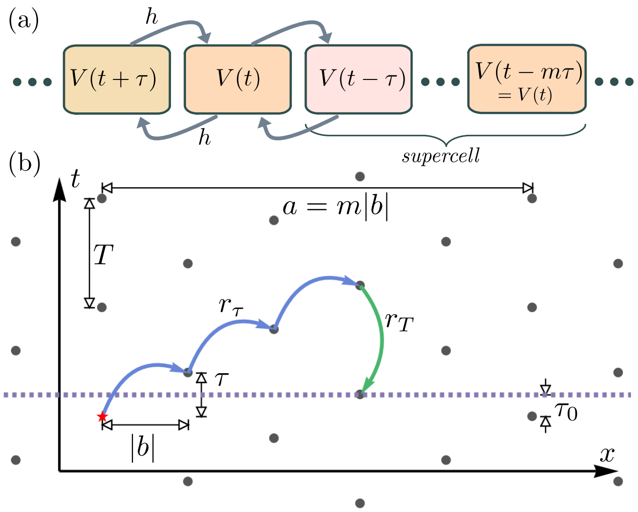

Figure 4.1. **a.** A schematic of a 1D lattice with space-time symmetry where h denotes the hopping term and $V(t)$ the onsite potential. The lattice is invariant under the transformation $(x, t) \mapsto (x + b, t + \tau)$. **b.** Its symmetry structure can be visualized by points (shown in dark gray) of space and time at which the system is equivalent to a special chosen point (red star). Periodic boundary conditions ensure that the lattice is also invariant under $(x, t) \mapsto (x, t + T)$ where the time-period $T = \frac{m}{p}\tau$, and $(x, t) \mapsto (x + a, t)$ where $a := m|b|$. The co-prime integers m and p (here, 5 and 2 respectively) determine the symmetry structure. Integers r_T and r_τ (here, -1 and 3 respectively) defined such that $1 = r_T m + r_\tau p$ determine τ_0 the smallest time-step of numerical integration needed to capture the long-time behavior of the system.

define integers r_T and r_τ such that $\tau_0 = r_T T + r_\tau \tau$ [3] such that

$$\begin{aligned} V(x, t) &= V(x + r_\tau b, t + r_\tau \tau + r_T T), \\ &= V(x + r_\tau b, t + \tau_0). \end{aligned} \tag{4.4}$$

For the commonly occuring case of $\tau = T/m$, the integer r_τ is unity. The definitions above are visually summarized in Fig. 4.1.

We now define $S(r) := e^{i\,\mathrm{sgn}(b) r p} = e^{\mathrm{sgn}(b) r \frac{d}{dx}}$ to be the translation operator in the direction of the modulation wave. Here, sgn(b) denotes the sign of b and we set

---

[3] The set of all such solutions can be represented in the form $\{r_T^0 - kp, r_\tau^0 + km\}$ where k is an integer and $\{r_T^0, r_\tau^0\}$ is a particular solution. To fix the solutions we can choose k such that $0 < r_\tau < m$.

$\hbar = 1$. The displacement operator satisfies $S(r)\Psi(x) = \Psi(x + \mathrm{sgn}(b)r)$. We can now write the Hamiltonian's space-time symmetry, discrete translational symmetry, and Floquet symmetry respectively as

$$\mathcal{H}(t) = S(r_\tau|b|)\mathcal{H}(t+\tau_0)S^{-1}(r_\tau|b|), \tag{4.5a}$$

$$\mathcal{H}(t) = S(a)\mathcal{H}(t)S^{-1}(a), \tag{4.5b}$$

$$\mathcal{H}(t) = \mathcal{H}(t+T). \tag{4.5c}$$

The time-propagation matrix inherits these symmetries and satisfies

$$U(t+\tau_0) = S^{-1}(r_\tau|b|)U(t)S(r_\tau|b|)U(\tau_0), \tag{4.6a}$$

$$U(t) = S(a)U(t)S^{-1}(a), \tag{4.6b}$$

$$U(t+T) = U(t)U(T). \tag{4.6c}$$

The long-time behavior of the space-time symmetric system is deduced by applying Eq. (4.6a) (which we prove in Appendix 4.5.1) k times to get

$$U(t+k\tau_0) = S(r_\tau|b|)^{-k}U(t)[S(r_\tau|b|)U(\tau_0)]^k. \tag{4.7}$$

4.3 BAND STRUCTURE

Combining this space-time formulation with the discrete translational symmetry of the system allows us to define a 'space-time band structure' generalizing the Floquet band structure. For this, choose a basis of states that simultaneously block-diagonalizes the matrices $\mathcal{H}(t)$, $U(t)$, and $S(r_\tau|b|)$. The eigenstates of $S(|b|)$ which are Bloch states with $\Psi(x+b) \propto \Psi(x)$ provide such a basis. In particular, they are also the eigenstates of $S(a) = S(m|b|) = S^m(|b|)$ and satisfy $\Psi(x+a) = \lambda\Psi(x)$ for some eigenvalue λ. Since both $\mathcal{H}(t)$ and $U(t)$ commute with $S(a)$, they can be block-diagonalized in the basis of these eigenstates. The block matrices so formed act on the uncoupled Bloch subspaces.

The eigenvalues λ take n unique values given by $e^{i\frac{2\pi j}{n}}$ with $j \in \{0, 1, \ldots, n-1\} = \mathbb{Z}_n$. Thus,

$$\mathcal{H}(t) = \mathcal{H}_0(t) \oplus \cdots \oplus \mathcal{H}_{n-1}(t) = \oplus_{j\in\mathbb{Z}_n}\mathcal{H}_j(t). \tag{4.8}$$

Similarly, $U(t) = \oplus_{j\in\mathbb{Z}_n}U_j(t)$ and $S(r_\tau|b|) = \oplus_{j\in\mathbb{Z}_n}S_j(r_\tau|b|)$. Here, the operator $\oplus$ denotes the direct sum and matrices labelled by the subscript j denote the different block matrices. Using $(\oplus_j X_j)(\oplus_j Y_j) = \oplus_j(X_jY_j)$ we get

$$U_j(t+\tau_0) = S_j^{-1}(r_\tau|b|)U_j(t)S_j(r_\tau|b|)U_j(\tau_0) \tag{4.9}$$

and applying this m times,

$$\begin{aligned} U_j(T) = U_j(m\tau_0) &= S_j^{-1}(r_\tau a)[S_j(r_\tau|b|)U_j(\tau_0)]^m, &(4.10)\\ &= \lambda_j^{-r_\tau}[S_j(r_\tau|b|)U_j(\tau_0)]^m. &(4.11)\end{aligned}$$

The last equation results from $S_j(a) = \lambda_j\mathbb{I}$ in the chosen basis. We define

$$X_j(\tau_0) := \lambda_j^{-\frac{r_\tau}{m}}S_j(r_\tau|b|)U_j(\tau_0) \tag{4.12}$$

as the jth block of the *space-time Floquet matrix*. In this definition we take the principal mth root of $\lambda_j^{-r_\tau}$. The important result is that each Bloch block of the Floquet matrix can be factorized as $U_j(T) = X_j^m(\tau_0)$.

Adopting a continuum notation ($n \to \infty$) such that the eigenvalue of $S(a)$ becomes $\lambda = e^{i\frac{2\pi}{n}} \to e^{ika}$ with the wavevector $k \in (-\frac{\pi}{a}, \frac{\pi}{a}]$, we label the submatrices by the corresponding value of k,

$$\begin{aligned} U(k,T) &= X^m(k,\tau_0), &(4.13)\\ X(k,\tau_0) &= e^{-i\frac{r_\tau}{m}ka}S(k, r_\tau|b|)U(k,\tau_0), &\\ &= e^{-ir_\tau k|b|}S(k, r_\tau|b|)U(k,\tau_0). &(4.14)\end{aligned}$$

The eigenvectors of the space-time Floquet matrix $X(k,\tau_0)$ are also eigenvectors of the Floquet matrix $U(k,T)$ (although the converse is not necessarily true). These eigenvectors satisfy

$$X(k,\tau_0)\Psi(x,t) = e^{-ir_\tau k|b|}\Psi(x + r_\tau b, t + \tau_0) \propto \Psi(x,t) \tag{4.15}$$

and are thus invariant, upto a multiplicative factor, on a space-time translation. We define the effective Hamiltonian $\mathcal{H}_{\text{eff}}(k)$ of the system by $e^{-i\mathcal{H}_{\text{eff}}\tau_0} := X(k,\tau_0)$ and denote its jth eigenvalue by $\omega_j(k)$. The eigenvalue $\omega_j(k)$ is defined upto integer multiples of $\frac{2\pi}{\tau_0} = \frac{2\pi m}{T}$. By Eq. (4.13), the Floquet multipliers are given by $(e^{-i\omega_j(k)\tau_0})^m = e^{-i\omega_j(k)T}$ and thus $\omega_j(k)$ precisely denote the Floquet frequencies of the system. With the Floquet frequencies defined upto integer multiples of $\frac{2\pi m}{T}$ rather than $\frac{2\pi}{T}$ we avoid extraneous foldings and unphysical degeneracies in the band structure.

Fig. 4.2**a** shows a schematic plot of the dimensionless space-time band structure $\omega_j(ka)\tau_0$ vs. ka with Fig. 4.2**b** depicting the corresponding dimensionless Floquet band structure. The former is composed of repeated copies of a square Brillouin zone (BZ) defined by the square stretching from $-\pi$ to $+\pi$ in both horizontal and vertical directions. On a conventional Floquet-Bloch band structure [Fig. 4.2**b**], a point $(ka, \omega T)$ is identified with the points $(ka + 2\pi, \omega T)$ and $(ka, \omega T + 2\pi)$. In contrast, in the band structure defined using space-time symmetry, $(ka, \omega\tau_0)$ is identified with $\left(ka + 2\pi, \omega\tau_0 - \frac{r_\tau 2\pi}{m}\right)$ and $(ka, \omega\tau_0 + 2\pi)$. The frequencies $\omega_j(-\pi)\tau_0$ do not equal $\omega_j(+\pi)\tau_0$ and the band structure does not tile in the conventional manner. This can be traced back to the mth root taken in Eq. (4.12). Defining an obliquely shaped torus as the Brillouin zone (drawn with red dots in the figure) recovers conventional tiling with repeated units touching at the corners [cite]. However, we shall continue to use the square Brillouin zone for the rest of the paper.

The BZ can be divided into m horizontal strips of height $\frac{2\pi}{m}$ (see Fig. 4.2**a**). The conventional Floquet-Bloch band structure, obtained by plotting the eigenvalues

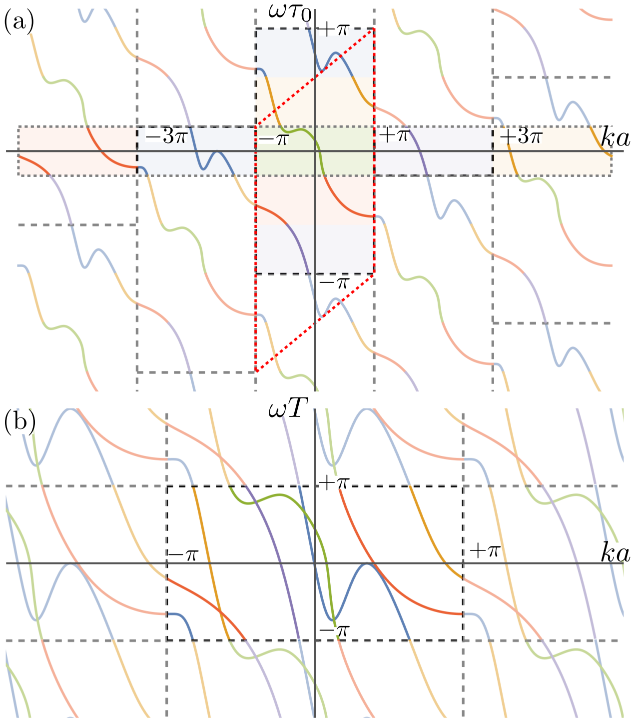

Figure 4.2. **a.** Schematic of a dimensionless space-time band structure with two bands and no degeneracies for a system with $\tau = \frac{p}{m}T = \frac{2}{5}T$. Dashed black lines show the square BZ, the red dotted ones depict the oblique BZ, and the gray dotted lines show the horizontal BZ. The $m = 5$ strips of height $\frac{2\pi}{m}$ that form the square BZ and the horizontal BZ are colored with different colors. **b.** The corresponding Floquet BZ is created by superimposing these $m = 5$ strips leading to unphysical degeneracies.

of $i \log [U(k, T)]$ vs the crystal momentum ka, is reproduced from the space-time band structure by superimposing the m strips. This is the source of the unphysical degeneracies noticed previously in the literature.

An alternate BZ is the rectangle which stretches vertically from $-\frac{\pi}{m}$ to $+\frac{\pi}{m}$ and horizontally from $-m\pi$ to $+m\pi$ which we call 'the horizontal BZ'. This rectangle covers all unique parts of the band structure as we prove in Appendix 4.5.2. In a conventional Brillouin zone eigenvalues associated with different values of the wavevector are uncoupled since they belong to different Bloch subspaces. However, in the horizontal BZ, an eigenvalue at $\omega_j(ka)\tau_0$ will couple with another eigenvalues at $\omega_i(ka + 2r\pi)\tau_0$ where r is any integer. When an eigenvalue $(ka, \frac{\pi}{m})$ hits the top of this rectangle it re-enters the rectangle at $(ka + 2p\pi, -\frac{\pi}{m})$ since $p = r_\tau^{-1} \bmod m$ [4] (see Fig. 4.2**a**). As we shall see in the examples of the next section, this 'horizontal scheme' is easiest to visualize and connects best with the static system.

4.3.1 Weak modulation limit

As a special case we consider systems with weak modulation. For example consider the Hamiltonian

$$\mathcal{H}(t) = \frac{p^2}{2m} + V_0\left(\frac{x}{b}\right) + \delta V_s\left(\frac{px}{mb} - \frac{t}{T}\right) \tag{4.16}$$

with $b > 0$ and $\delta \ll 1$. The functions $V_0(.)$ and $V_s(.)$ are periodic with period one and we shall consider the latter, which is space-time symmetric, as a perturbation on the static system. In the adiabatic regime this Hamiltonian models a Thouless pump. In the limit $\delta \to 0$, the Hamiltonian commutes with $S(b)$ and can be block-diagonalized as $\mathcal{H}(qb)$ with e^{iqb} being an eigenvalue of $S(b)$. The eigenvalues of each block $\mathcal{H}(qb)$ are denoted by $\Omega_j(qb)$ where j labels the static band.

When δ is turned on, the system shall lose the symmetry under translation by b and is now invariant only after a translation by $a = mb$. The m blocks $\mathcal{H}(q_l b)$, such that $(e^{iq_l b})^m = e^{ikmb}$ or $q_l = k$ upto multiples of $\frac{2\pi}{a}$, can now couple to each other. The space-time band structure can be constructed from the static band structure in the following way (see Appendix 4.5.3 for details). First one divides the static band-structure $\Omega_j(qb)\tau_0$ into horizontal strips of height $\frac{2\pi}{m}$. These strips are then superimposed on top of each other after shifting each strip, whose center is at height $\frac{2\pi j}{m}$, horizontally by $-2p\pi$. Thus, the strip running from $-\frac{\pi}{m}$ to $+\frac{\pi}{m}$ in the vertical direction is left untouched, the stip directly above it is shifted horizontally by $-2p\pi$

---

[4] $1 = r_T m + r_\tau p$ implies $1 = p r_\tau \bmod m$.

and the one below it by $+2p\pi$. The degeneracies formed on the superimposition of these strips couple as δ is turned on. Physically, these degeneracies repel when the Hamiltonian is Hermitian due to level repulsion, and can give rise to exceptional points signalling amplification when the Hamiltonian is non-Hermitian.

4.4 EXAMPLES

4.4.1 One-way amplification of waves in mechanical metamaterials

In ref. [151], the authors considered a chain of particles of unit mass connected to each other with springs of rest length $b = 1$ and stiffness k_0. The particles are constrained to oscillate longitudinally. When the ith spring in the chain modulated as $k_i(t) = k_0\left[1 + \delta\cos\left(\frac{2\pi}{m}i - \frac{2\pi p}{T}t\right)\right]$, a stiffness wave with speed $v_\mathrm{m} = \frac{m}{pT}$ is set up in the chain. Here, m and p are integers with the same meaning as defined in the general theory above—m corresponds to the number of degrees of freedom in a unit cell and p quantifies the phase shift (ref. [151] only considers $p = 1$).

When $\delta \to 0$, the static chain's dispersion relation is $\Omega_\pm(q) = \pm 2\sqrt{k_0}\sin(q/2)$ which for small wavevectors is linear, $\Omega_\pm(q) \sim \pm\sqrt{k_0}q$. We identify $v_\mathrm{s} = \sqrt{k_0}$ as the speed of sound in the chain. By tuning the speed of the modulation wave v_m to match the speed of sound v_s, the waves travelling in the direction of the stiffness wave are amplified while the ones travelling in the opposite direction are not. The gain factors are fairly constant throughout the band which makes the amplification fairly dispersion-free.

Using the fact that the system is space-time symmetric, we can develop a more solid theoretical framework to explain the phenomena without resorting to perturbation theory. Our strategy is to examine the space-time band structure in the $\delta \to 0$ limit, which can be constructed out of the static band structure, to design the conditions for amplification. This corresponds to dividing the static band structure into strips of height $\frac{2\pi m}{T}$ and superimposing them after appropriate horizontal shifts of integer multiples of $\frac{2\pi p}{m}$ as shown in Fig. 4.3**a** and Fig. 4.3**c**. For the modes to resonate and amplify, we need eigenvalues of the + band to be near those from the − band so that they couple when modulation is turned on. This would happen if the bands in strips being superimposed have similar shapes. In the linear regime, $\Omega_{\pm}(q) \sim \pm\sqrt{k_0}q$,if the horizontal shift between two consecutive strips $\frac{2\pi p}{m}$ equals the horizontal projection of the band in the strip $\frac{1}{\sqrt{k_0}}\frac{2\pi}{T}$, then two near linear parts of the band will superimpose. Thus we expect amplification when $T = \frac{m}{p\sqrt{k_0}}$ or $v_{\mathrm{m}} = v_{\mathrm{s}}$ recovering the results from perturbation theory [151].

As the modulation is turned on ($\delta > 0$), the eigenvalues of the bands which are close by begin to couple and become complex-valued as shown in Fig. 4.3**b** and Fig. 4.3**d**. Since corresponding eigenvalues of the two superimposing bands are about the same distance apart in the linear regime, the gain factors (or the imaginary part of the frequencies) are fairly uniform across the band. In the space-time band structure all pairs of eigenvalues which come from different bands and overlap become complex-valued when the system is modulated. The Floquet band structure on the other hand exhibits extraneous degeneracies where the eigenvalues do not couple.

4.5 DETAILS OF SOME CALCULATIONS IN PREVIOUS SECTIONS

4.5.1 Derivation of the space-time Floquet theorem

For the time-propogation operator, we have (with $\mathcal{T}$ being the time-ordering operator),

$$\begin{aligned} U(t+\tau_0) &= \mathcal{T}\left[\exp\left(-i\int_0^{t+\tau_0} dt' H(t')\right)\right] \\ &= \mathcal{T}\left[\exp\left(-i\int_{\tau_0}^{t+\tau_0} dt' H(t')\right)\right] U(\tau_0) \\ &= \mathcal{T}\left[\exp\left(-i\int_0^{t} dt' S^{-1}(r_\tau|b|) H(t') S(r_\tau|b|)\right)\right] U(\tau_0) \\ &= S^{-1}(r_\tau|b|) U(t) S(r_\tau|b|) U(\tau_0). \end{aligned} \tag{4.17}$$

If $S(r_\tau|b|)$ was identity such that $\mathcal{H}(t) = S(r_\tau|b|)\mathcal{H}(t+\tau_0)S^{-1}(r_\tau|b|) = \mathcal{H}(t+\tau_0)$, then this derivation would recover Floquet's theorem.

4.5.2 Proof that the horizontal BZ can be used to tile the band structure

In the dimensionless band structure $\omega_j(ka)\tau_0$ vs. ka, the square BZ that stretches from $-\pi$ to $+\pi$ in both horizontal and vertical directions can tile the band structure. We need to show that the horizontal BZ corresponds to these m strips of the square BZ of height $\frac{2\pi}{m}$ laid horizontally next to each other in some order. We know that a point $(ka, \omega\tau_0)$ on the band structure is identified with $\left(ka + 2j\pi, \omega\tau_0 - j\frac{r_\tau 2\pi}{m}\right)$ where j is any integer. The horizontal BZ is constructed by following the strips stretching vertically from $-\frac{\pi}{m}$ to $+\frac{\pi}{m}$ in the horizontal direction covering a length of $2m\pi$ which corresponds to following the sequence $j = 0, 1, \ldots, m-1$.

Thus, all we need to show is that the integers $jr_\tau \bmod m$ with $j \in \mathbb{Z}_m$ are all unique. Equivalently, we need to prove that $r_\tau j$ is not a multiple of m where j is an integer between 1 and $m-1$. Assume for the sake of contradiction that $r_\tau j = 0 \bmod m$ for j an integer between 1 and $m-1$.. Now $1 = r_T m + r_\tau p$, the defining equation for r_T and r_τ, implies that $r_\tau p = 1 \bmod m$ or $r_\tau p j = j \bmod m$. Thus $0 = j \bmod m$ which is a contradiction.

4.5.3 Constructing the space-time band structure from the static band structure in the weak modulation limit

Labelling each q_l by $q_l = k + l\frac{2\pi}{m|b|}$ with $l \in \mathbb{Z}_m$, we can define the larger blocks $\mathcal{H}(ka) = \oplus_{j\in\mathbb{Z}_m}\mathcal{H}(q_l|b|)$ which act on subspaces which remain invariant even after the modulation is turned on. Now the system's dynamics is captured by the block matrices $X(ka,\tau_0)$ which at small modulation is given by

$$X(ka,\tau_0) \sim e^{-ir_\tau kb} S(k, r_\tau b) \exp\left(-i\mathcal{H}_0\left(ka\right)\tau_0\right) \tag{4.18}$$

and thus its eigenvalues are given by

$$\begin{aligned} e^{-i\omega_{jl}(ka)\tau_0} &= \exp\left[ir_\tau b\left(q_l - k\right) - i\Omega_j(q_l|b|)\tau_0\right], \\ &= \exp\left[ir_\tau b\frac{2\pi l}{m|b|} - \Omega_j(q_l|b|)\tau_0\right]. \end{aligned} \tag{4.19}$$

Now, consider the system modulated at a high frequency such that the modulation time period T is small compared to the time-scales of the static system. Specifically, consider the case where $-\frac{\pi}{T} < \omega_{jl}(ka) < +\frac{\pi}{T}$ or $-\frac{\pi}{m} < \omega_{jl}(ka)\tau_0 < +\frac{\pi}{m}$ for all frequencies $\omega_{jl}(ka)$. In the horizontal BZ, at any value of ka, only those frequencies $\Omega_j(q_l|b|)$ appear for which $q_l = k$. Thus as we go from $ka = -m\pi$ to $ka = +m\pi$ (which is the same as $q_l|b| = -\pi$ to $q_l|b| = +\pi$) the band-structure plots $\omega_{jl}(ka)\tau_0 = \Omega_j(q_l|b|)\tau_0$ which is precisely the static band-structure without any folding. As we increase the time-period of modulation, some eigenvalue $(ka, \omega_{jl}(ka)\tau_0)$ will hit either the top of the horizontal BZ at $(ka, +\frac{\pi}{m})$ or the bottom at $(ka, -\frac{\pi}{m})$. It then re-enters the BZ according to the rules laid down in the main text.

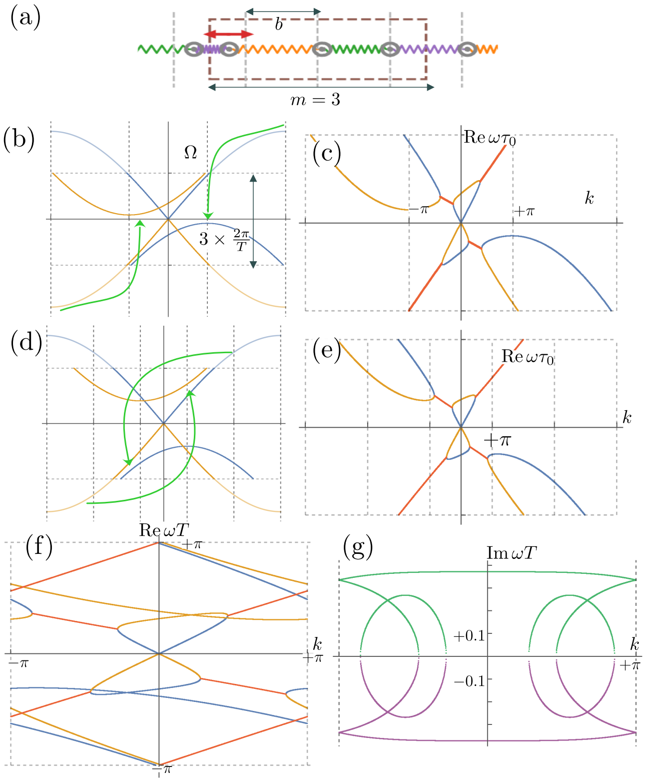

Figure 4.3. **a.** A chain of masses connected by springs modulated in a travelling wave fashion. **b., d.** The static band structure of the unmodulated chain (translucent curve) can be transformed into the space-time band structure at infinitesimal modulation according to the discussion on the weak modulation limit. **b.** shows the case for $m = 3, p = 1$ and **d.** corresponds to $m = 5, p = 2$. **c., e.** At finite modulation strength frequency eigenvalues of the upper band (blue) couples with those in the lower band (yellow) and become complex-valued (red). **c., e.** correspond to the parameters in **b., d.** respectively. **f., g.** Real and imaginary parts of the Floquet band-structure corresponding to the space-time band-structure in **e.**. **g.** shows how the band is amplified almost uniformly across its expanse.

CHAPTER V

DEGENERACIES AND SYMMETRY BREAKING IN PSEUDO-HERMITIAN MATRICES

This work was published in Physical Review Research as Ref. [29]. Compared to the original text there is one small correction in the Appendix.

5.1 Introduction

Linear operators, such as those representable by matrices, are ubiquitous in physics forming many exact models of nature. They also occur as effective models when a more fundamental model is linearized around a point of interest. While Hermitian matrices are common in canonical quantum mechanics, the richer behavior of non-Hermitian matrices is being increasingly used to model gain/loss in open systems [2, 161], phase transitions [42, 74, 116], sensitivity to boundary conditions [52, 175], and various other phenomena excluded by assumptions of Hermiticity.

Pseudo-Hermitian matrices [186] are non-Hermitian matrices that can be similarity-transformed to their adjoints, $H = G^{-1}H^{\dagger}G$. They are ubiquitous in classical physics [18, 42, 151, 161, 187] since all real-valued matrices are pseudo-Hermitian. Matrices with time-reversal symmetry [188] or with parity-time symmetry ($\mathcal{PT}$-symmetry) [189] are also pseudo-Hermitian (see **Section 5.2**)—the latter being one of the earliest classes of non-Hermitian matrices to be analyzed in terms of symmetries [21, 190].

Upon tuning some parameter, degenerate real eigenvalues of a pseudo-Hermitian matrix can turn into complex conjugate pairs. This phenomenon is known as spontaneous pseudo-Hermiticity breaking (henceforth simply called symmetry breaking) since it is accompanied by a change in the symmetries of the corresponding eigenvectors. Typically, the parameter quantifies an external source of bias, amplification, or dissipation [2, 42]. Upon symmetry breaking the system exhibits qualitatively different behavior usually signifying the emergence of amplified/dissipated modes [2] or even different thermodynamic phases [74, 116, 191]. Systematically analyzing the conditions for pseudo-Hermiticity breaking is then crucial to understanding the physical properties and potential applications of pseudo-Hermitian systems.

In this paper, we provide the necessary and sufficient conditions for symmetry breaking to occur in a pseudo-Hermitian matrix, H. We use the intertwining operator G, whose expectation value is a conserved quantity [192], to classify the eigenspace of H. We demonstrate that symmetry breaking occurs when and only when eigenvalues associated with opposite signs of the conserved quantity collide on the real axis. This allows one to predict which real-valued degeneracies of a pseudo-Hermitian matrix can lead to symmetry breaking, and hence are "unstable degeneracies".

By characterizing the degeneracies we also determine the sets of pseudo-Hermitian matrices with real eigenvalues that can be continuously connected to each other without ever encountering symmetry breaking. These in turn correspond to all the disconnected stable phases (regions in parameter space where all eigenvalues are real) of a physical system.

Non-Hermitian matrices exhibit two types of eigenvalue degeneracies—diabolic points (DPs), where the number of independent eigenvectors equals the number of times an eigenvalue is repeated, and exceptional points (EPs) [58, 193, 194], where the matrix cannot be diagonalized and its eigenvectors fail to span the complete space. We find that these disconnected regions in parameter space, where all eigenvalues are real, are surrounded by exceptional surfaces, which comprise all the real-valued

EPs of pseudo-Hermitian matrices. Exceptional surfaces that are boundaries to two different regions may meet, annihilating each other and giving rise to DPs. These exceptional surfaces, together with the diabolic points created by their intersections, comprise all points of pseudo-Hermiticity breaking.

Furthermore, degeneracies in Hamiltonian matrices are either accidental or caused by symmetries. In this paper, we also use the intertwining operator to derive the conditions for when degeneracies caused by external symmetries are susceptible to thresholdless pseudo-Hermiticity breaking (i.e., symmetry breaking at infinitesimal amounts of non-Hermiticity).

Much of our paper builds on the insight by Refs. [27, 195, 196] that pseudo-Hermitian matrices can be mapped to $G-$Hamiltonian matrices, a class of matrices studied by Krein, Gel'fand, Lidskii, and others in the context of stability of mechanical systems [28, 164, 197, 198]. This mapping is being increasingly used in works on quadratic Bosonic systems [199, 200] that can be described by an effective Bogoliubov-de Gennes (BdG) Hamiltonian that is pseudo-Hermitian. (See Ref. [201] for a detailed analysis.)

This article is structured as follows. We define pseudo-Hermitian matrices and intertwining operators in **Section 5.2** and review the phenomenon of pseudo-Hermiticity breaking. In **Section 5.3** we use the intertwining operator to classify the eigenspace. In **Section 5.4** we provide the main results of the paper including the conditions for pseudo-Hermiticity breaking to occur and the classification of stable phases of a pseudo-Hermitian matrix. These results are illustrated via a schematic example in **Section 5.5**. In **Section 5.6** we characterize the boundaries of the stable phases, i.e., the points of symmetry breaking. We then discuss conserved quantities in pseudo-Hermitian systems and the interplay of pseudo-Hermiticity with degeneracies caused by external symmetries in **Section 5.7**. In Sec. 5.8, we provide illustrative examples of well-known pseudo-Hermitian Hamiltonians from photonics, condensed matter physics, and mechanics.

5.2 PSEUDO-HERMITIAN MATRICES AND SYMMETRY BREAKING

A matrix H is called pseudo-Hermitian if it is similar to its conjugate transpose. That is

$$H = G^{-1} H^{\dagger} G \tag{5.1}$$

for some invertible matrix G called the intertwining operator [192, 202]. G is not unique and can always be chosen to be Hermitian [27], which we will assume is the case from here on. Since every matrix is similar to its transpose, an equivalent definition is that H is similar to its complex conjugate,

$$H = S H^{*} S^{-1} \tag{5.2}$$

for some invertible matrix S. A real matrix is then trivially pseudo-Hermitian. The equation above can also be written as $[H, S\mathcal{T}] = 0$ where $\mathcal{T}$ is the antilinear complex-conjugation operator, which acts as the time-reversal operator. For this reason, H is also said to be $S\mathcal{T}$ symmetric—a familiar case is when S is the parity operator $\mathcal{P}$.

Non-Hermitian matrices with the $\mathcal{K}$ or $\mathcal{Q}$ internal symmetries (in the Bernard-LeClair notation [24, 56, 152]) are all special cases of pseudo-Hermitian matrices. Matrices satisfying $H = -G^{-1} H^{\dagger} G$ with an additional minus sign (or indeed any phase factor) can be transformed, via $H \to iH$, to also satisfy Eq. (5.1).

Pseudo-Hermiticity breaking occurs when a (degenerate) real eigenvalue splits into a complex conjugate pair on the variation of a parameter, such as the Bloch wave vector for a periodic system. If λ is a complex-valued eigenvalue with associated eigenvector $|R\rangle$ then, by Eq. (5.2), $S|R\rangle^* = S\mathcal{T}|R\rangle$ is an eigenvector of H associated with λ^* and is, thus, linearly independent of $|R\rangle$. Conversely, if λ were real and nondegenerate, then $S\mathcal{T}|R\rangle$ and $|R\rangle$ would be linearly dependent, i.e., $|R\rangle$ would be an eigenvector of $S\mathcal{T}$. In general, eigenvectors of H with real eigenvalues can be chosen to also be eigenvectors of the "symmetry operator" $S\mathcal{T}$. On the variation of a parameter, when a degenerate real eigenvalue splits into complex conjugate pairs, this symmetry of the eigenvectors gets spontaneously broken: $S\mathcal{T}|R\rangle$ and $|R\rangle$ become linearly independent.

While the above formulation in terms of S and $\mathcal{T}$ is familiar [21, 190], in the following we formulate this behavior in terms of G. This will enable us to uncover additional features including the conditions for symmetry breaking to occur.

5.3 STRUCTURE OF THE EIGENSPACE

We denote a column vector by the ket $|v\rangle$ and its conjugate transpose $(|v\rangle)^\dagger$ by the bra $\langle v|$. The right and left eigenvectors of H are defined by $H|R_i\rangle = \lambda_i|R_i\rangle$ and $\langle L_i|H = \lambda_i\langle L_i|$. They share the same eigenvalues. Taking conjugate transpose of the latter equation we get

$$H^\dagger|L_i\rangle = \lambda_i^*|L_i\rangle. \tag{5.3}$$

Operating Eq. (5.1) on $G^{-1}|L_i\rangle$ shows that $G^{-1}|L_i\rangle$ is a (right) eigenvector of H with eigenvalue λ_i^*.

First let us assume that there are no degeneracies in the eigenvalues of H. In that case we can define a biorthonormal eigenbasis for H [21],

$$H = \sum_i \lambda_i|R_i\rangle\langle L_i|, \quad \langle L_i|R_j\rangle = \delta_{ij}. \tag{5.4}$$

Now if $|R_i\rangle$ is the eigenvector of H with $\operatorname{Im}\lambda_i \neq 0$ then the eigenvector corresponding to the eigenvalue $\lambda_j = \lambda_i^*$ is $\eta G^{-1}|L_i\rangle$ where η is some constant. Furthermore,

$$\langle R_j|G|R_j\rangle = \eta\langle R_j|GG^{-1}|L_i\rangle = 0. \tag{5.5}$$

On the other hand if λ_i is real we should have $|R_i\rangle = \mu G^{-1}|L_i\rangle$ (μ being some non-zero constant). In this case,

$$\langle R_i|G|R_i\rangle = \mu\langle R_j|GG^{-1}|L_i\rangle = \mu. \tag{5.6}$$

Since G is invertible and Hermitian, μ has to be a nonzero real constant.

On relaxing our assumption of no degeneracies, these statements generalize as follows (see Appendix C.1 for details):

If λ is complex valued, $\operatorname{Im}\lambda \neq 0$, then $\langle R|G|R\rangle = 0$ for all associated eigenvectors $|R\rangle$.

If λ is real valued, there are three possibilities. If $\langle R|G|R\rangle$ is positive for all vectors, $|R\rangle$, in the eigenspace, we say the eigenvalue λ is of *positive kind* (the first kind in Krein's formulation [28]). Similarly, if $\langle R|G|R\rangle$ is always negative, the eigenvalue λ is of *negative kind.* The third possibility is that one is able to find two eigenvectors, $|R_j\rangle$ and $|R_k\rangle$ in the eigenspace, such that $\langle R_j|G|R_j\rangle$ and $\langle R_k|G|R_k\rangle$ are of opposite signs. In this case the eigenvalue is said to be of *indefinite kind* and it is possible to find an eigenvector $|R_m\rangle$, say, such that $\langle R_m|G|R_m\rangle = 0$. Exceptional point degeneracies are always of indefinite kind while non-degenerate real eigenvalues are never indefinite.

We are now ready to state the main result of the paper, which connects symmetry breaking to the expectation value of the intertwining operator G.

5.4 CONDITIONS FOR SYMMETRY BREAKING

Suppose $G(\boldsymbol{k})$ is a (continuously) parameterized matrix that is Hermitian and invertible for all values of the parameter(s) $\boldsymbol{k}$; and suppose $H(\boldsymbol{k})$ is a (continuously) parameterized pseudo-Hermitian matrix obeying $H(\boldsymbol{k}) = G(\boldsymbol{k})^{-1}H(\boldsymbol{k})^{\dagger}G(\boldsymbol{k})$. Let $\boldsymbol{k} = \boldsymbol{k}_0 + \epsilon\boldsymbol{q}$ where ϵ is small, $\boldsymbol{q}$ is an arbitrary direction in parameter space, and $\boldsymbol{k}_0$ is some reference point such that $H(\boldsymbol{k}_0)$ has all its eigenvalues real.

$H(\boldsymbol{k}_0)$ is said to be protected from pseudo-Hermiticity breaking (strongly stable in Krein's formulation) if for any $\boldsymbol{q}$, $H(\boldsymbol{k} = \boldsymbol{k}_0 + \epsilon\boldsymbol{q})$ also has all real eigenvalues. For example, if $H(\boldsymbol{k}_0)$ has no degeneracies then it is protected from symmetry breaking. The necessary and sufficient conditions for symmetry breaking to occur in a pseudo-Hermitian matrix are provided by the Krein-Gel'fand-Lidskii (KGL) Theorem.

Krein-Gel'fand-Lidskii Theorem. $H(\boldsymbol{k}_0)$ is protected from pseudo-Hermiticity breaking if and only if the eigenvalues of $H(\boldsymbol{k}_0)$ are definite, i.e., $\langle v|G(\boldsymbol{k}_0)|v\rangle \neq 0$ for all eigenvectors $|v\rangle$ of $H(\boldsymbol{k}_0)$. The proof of this statement can be found in Appendix C.2 and in Refs. [28, 164].

In particular, this implies that while an exceptional point at a real eigenvalue is sufficient for symmetry breaking to occur (since $\langle v|G|v\rangle = 0$ at an EP), it is not necessary. (We provide explicit examples of pseudo-Hermitian matrices with symmetry breaking at diabolic points in the sections below.)

Eigenvalues of positive and negative kind retain their kind on the variation of a parameter (see Appendix C.3). This provides predictive power for the purposes of engineering (or avoiding) exceptional points and symmetry-breaking points. For example, suppose that on the variation of a parameter, two definite real eigenvalues are about to meet on the real axis. If the eigenvalues are of the same kind ($\langle v|G|v\rangle$

is of the same sign) then even after colliding they are forbidden from moving off the real axis or giving rise to an exceptional point degeneracy.

The matrix H has as many eigenvalues of positive (negative) kind as the number of positive (negative) eigenvalues of the intertwining operator G (see Appendix C.3). In particular, if G were positive-definite (or negative-definite) then all eigenvalues of H would always be real and all degeneracies diabolic. H would then be equivalent to a Hermitian matrix, a condition known as *exact* pseudo-Hermiticity [203] or quasi-Hermiticity [21].

Suppose an $N \times N$ pseudo-Hermitian matrix, protected from symmetry breaking, has eigenvalues, $\lambda_1 \leq \cdots \leq \lambda_N$. We can characterize it by a signature—an ordered list of N signs, such as $(+,+,-,+,\dots)$, where the nth sign signifies the kind of the nth eigenvalue. Two strongly stable pseudo-Hermitian matrices can be continuously connected to each other, without every encountering pseudo-Hermiticity breaking, if and only if they have the same signature [28]. If G has p positive eigenvalues (and hence $N-p$ negative eigenvalues), then the number of possible distinct signatures is $\frac{N!}{p!(N-p)!}$ (or N choose p). These characterize all the disconnected regions of parameter space where the eigenvalues of a pseudo-Hermitian matrix are all real. In many physical systems these correspond to distinct phases characterized by localization, absence of dissipation, etc. (see **Section 5.8**).

The matrices at the boundaries enclosing these regions protected from symmetry breaking (i.e., at the points at which symmetry breaking occurs) have eigenvalues of indefinite kind. In **Section 5.6** we show that if two strongly stable regions share a point on the boundary, the point is diabolic. All other points on the boundaries are exceptional degeneracies and can be uniquely associated with a single strongly stable region and its signature. It is known that parametrized pseudo-Hermitian matrices have EPs with codimension 1 and DPs with codimension 3 [116, 204, 205]. The large codimensionality of DPs compared to that of EPs explains why symmetry breaking is observed usually at EPs.

It is useful to compare this characterization with the classification of symmetry-protected topological (SPT) phases in non-Hermitian matrices [24, 25, 56, 152] (which generalizes the classification of Hermitian matrices [23]). Matrices belonging to the same symmetry class/phase are topologically equivalent—they are characterized by the same topological invariants and they can be continuously deformed into each other without encountering any degeneracy (the spectral gap is always open). For such a classification all degeneracies are considered equivalent. Here, we are considering properties of the individual eigenspaces of a matrix that too remain invariant unless there are degeneracies and the eigenspaces merge. Moreover, we distinguish between two kinds of degeneracies on physical grounds—stable ones that prohibit symmetry breaking and unstable ones that allow symmetry breaking.

The KGL theorem was originally formulated with the assumption that the intertwining operator G is constant and does not depend on the parameter(s) $\boldsymbol{k}$ [28]. Many systems, especially real-valued systems, however, have intertwining operators that are continuous functions of the parameters. Our proof of the KGL theorem in Appendix C.2 and Appendix C.3 generalizes to the case where $G(\boldsymbol{k})$ is a continuous function of the parameter(s) $\boldsymbol{k}$ as long as it is Hermitian and invertible for all values of $\boldsymbol{k}$.

Since the intertwining operator G is not unique, we provide an exhaustive method to find all intertwining operators for a pseudo-Hermitian matrix H in Appendix C.4 and show that they form a vector space. Our results will apply to each Hermitian intertwining operator that one can find. Finally, since pseudo-Hermiticity is equivalent to commutation with a generalized $\mathcal{PT}$ operator, in Appendix C.5 we provide an attempt to formulate the results of this section in terms of $\mathcal{P}$ and $\mathcal{T}$.

5.5 A SCHEMATIC EXAMPLE

Let us illustrate these results with an example. Suppose H is a 3×3 pseudo-Hermitian matrix with respect to the conveniently diagonalized,

$$G = \begin{pmatrix} 1 & 0 & 0 \\ 0 & 1 & 0 \\ 0 & 0 & -1 \end{pmatrix}. \tag{5.7}$$

The general form of H can be written as,

$$H = \begin{pmatrix} r_1 & a & b \\ a^* & r_2 & c \\ -b^* & -c^* & r_3 \end{pmatrix}, \tag{5.8}$$

where r_i are real numbers and a, b, c are complex numbers. When $a = b = c = 0$, the three eigenvalues are real and located at $\lambda_i = r_i$. The eigenvectors are the permutations of $(1, 0, 0)^T$ and it is straightforward to check that λ_3 is of opposite kind to the other two eigenvalues.

On increasing $|a|$, λ_3 remains fixed while λ_1 and λ_2 move away from each other on the real axis due to level repulsion. (The matrix is Hermitian when $b = c = 0$.) If $|c|$ were increased with $a = b = 0$, then λ_2 and λ_3 move, first towards each other along the real axis and then since they are of opposite kinds, away from each other in the complex plane after colliding. Similarly, if $|b|$ were increased then λ_1 and λ_3 move towards each other.

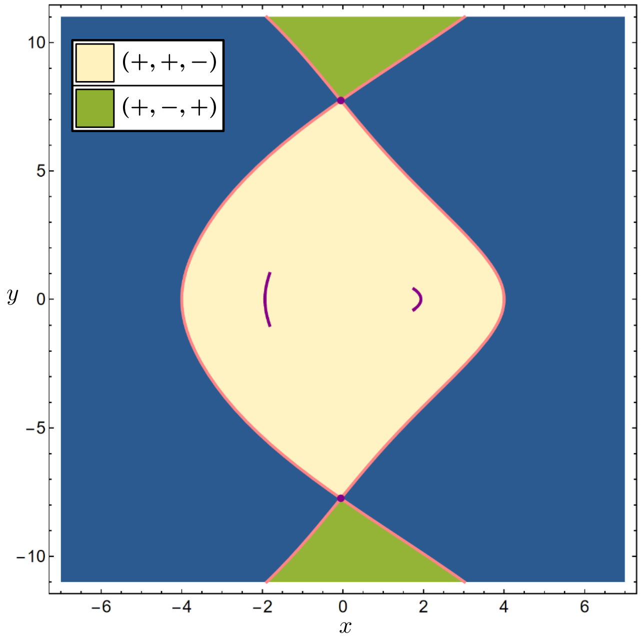

Figure 5.1. Parameter space of the matrix $H(x, y)$ in Eq. (5.9) which obeys $H = G^{-1}H^{\dagger}G$ where $G = \text{diag}(1, 1, -1)$. In the blue region of parameter space, pseudo-Hermiticity is broken and the eigenvalues of H are no longer all real. The yellow region is protected from symmetry breaking and has signature $(+, +, -)$, i.e., the eigenvalue of negative kind is the largest. Similarly, the green region has signature $(+, -, +)$. Regions of different signatures are topologically disconnected. The boundaries between these regions have exceptional point degeneracies (pink curves), except where the curves meet and annihilate to form a diabolic point (purple points). The central region also contains two disconnected diabolic curves (purple curves) involving two eigenvalues of positive kind. Since they are of the same kind these degeneracies cannot lead to symmetry breaking.

Let us constrain H to a two-dimensional parameter space with the parametrization,

$$H(x, y) = \begin{pmatrix} 1 & y & ix \\ y & \frac{3}{2} & \frac{i}{2}\sin(\frac{\pi y}{8}) \\ ix & \frac{i}{2}\sin(\frac{\pi y}{8}) & 9 \end{pmatrix}. \tag{5.9}$$

In Fig. 5.1, we show the parameter space of this matrix. The region around the origin, $(0, 0)$, is protected from symmetry breaking and has the signature $(+, +, -)$. As we move from the origin along the positive x axis, the eigenvalue at $r_2 = \frac{3}{2}$ remains fixed while the other two eigenvalues move towards each other. At $x = \frac{\sqrt{15}}{2} \approx 1.94$ a diabolic degeneracy is encountered but since it involves eigenvalues of the same kind, it cannot give rise to symmetry breaking even in a higher dimensional parameter space. On increasing x further, two eigenvalues of opposite kind meet at an EP at $x = 4$ beyond which pseudo-Hermiticity gets broken.

Figure 5.1 shows that the boundary between symmetry broken regions of the 2D parameter space and regions protected from symmetry breaking are given by exceptional curves. When the exceptional curves meet, they annihilate each other to form diabolic points [205]. These are examples of symmetry breaking at DPs—perturbing the value of x at the DP at $(x, y) \approx (-0.05, 7.75)$, for example, will cause the eigenvalues to become complex valued. While it seems from the figure that the region with signature $(+, -, +)$ consists of disconnected areas, this is just an artifice of being constrained to a two-dimensional parameter space.

5.6 CHARACTERIZING THE POINTS OF SYMMETRY BREAKING

The points of symmetry breaking of an $N \times N$ pseudo-Hermitian matrix form the boundaries separating strongly stable regions of parameter space from the regions where at least one eigenvalue is complex valued. To characterize these points we will only focus on the most relevant case of boundaries formed when two eigenvalues of opposite kind meet each other. (Higher order degeneracies are rare in the absence of additional symmetries.) In the subspace corresponding to these two eigenvalues of opposite kind, a general intertwining operator (after diagonalization) is given by

$$G_0 = \begin{pmatrix} \eta_1 & 0 \\ 0 & -\eta_2 \end{pmatrix} \tag{5.10}$$

where η_1 and η_2 are positive real numbers. The relation $H_0 = G_0^{-1} H_0^\dagger G_0$ eliminates 4 out of 8 real parameters of a generic complex-valued 2×2 matrix. We can parametrize such a pseudo-Hermitian matrix as

$$H_0 = \begin{pmatrix} \lambda + a & \eta_2 b e^{i\theta} \\ -\eta_1 b e^{-i\theta} & \lambda - a \end{pmatrix} \tag{5.11}$$

where a, b, θ, λ are real. Since θ does not enter the characteristic equation and λ only shifts the eigenvalues by the same amount, the physics of a generic 2×2 pseudo-Hermitian matrix is controlled by the gain-loss factor (a) and the coupling factor (b) (see **Section 5.8.1**). The matrix has degenerate eigenvalues (at λ) when we set $b = \frac{a}{\sqrt{\eta_1 \eta_2}}$,

$$H_0 = a \begin{pmatrix} 1 & \sqrt{\frac{\eta_2}{\eta_1}} e^{i\theta} \\ -\sqrt{\frac{\eta_1}{\eta_2}} e^{-i\theta} & -1 \end{pmatrix} + \begin{pmatrix} \lambda & 0 \\ 0 & \lambda \end{pmatrix}. \tag{5.12}$$

The behavior of the degeneracy is controlled by the parameter a — the degeneracy is diabolic when $a = 0$ and is exceptional at all other values.

In Appendix C.6.1, we consider pseudo-Hermitian matrices arbitrarily close to H_0. That is, we consider $G(\epsilon), H(\epsilon)$ such that $H(\epsilon) = G(\epsilon)^{-1} H(\epsilon)^{\dagger} G(\epsilon)$ and $G(0) = G_0, H(0) = H_0$. In the limit of $0 < \epsilon \lll 1$, we find that strongly stable matrices close to H_0 with $a > 0$ can only be from the region $(-, +)$ while those close to H_0 with $a < 0$ can only be from the region $(+, -)$. In contrast, one can always find strongly stable matrices from both the regions $(-, +)$ as well as $(+, -)$ arbitrarily close to H_0 with $a = 0$ (the DP) (see Fig. 5.2).

Thus, the EPs on the boundaries can be identified with the topological index, i.e., the signature, of the strongly stable region they enclose. In fact, EPs can be characterized by several independent topological indices [193]. For example, they can also be characterized by the topological indices associated with symmetry protected exceptional surfaces/rings that arise in systems with chiral symmetry [161, 206]. This relies on the fact that iH has the non-Hermitian chiral symmetry, $(iH)G + G(iH)^{\dagger} = 0$

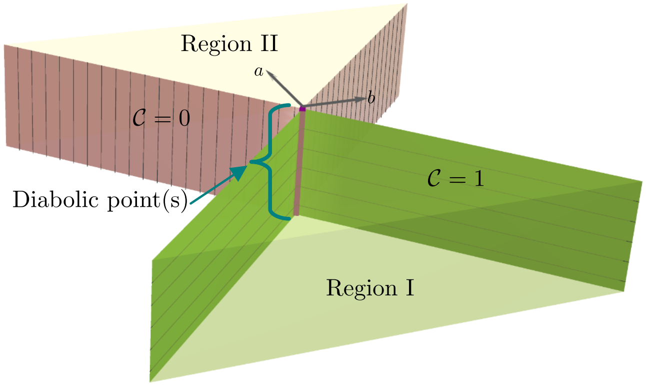

Figure 5.2. Strongly stable regions in parameter space (where all eigenvalues are real) are surrounded by exceptional surfaces that meet and annihilate at diabolic points (purple line). These EPs and DPs together make up all possible points where pseudo-Hermiticity breaking occurs. Two such strongly stable regions with signature $(\ldots,+,-,\ldots)$ and $(\ldots,-,+,\ldots)$ are shown (labelled I and II respectively). The exceptional surfaces (green with horizontal mesh and pink with vertical mesh respectively) can be identified uniquely with the strongly stable region they enclose and the corresponding signature. Their topological charges can also be written in terms of the zeroth Chern number ($\mathcal{C} = 1$ and $\mathcal{C} = 0$ respectively). Pseudo-Hermiticity is broken in the region outside these surfaces. In the neighbourhood of a symmetry-breaking point, the Hamiltonian can be reduced to the two parameter matrix $\begin{pmatrix} a & b \\ -b & -a \end{pmatrix}$ where $a \in \mathbb{R}$ is a gain-loss parameter and $b \in \mathbb{R}$ is a coupling parameter [see Eq. (5.11)].

and thus one can follow the procedure first laid out in Ref. [161]. The relevant topological index is the zeroth Chern number number associated with an extended Hermitian matrix created from H (see Appendix C.6.2). We find that the exceptional line $a > 0$ carries a Chern number of 0 while the line $a < 0$ has Chern number 1 (see Fig. 5.2).

5.7 RELATION WITH SYMMETRIES

Degeneracies in Hamiltonian matrices are either accidental or caused by symmetries. In Hermitian Hamiltonians, the latter case is more common due to level repulsion. It is natural to ask whether degeneracies caused by symmetries are susceptible to pseudo-Hermiticity breaking? Indeed if this were the case we would observe *thresholdless* pseudo-Hermiticity breaking — even a small non-Hermitian perturbation of a spatially symmetric Hermitian Hamiltonian would cause complex-valued eigenvalues (see Ref. [171] and **Section 5.8.2** for examples). We show that the intertwining operator provides the right language to address this question.

We recall that H has a symmetry described by a group $\mathcal{G}$ if H commutes with the matrix representations of the elements of $\mathcal{G}$. We assume that the representations are unitary—a standard assumption in canonical quantum mechanics since it keeps the inner product invariant. Additionally, we recall that any representation η can be generically broken into irreps (irreducible representations), $\eta = \pi_1 \oplus \pi_2 \oplus \dots$, and that the Hamiltonian H becomes degenerate in each subspace on which an irrep acts [207]. This is the reason why symmetries typically give rise to degeneracies unless, for example, the underlying group is Abelian, in which case the irreps are one-dimensional.

Let us start below the threshold for symmetry breaking such that a pseudo-Hermitian matrix H has all real eigenvalues and can be diagonalized. Now on tuning a parameter suppose the spatial symmetry of the Hamiltonian is explicitly broken, which allows for the previously degenerate eigenvalues to move away from each other. Would they stay on the real axis or would they move off in the complex plane?

To answer this question we need to classify the subspace Ω on which an irreducible representation π acts. Before spatial symmetry is explicitly broken, Ω was also one of the degenerate eigenspaces of H. Now, since π is an irrep, for any non-zero vector $|v\rangle \in \Omega$ one can operate the group elements, $\pi(g_i)\pi(g_j)\dots|v\rangle$ to span the whole space Ω. Computing the expectation value of the intertwining operator G for each of these spanning vectors we get terms like

$$\langle v|\dots\pi(g_j)^\dagger\pi(g_i)^\dagger G\pi(g_i)\pi(g_j)\dots|v\rangle. \tag{5.13}$$

The relative sign of these terms capture whether or not we would see thresholdless symmetry breaking. We see that if G were to commute with the elements of $\mathcal{G}$, all these terms would equal $\langle v|G|v\rangle$ implying that the subspace is either of positive or negative kind (as long as $\langle v|G|v\rangle$ is non-zero). The commutation of the intertwining operator, G, with the group elements thus ensures that the degeneracy is stable such that on loss of spatial symmetry even though the degeneracy of eigenvalues is broken, they still stay on the real axis.

We note here that the intertwining operator G has another property associated with symmetries —it provides a conserved quantity for pseudo-Hermitian systems [192]. To show this, we first define the time propagation matrix $U(t) = e^{-iHt}$, which is the solution to the Schrödinger equation, $i\frac{dU}{dt} = HU$. Since H is not Hermitian, $U(t)$ is not unitary; instead it satisfies [165]

$$U^{-1}(t) = G^{-1}U^\dagger(t)G. \tag{5.14}$$

The expectation value of G with respect to a time-evolving vector $|v(t)\rangle = U(t)|v(0)\rangle$ is independent of time.

$$\begin{aligned}\langle v(t)|G|v(t)\rangle &= \langle v(0)|U^\dagger(t)GU(t)|v(0)\rangle \\ &= \langle v(0)|G|v(0)\rangle.\end{aligned} \tag{5.15}$$

$\langle v(t)|G|v(t)\rangle$ is then a conserved quantity of the system [192].

5.8 EXAMPLES

In the following, we provide some examples of physical Hamiltonians exhibiting pseudo-Hermiticity breaking. We study a minimal example of a two-level system from photonics in **Section 5.8.1**, in particular noting the role of the conserved quantity for a system with gain and loss. In **Section 5.8.2**, we study a lattice in which non-Hermiticity arises from asymmetric couplings and show how pseudo-Hermiticity breaking can be analyzed in the submatrices of the Hamiltonian. Finally, in **Section 5.8.3**, we examine coupled dissipative oscillators and find an interplay of two simultaneous intertwining operators.

These examples demonstrate how various physical systems that were previously considered to exhibit unique rich behavior can be analyzed from the unified perspective of pseudo-Hermiticity.

5.8.1 Gain and loss in a qubit

One of the simplest pseudo-Hermitian system is a two-level system describing the physics of two coupled sites, one experiencing gain and the other suffering loss. The Hamiltonian

$$H = \begin{pmatrix} -ig_1 & \kappa \\ \kappa & ig_2 \end{pmatrix}, \tag{5.16}$$

where g_1, g_2 describe the amplification/dissipation at each site and κ is the coupling constant describes such a system. See the review articles Refs. [2, 189] for examples of physical setups described by such a Hamiltonian. When $g_1 = g_2 = g$, the gain and loss are balanced and H becomes pseudo-Hermitian, $H = G^{-1}H^\dagger G$, with

$$G = \begin{pmatrix} 0 & 1 \\ 1 & 0 \end{pmatrix}. \tag{5.17}$$

If $\begin{pmatrix} a(t) \\ b(t) \end{pmatrix} = \begin{pmatrix} |a(t)|e^{i\theta_1(t)} \\ |b(t)|e^{i\theta_2(t)} \end{pmatrix}$ is a solution to the Schrödinger equation, then the conserved quantity is

$$C = \begin{pmatrix} a^* & b^* \end{pmatrix} \begin{pmatrix} 0 & 1 \\ 1 & 0 \end{pmatrix} \begin{pmatrix} a \\ b \end{pmatrix} = 2|a(t)b(t)|\cos(\theta_1(t) - \theta_2(t)). \tag{5.18}$$

Furthermore, G has eigenvalues $+1$ and -1 so the two modes of H are of opposite kinds and we can expect symmetry breaking. (Indeed for a two-level system we either have this case or the trivial case of both modes being of the same kind for which the dynamics is similar to Hermitian dynamics.)

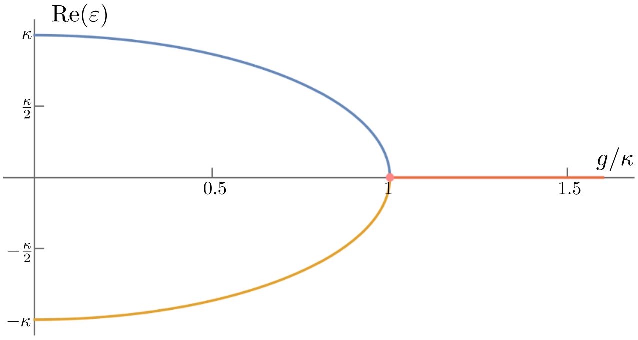

Figure 5.3. Real part of the eigenvalues of $H = \begin{pmatrix} -ig & \kappa \\ \kappa & +ig \end{pmatrix}$ which describes two coupled modes with equal and opposite gain/loss. When $g < \kappa$, the two eigenvalues, which are of opposite kind, are real. They meet each other at an exceptional point when g/κ reaches the threshold value of 1 and on further increasing g/κ, the eigenvalues become complex valued.

The eigenvalues of H are $\pm\sqrt{\kappa^2 - g^2}$. When $\kappa > g$, the coupling dominates the amplification/dissipation, the eigenvalues are real, and pseudo-Hermiticity symmetry is unbroken. Symmetry breaking occurs when g reaches its critical value, $g_c = \kappa$, after which the eigenvalues of H become complex (see Fig. 5.3).

Symmetry unbroken phase ($g < \kappa$). The eigenvalues are real and can be written as $\pm\eta$, where $\eta = \sqrt{\kappa^2 - g^2}$ is real and positive. The eigenvectors are $|v_\pm\rangle = \begin{pmatrix} 1 \\ \pm e^{\pm i\theta} \end{pmatrix}$ where $\theta = \arcsin(g/\kappa)$. We have $\langle v_s|G|v_s\rangle = 2s\cos(\theta)$ so the eigenvalue $+\eta$ is of positive kind while $-\eta$ is of negative kind.

The general solution to the Schrödinger equation is

$$|v(t)\rangle = \begin{pmatrix} c_1\cos(\theta - \eta t) + ic_2\sin(\eta t) \\ c_2\cos(\theta + \eta t) + ic_1\sin(\eta t) \end{pmatrix} \tag{5.19}$$

where c_1, c_2 specify the initial conditions. If we start with a $\frac{\pi}{2}$ phase shift, $c_1 = e^{i\alpha}|c_1|, c_2 = ie^{i\alpha}|c_2|$, then the two sites remain phase locked due to the conservation of $\langle v|G|v\rangle$.

Symmetry broken phase ($g > \kappa$). The eigenvalues are now complex conjugates and can be written as $\pm i\mu$, where $\mu = \sqrt{g^2 - \kappa^2}$ is real and positive. The eigenvectors of H are $|v_\pm\rangle = \begin{pmatrix} \kappa \\ i(g \pm \mu) \end{pmatrix}$ and $\langle v_s|G|v_s\rangle = 0$.

The general solution to the Schrödinger equation is

$$|v(t)\rangle = \begin{pmatrix} c_1\kappa e^{\mu t} + c_2\kappa e^{-\mu t} \\ ic_1(g + \mu)e^{\mu t} + ic_2(g - \mu)e^{-\mu t} \end{pmatrix}. \tag{5.20}$$

For nonzero c_1, since the amplitudes of both the sites increase exponentially for large t, asymptotically the sites develop a phase difference of $\frac{\pi}{2}$. Again this is predicted directly from the conservation of $\langle v|G|v\rangle$ since as $|v_1v_2|$ increases, $\cos(\theta_1 - \theta_2)$ should diminish.

Symmetry breaking point ($g = \kappa$). At exactly $g = \kappa$, the system exhibits an exceptional point. The eigenvalues equal zero, and the eigenvectors coalesce to a single eigenvector, $|v\rangle = \begin{pmatrix} 1 \\ i \end{pmatrix}$ with $\langle v|G|v\rangle = 0$ as expected from an exceptional point.

While this two-level Hamiltonian is well known, the fact that it has a conserved quantity, which leads to a $\frac{\pi}{2}$ phase-locking, was never noted. Furthermore, the physics of many finite-dimensional systems experiencing gain and loss cannot be captured in terms of effective two-level Hamiltonians [208, 209]. These systems exhibit richer behavior with phase diagrams of pseudo-Hermiticity broken regions separated by exceptional lines and higher order exceptional points [208, 209]. For these systems exact solutions are difficult, and using the intertwining operator to predict the phase diagram and the stability of degeneracies may be the only tractable method to lead to any physical insights.

5.8.2 Lattice with asymmetric hopping

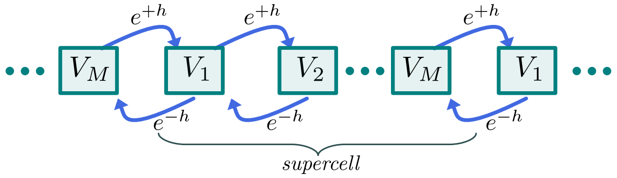

Figure 5.4. A lattice with asymmetric hopping described by the Hamiltonian in Eq. (5.21). Each supercell consists of M sites with onsite potential V_α. The particle hops to the site on its right with amplitude e^{+h} and to the site on its left with amplitude e^{-h}.

We consider a one-dimensional real lattice of N supercells, each with M sites, connected by nearest-neighbor coupling (see Fig. 5.4). The Hamiltonian is [77]

$$H = \sum_{n=1}^{N} H_n \tag{5.21}$$

where,

$$\begin{aligned} H_n = &\sum_{\alpha=1}^{M} V_\alpha |n,\alpha\rangle\langle n,\alpha| \\ &+ \sum_{\alpha=1}^{M-1} \left(e^{-h}|n,\alpha\rangle\langle n,\alpha+1| + e^{h}|n,\alpha+1\rangle\langle n,\alpha|\right) \\ &+ e^{-h}|n,M\rangle\langle n+1,1| + e^{h}|n+1,1\rangle\langle n,M|. \end{aligned} \tag{5.22}$$

Here, V_α is the potential energy at each site, e^h is the amplitude for the particle to hop rightwards, and e^{-h} the amplitude to hop leftwards. Periodic boundary conditions are assumed.

Such a Hamiltonian has been used to model vortex lines in type II superconductors [15] (where $h > 0$ signifies a transverse component of the applied magnetic field), polymers chains on periodic substrates [42] (where $h > 0$ signifies an externally applied shear force), and a variety of other physical systems [51, 210]. The source of non-Hermiticity in these models is asymmetric coupling instead of gain/loss as in the previous example.

In the Hermitian limit, $h \to 0$, the eigenvalues of H are real and form M bands. As h increases, it is known that the bands expand into ovals in the complex plane [see Fig. 5.5**a**] [42, 77]. As the bands expand, two bands may meet each other at a critical value of h closing the bandgap and leading to an insulator-conductor transition. This corresponds to a localization-delocalization transition in the physical system [15, 42, 51] and we show below that such a transition is equivalent to pseudo-Hermiticity breaking.

Due to the discrete translation symmetry of the lattice, H can be block diagonalized as $H = \oplus_k \mathcal{H}(k)$ where

$$\begin{aligned}\mathcal{H}(k) = &\sum_{\alpha=1}^{M} V_\alpha |k,\alpha\rangle\langle k,\alpha| \\ &+ \sum_{\alpha=1}^{M-1} \left(e^{-h}|k,\alpha\rangle\langle k,\alpha+1| + e^{h}|k,\alpha+1\rangle\langle k,\alpha|\right) \\ &+ e^{-h-ik}|k,M\rangle\langle k,1| + e^{h+ik}|k,1\rangle\langle k,M|, \end{aligned} \tag{5.23}$$

and $k = \frac{\pi m}{N}$ with $m \in \{-N+2, -N+4, \ldots, N-2, N\}$. In matrix form this is (where blanks denote zeros)

$$\mathcal{H}(k) = \begin{pmatrix} V_1 & e^{-h} & & & & e^{h+ik} \\ e^{h} & V_2 & e^{-h} & & & \\ & e^{h} & V_3 & e^{-h} & & \\ & & \ddots & \ddots & \ddots & \\ & & & e^{h} & V_{M-1} & e^{-h} \\ e^{-h-ik} & & & & e^{h} & V_M \end{pmatrix}. \tag{5.24}$$

The eigenvalues $\varepsilon(k)$ of $\mathcal{H}(k)$ correspond to the projections of the M Bloch bands at wave-vector k. We will assume that the potential is inversion symmetric, such that $V_1 = V_M, V_2 = V_{M-1,\ldots}$, which will simplify the form of the intertwining operator, and restrict ourselves to a lattice that is a band insulator at $h \to 0$ (all bands are separated). For concreteness we will also assume that M is an odd number.

We note that $\mathcal{H}(k) = \mathcal{H}(-k)^*$ (due to the lattice being real valued) and $\mathcal{H}(k) = G^{-1}\mathcal{H}(k)^T G$ (due to the left-right symmetry of the lattice). Here, G is an $M \times M$

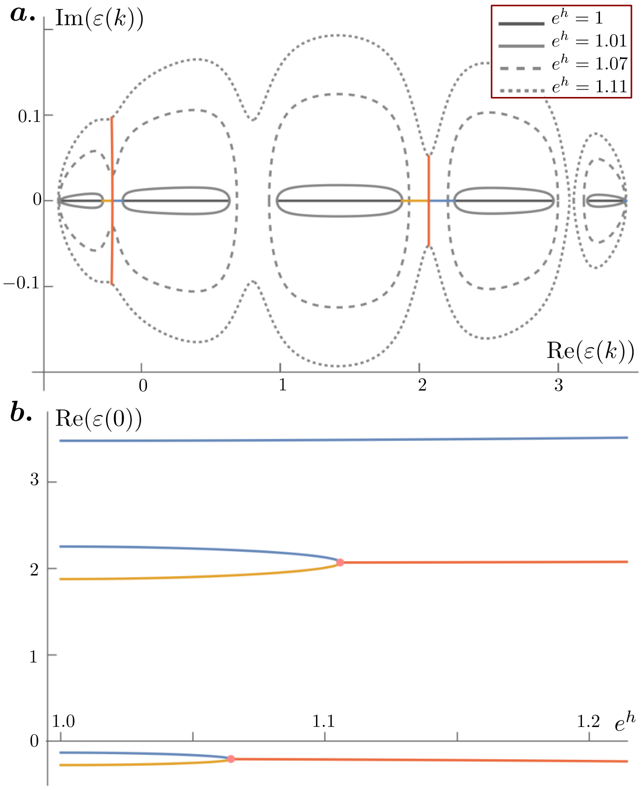

Figure 5.5. **a** The eigenvalues of the Hamiltonian in Eq. (5.21) form M separate oval-shaped bands in the complex plane. Here, we have set $M = 5$ and $V_1 = V_5 = 1.4, V_2 = V_3 = 1.2, V_3 = 2$. At $h = 0$ ($e^h = 1$), the Hamiltonian is Hermitian and the ovals collapse to line segments on the real axis [dark gray continuous lines in **a**]. As the non-Hermiticity factor h increases, the ovals grow in size and merge with each other (we show the bands at $e^h = 1.01, 1.07, 1.11$). The eigenvalues associated with $k \neq 0, \pi$ move off the real axis at arbitrarily small h while those with $k = 0$ or $k = \pi$ move along the real axis until a degeneracy of indefinite kind is formed. The trajectories of the eigenvalues of $\mathcal{H}(0)$ [Eq. (5.24)] on increasing h are depicted by the continuous curves (real eigenvalues of positive and negative kind are shown in blue and yellow respectively, complex-valued eigenvalues are shown in red). These are also shown in **b** where the attraction between eigenvalues of opposite kinds is more apparent. The two symmetry-breaking points shown in pink are both exceptional degeneracies.

antidiagonal matrix with each entry on the antidiagonal being 1, i.e.,

$$G = \begin{pmatrix} 0 & 0 & \dots & 0 & 1 \\ 0 & 0 & \dots & 1 & 0 \\ \vdots & \vdots & \iddots & \vdots & \vdots \\ 0 & 1 & \dots & 0 & 0 \\ 1 & 0 & \dots & 0 & 0 \end{pmatrix}. \tag{5.25}$$

G has $+1$ as an eigenvalue, repeated $\frac{M+1}{2}$ times, with any symmetric vector, $\{a_1, a_2, \dots, a_2, a_1\}^T$ as an eigenvector. The other eigenvalue is -1, repeated $\frac{M-1}{2}$ times, with antisymmetric vectors, $\{a_1, a_2, \dots, a_{\frac{M-1}{2}}, 0, -a_{\frac{M-1}{2}}, \dots, -a_2, -a_1\}^T$ spanning the eigenspace. We use the pseudo-Hermiticity structure arising from these two symmetries to explain the key characteristics of this system.

The swelling of bands into ovals is captured by the matrix $\mathcal{H}(+k) \oplus \mathcal{H}(-k)$ where k is neither 0 nor π. For these matrices, one can show that $\tilde{G}[\mathcal{H}(+k) \oplus \mathcal{H}(-k)] = [\mathcal{H}(+k) \oplus \mathcal{H}(-k)]^\dagger \tilde{G}$ where $\tilde{G}$ is a $2M \times 2M$ antidiagonal matrix with each entry on the antidiagonal being 1. That is,

$$\begin{pmatrix} 0 & G \\ G & 0 \end{pmatrix} \begin{pmatrix} \mathcal{H}(+k) & 0 \\ 0 & \mathcal{H}(-k) \end{pmatrix} = \begin{pmatrix} \mathcal{H}(+k) & 0 \\ 0 & \mathcal{H}(-k) \end{pmatrix}^\dagger \begin{pmatrix} 0 & G \\ G & 0 \end{pmatrix}. \tag{5.26}$$

$\tilde{G}$ has $+1$ as an M-fold eigenvalue and -1 as the other M-fold eigenvalue.

In the Hermitian limit, $h \to 0$, the eigenvalues of $\mathcal{H}(k)$ are real for all values of k. The time-reversal symmetry, $\mathcal{H}(+k) = \mathcal{H}(-k)^*$, implies (by Kramers' theorem [152]) that the eigenvalues of $\mathcal{H}(+k) \oplus \mathcal{H}(-k)$ come in degenerate pairs. At nonzero h, Kramers' degeneracy theorem breaks down [211] and we may expect a case of *threshold-less* symmetry breaking [171] as in **Section 5.7** if the degenerate eigenvalues were of opposite kind.

Returning to the Hermitian limit, suppose $|v_i(+k)\rangle$ and $|v_i(-k)\rangle$ are the eigenvectors of $\mathcal{H}(+k)$ and $\mathcal{H}(-k)$, respectively, for a common eigenvalue λ_i. The superposition $\alpha|v_i(+k)\rangle + \beta|v_i(-k)\rangle$ is then the general eigenvector of $[\mathcal{H}(+k) \oplus \mathcal{H}(-k)]$ corresponding to λ_i. One can check that the eigenvector with $(\alpha, \beta) = (1, 1)$ is of opposite kind to the one with $(\alpha, \beta) = (1, -1)$. Thus, all the degeneracies of $[\mathcal{H}(+k) \oplus \mathcal{H}(-k)]$ are of indefinite kind at $h \to 0$ enabling the eigenvalues to move off the real axis when non-Hermiticity is introduced at arbitrarily small h leading to the swelling of bands into ovals [see Fig. 5.5**a**].

Now, for $k = 0, \pi$, we get $\mathcal{H}(0) = G^{-1}\mathcal{H}(0)^\dagger G$ and $\mathcal{H}(\pi) = G^{-1}\mathcal{H}(\pi)^\dagger G$. Thus, these two matrices have $\frac{M+1}{2}$ eigenvalues of positive kind and the rest of negative kind. In the Hermitian limit, $h \to 0$, the eigenvalues are all real and since $\mathcal{H}(0)$ [as well as $\mathcal{H}(\pi)$] commutes with G, its eigenvectors are either symmetric vectors (and of positive kind), or antisymmetric vectors (and of negative kind). Upon turning on the bias, by increasing the value of h, while the eigenvectors are no longer constrained to be either symmetric or anti-symmetric, the eigenvalues remain restricted to the real axis in the absence of degeneracies. Numerical investigations suggest that on increasing h, the eigenvalues of opposite kinds attract each other and when they meet, and two bands merge at $k = 0$, they generically produce exceptional point degeneracies [see Fig. 5.5**b** where we show the eigenvalues of $\mathcal{H}(0)$].

Whether or not the bands have merged is then captured by whether or not pseudo-Hermiticity breaking has occurred in the matrix $\mathcal{H}(0) \oplus \mathcal{H}(\pi)$. When the symmetry breaking does occur, it leads to a localization to delocalization transition (or insulator to metal transition) in the physical system.

In summary, we showed that the two key characteristics of a lattice with asymmetric coupling—namely, the swelling of bands into ovals at infinitesimal asymmetry and the localization-delocalization transition at a critical value of asymmetry—are captured by pseudo-Hermiticity breaking in the relevant submatrices of the system. We expect these key insights to be valuable in the study of higher dimensional systems [81], dimerized systems, and systems with disorder [77].

5.8.3 Coupled dissipative oscillators

Harmonic oscillators are ubiquitous in classical physics since they model small fluctuations of a many-body system about its equilibrium configuration. In recent years, a detailed study of the matrix structure of mechanical oscillators revealed rich behavior such as internal symmetries [18], topologically protected boundary modes [17], exceptional rings [161], etc. Here we consider a system of identical masses subject to an arbitrary harmonic potential and show that the system exhibits two intertwining operators that govern the behavior of the modes.

Consider n coupled classical mechanical oscillators with equal masses (set to 1). We denote the positions of the oscillators by $\vec{x} = \{x_1, x_2, \ldots, x_n\}^T$ such that the potential energy of the system is $\vec{x}^T.K.\vec{x}$ where K is the stiffness matrix. K is real and symmetric with real eigenvalues Ω_i^2, and corresponding eigenvectors $\vec{q}_i$ satisfying

$$K\vec{q}_i = \Omega_i^2 \vec{q}_i. \tag{5.27}$$

We are interested in the first-order equation

$$i\frac{d}{dt}\begin{pmatrix} \vec{x}(t) \\ \vec{p}(t) \end{pmatrix} = -i\begin{pmatrix} 0 & -\mathbb{I}_n \\ K & \gamma\mathbb{I}_n \end{pmatrix}\begin{pmatrix} \vec{x}(t) \\ \vec{p}(t) \end{pmatrix}, \tag{5.28}$$

where γ is the viscous damping coefficient. The equation above also defines the quantum Hamiltonian

$$H = -i\begin{pmatrix} 0 & -\mathbb{I}_n \\ K & \gamma\mathbb{I}_n \end{pmatrix}. \tag{5.29}$$

Since the Hamiltonian is time-independent the equation can be solved by substituting $\begin{pmatrix} \vec{x}(t) \\ \vec{p}(t) \end{pmatrix} = e^{-i\omega t}|v\rangle$, where $|v\rangle$ is a time-independent column vector, to get

$$\omega|v\rangle = -i \begin{pmatrix} 0 & -\mathbb{I}_n \\ K & \gamma\mathbb{I}_n \end{pmatrix} |v\rangle, \tag{5.30}$$

an eigenvalue equation. The eigenvectors are

$$|v_i^{\pm}\rangle = \begin{pmatrix} \vec{q}_i \\ -i\omega_i^{\pm}\vec{q}_i \end{pmatrix} \tag{5.31}$$

with eigenvalues

$$\omega_i^{\pm} = -\frac{i\gamma}{2} \pm \frac{\sqrt{4\Omega_i^2 - \gamma^2}}{2}. \tag{5.32}$$

We first consider the case of no dissipation, $\gamma = 0$, such that the eigenvalues are guaranteed to be real, $\omega_i^{\pm} = \pm\Omega_i$. The pseudo-Hermitian symmetries of $H(\gamma = 0)$ are as following.

First, since this is a classical mechanical system the underlying matrix is real-valued. By our choice of notation this implies $H(\gamma = 0)^* = -H(\gamma = 0)$ such that its eigenvalues are either purely imaginary or come in pairs with oppositely signed real parts. Recalling that such a condition is equivalent to (anti-)pseudo-Hermiticity we find that we can write this as $G_1' H = -H^\dagger G_1'$, where

$$G_1' = \begin{pmatrix} -\tau K & \mathbb{I}_n \\ \mathbb{I}_n & \tau\mathbb{I}_n \end{pmatrix} \tag{5.33}$$

is Hermitian and invertible. Here, τ is an arbitrary real number.

Second, $H(\gamma = 0)$ is also pseudo-Hermitian, $G_2 H(\gamma = 0) G_2^{-1} = H(\gamma = 0)^\dagger$ with

$$G_2 = iJ = i \begin{pmatrix} 0 & \mathbb{I}_n \\ -\mathbb{I}_n & 0 \end{pmatrix}, \tag{5.34}$$

which is Hermitian as well as unitary. This additional pseudo-Hermiticity comes from the equations of motion being derived from Hamilton's equations of motion [196] (J is the symplectic form). Pseudo-Hermiticity implies that eigenvalues are either real or come in complex conjugate pairs.

Taking the two symmetries together, $H(\gamma = 0)$ either has pairs of oppositely signed eigenvalues that are purely real or purely imaginary, or it has quadruplets of eigenvalues with nonzero real as well as imaginary parts forming the set, $\{\lambda, -\lambda, \lambda^*, -\lambda^*\}$. These symmetries were noted in Ref. [18] where they were connected to the time-reversal symmetry and the chiral symmetry respectively.

With dissipation present, it is useful to work with the traceless matrix,

$$\tilde{H} = H + \frac{i\gamma}{2}\mathbb{I}_{2n} = -i \begin{pmatrix} -\frac{\gamma}{2}\mathbb{I}_n & -\mathbb{I}_n \\ K & \frac{\gamma}{2}\mathbb{I}_n \end{pmatrix}, \tag{5.35}$$

which has the same eigenvectors as in Eq. (5.31) but eigenvalues shifted to $\tilde{\omega}_i^{\pm} = \pm\frac{\sqrt{4\Omega_i^2-\gamma^2}}{2}$. Essentially we have separated away the term governing the total loss of energy of the system and are now working with a matrix with balanced gain and loss. The symmetry due to iH being real generalizes to $G_1\tilde{H} = -\tilde{H}^\dagger G_1$ with

$$G_1 = \begin{pmatrix} \gamma\mathbb{I}_n - \tau K & \mathbb{I}_n \\ \mathbb{I}_n & \tau\mathbb{I}_n \end{pmatrix}. \tag{5.36}$$

G_1 is invertible as long as $\omega_i^{\pm}\tau \neq -i$ for any $\omega_i^{\pm}$. Since G_1 depends explicitly on the parameters of the system, its usefulness is limited as its number of positive and negative eigenvalues change whenever it passes through a noninvertible point. The other symmetry remains the same, $G_2\tilde{H}G_2^{-1} = \tilde{H}^\dagger$ with G_2 as in Eq. (5.34) [161].

Since we have two independent intertwining operators (or indeed a continuous family of intertwining operators), symmetry breaking can only occur when the modes meeting each other are of opposite kind with respect to *all* intertwining operators.

To find the kind of each eigenspace, first let us compute

$$\langle v_i^{\pm}|G_2|v_i^{\pm}\rangle = \begin{pmatrix} \vec{q}_i^* & +i\omega_i^{\pm *}\vec{q}_i^* \end{pmatrix} G_2 \begin{pmatrix} \vec{q}_i \\ -i\omega_i^{\pm}\vec{q}_i \end{pmatrix} = 2|\vec{q}_i|^2 \operatorname{Re}\omega_i^{\pm}. \tag{5.37}$$

This evaluates to 0 for the overdamped case, $4\Omega_i^2 \le \gamma^2$. For the underdamped case, $4\Omega_i^2 > \gamma^2$, we see that $\langle v_i^{+}|G_2|v_i^{+}\rangle$ is of positive kind while $\langle v_i^{-}|G_2|v_i^{-}\rangle$ is of negative kind. Physically, the modes are distinguished by whether the momenta are lagging behind the positions or are ahead of them.

Meanwhile,

$$\begin{aligned}\langle v_i^{\pm}|G_1|v_i^{\pm}\rangle &= \begin{pmatrix} \vec{q}_i^* & +i\omega_i^{\pm *}\vec{q}_i^* \end{pmatrix} G_1 \begin{pmatrix} \vec{q}_i \\ -i\omega_i^{\pm}\vec{q}_i \end{pmatrix} \\ &= \left(|\omega_i^{\pm}|^2\tau - \Omega_i^2\tau + 2\operatorname{Im}\omega_i^{\pm} + \gamma\right)|\vec{q}_i|^2. \end{aligned} \tag{5.38}$$

For the underdamped case, $4\Omega_i^2 > \gamma^2$, this evaluates to 0. For the overdamped case, $4\Omega_i^2 \le \gamma^2$, it evaluates to

$$\langle v_i^{\pm}|G_1|v_i^{\pm}\rangle = \left(\frac{\gamma^2 - 4\Omega_i^2}{2} \pm \frac{\sqrt{\gamma^2 - 4\Omega_i^2}}{2}(2-\gamma\tau)\right)|\vec{q}_i|^2. \tag{5.39}$$

To yield the strongest conditions we choose $\tau = 2/\gamma$ such that both the modes are of positive kind as long as $4\Omega_i^2 < \gamma^2$.

Let us see what the combination of symmetries implies. If we start from $\gamma = 0$ (when $\omega_i^{\pm} = \pm\Omega_i$), the conditions due to G_1 yield that all modes are of indefinite kind and are not very useful. G_2, on the other hand, shows that that the positive and negative frequencies are of opposite kind. They can become complex valued only if they meet at zero modes. Indeed these zero modes (or floppy modes) govern the instability of mechanical systems [17]. These modes have been a subject of interest since for certain lattices they arise from a topological origin and are localized at the boundary and insensitive to local perturbations [17].

On increasing γ, eigenvalues of opposite kind (opposite according to G_2) meet each other if $\Omega_i = \gamma/2$, a condition known as critical damping. The exact solution for the eigenvalues in Eq. (5.32) shows that this pseudo-Hermiticity breaking occurs at an exceptional point. For mechanical lattices, these exceptional points can form exceptional rings due to rotational symmetry [161]. On increasing γ further, the eigenvalues are now of positive kind with respect to G_1 and thus cannot wander freely in the complex plane, i.e., $\omega_i^{\pm} + i\frac{\gamma}{2}$ is constrained to be on the imaginary axis.

In summary, many properties of coupled oscillators are captured by pseudo-Hermiticity and these ideas may be useful in lattices and time-dependent systems and even nonlinear systems [212] where exact solutions are intractable.

5.9 CONCLUSIONS AND DISCUSSION

In summary, we showed that each eigenvalue/eigenspace of a pseudo-Hermitian matrix, H such that $H = G^{-1}H^{\dagger}G$, can be classified into three kinds according to the sign of $\langle v|G|v\rangle$: positive, negative, or indefinite. Real nondegenerate eigenvalues of a parametrized matrix $H(x)$ are either of positive kind or of negative kind, and as they wander along the real axis, on the variation of the parameter, x, these eigenvalues can turn into exceptional point degeneracies and/or split into complex conjugate pairs if and only if they meet a real eigenvalue of opposite kind. This then enables one to predict the occurrence of exceptional points and points of pseudo-Hermiticity breaking.

On the basis of this classification, we also showed that the parameter space of a pseudo-Hermitian matrix exhibits topologically disconnected regions where all the eigenvalues of the matrix are real — which in many cases correspond to distinct stable phases in physical systems. These regions are surrounded by exceptional surfaces which comprise all possible real-valued EPs of pseudo-Hermitian matrices. Exceptional surfaces that are boundaries to two different regions may meet annihilating each other and giving rise to DPs. These exceptional surfaces together with the DPs created by their intersections comprise all points of pseudo-Hermiticity breaking.

We also showed how the intertwining operator, G, gives rise to a conserved quantity and derived the conditions for when degeneracies caused by external symmetries are susceptible to thresholdless pseudo-Hermiticity breaking. We illustrated our results with examples from different branches of physics.

The topological ideas in this paper contribute to the broader study of non-Hermitian topological phenomena such as symmetry-protected topological phases, nodal phases [213, 214], the graph topology of spectra [215], etc. It would be interesting to investigate if the results of this paper can be generalized and applied to other symmetry classes of non-Hermitian matrices. A comprehensive study of the interplay of external symmetries and pseudo-Hermiticity, and the application of this work to the study of random non-Hermitian matrices [216, 217] and to time-dependent systems [197] are all interesting directions. Investigating the response strength of DPs and EPs at pseudo-Hermiticity breaking points is also an interesting direction [158]. We leave these questions to future work.

APPENDIX A

APPENDICES TO **Chapter II** ON SHEARING POLYMERS

A.1 Simulation methods

We implemented Langevin dynamics simulations of discretized polymer chains using a modified version of the open-source simulation software `HOOMD-Blue` [85], with modifications made to enable the addition of periodic potentials of arbitrary phase. Each polymer is approximated as a chain of 200 particles of mass m, connected by stiff harmonic springs with equilibrium length l_0, implemented as a bond potential $V_{\text{bond}}(r) = K(r-l_0)^2/2$ where r is the distance between adjacent particles on the chain and K is a stiffness constant. The noncrossing constraint is enforced by adding a stiff contact interaction between all pairs of particles in the system, with pair potential $V_{\text{contact}}(r) = K(r - l_0)^2$ for separations $r < l_0$. For simplicity, the same stiffness coefficient is used for both potentials.

The tension is implemented by applying the requisite forces on the first and last particles of each polymer chain in the desired shear angle relative to the vertical direction. To prevent the finite-length chains from drifting vertically, the first particle of each chain is confined to a τ coordinate of zero with a deep and narrow harmonic potential well; the well does not constrain the horizontal motion of the particles. The substrate potential energy per unit length of the chain, $V(x) = V_0 \cos(2\pi x/a)$, is implemented by adding a position-dependent potential energy of magnitude $l_0 V(x)$ to each particle.

In all our simulations, we set $m = 1$ and $a = 1$ to set the mass and length scales. The time scale is implicitly defined by setting $K = 10000$ in simulation units for the bond and contact stiffnesses across all simulations. We also set $l_0 = 0.2$, so chains with 200 particles have an equilibrium length of $40a$. The simulation box has periodic boundary conditions along the x direction with dimension $L_x = 10a$ (ten repetitions of the periodic potential) and the system size in the τ direction is set to be much larger than the chain length.

The equilibrium behavior of the system is simulated by using the built-in Langevin integrator of HOOMD-Blue, which introduces random forces on each particle that replicate the effect of a finite temperature T. Langevin dynamics requires the introduction of drag forces on each particle, $\mathbf{F}_{\mathrm{drag},i} = -\gamma \mathbf{v}_i$ proportional to the instantaneous velocity $\mathbf{v}_i$ of the ith particle. The value of the drag coefficient affects the transient dynamics as equilibrium is approached, but is not expected to affect the equilibrium properties. We choose a drag coefficient $\gamma = 0.5$ for our simulations. The time step is chosen to be 0.001 in simulation units. All simulations are run for $H = 10^7$ time steps or more. To aid the evolution to equilibrium conformations, the system is "annealed" by starting the simulation at a temperature of $1.5T$ and ramping the temperature down to the desired value T over the first $H/2$ time steps. Equilibrium density profiles are then built up by sampling particle positions during the latter $H/2$ time steps in intervals of 10^4 time steps.

Disorder in the substrate potential is implemented by adding n_{d} cosine potentials with random amplitudes α_i, wave numbers p_i, and phases ϕ_i to $V(x)$:

$$V_{\mathrm{disorder}}(x) = \sum_{i=1}^{n_{\mathrm{d}}} \alpha_i \cos\left(\frac{2\pi p_i}{L_x} x + \phi_i\right),$$

where α_i are drawn from a uniform distribution chosen to generate the desired RMS amplitude σ_{d}, ϕ_i are drawn uniformly from the interval $[0, 2\pi)$, and p_i are drawn uniformly from the range $2 \le p_i \le 20$.

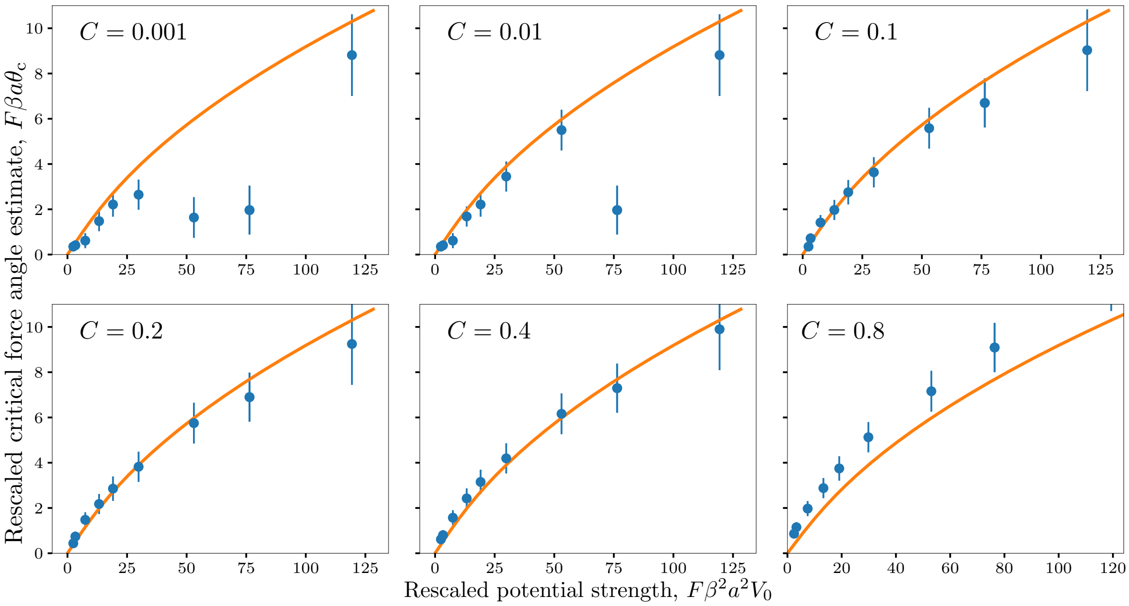

Figure A.1. Critical force angle θ_c estimated as the intersection of the ϕ-θ curve with the line $\phi = c\theta$, for different values of the numerical coefficient c. Estimates from simulated curves (symbols) are compared to the theoretical prediction (solid line) after rescaling as in Fig. 2.4. Data shown are from the sweep with $V_0 = 0.239$ and varying β.

A.2 Extracting critical force angle from simulation data

According to our theoretical analysis, in the limit of infinitely long polymers at commensurate filling the ϕ-θ curve should be exactly zero up to the critical value θ_c, then increase with a diverging slope (as $(\theta - \theta_c)^{1/2}$) before approaching the $\phi = \theta$ line. In our finite-sized molecular dynamics simulations, the polymers acquire a slight tilt at low force angles, which abruptly increases at a finite θ value (see solid curve in Fig. 2.2**g** for the typical behavior). The small nonzero tilt at low θ arises due to bending confined to the polymer ends, whereas the steep rise (signaled by a sudden increase in the slope of the *phi*-θ relationship) is interpreted as a finite-size signature of the sharp delocalization transition in the thermodynamic limit.

To automate the estimation of the critical delocalization angle from simulations, we need a criterion to identify the abrupt rise in the polymer tilt angle curve. One option would be to set a threshold value of ϕ and identify θ_c as the first θ value at which the measured tilt angle is above this threshold. However, the magnitude of the tilt at low θ values depends on the system parameters such as the polymer length and potential strength, so any such threshold ϕ value would have to be adjusted for each simulation to accurately capture the sharp increase. Furthermore, such a criterion would not incorporate the information also present in the changing slope of the ϕ-θ curve. Another possible approach would be to directly estimate the slope of the measured ϕ-θ curve and apply a threshold value to the slope, but this approach is limited in precision by the large spacing between simulated θ values (restricted by the computational resources available).

Rather than imposing a threshold on the value of ϕ or the slope of the ϕ-θ curve, we found that the sudden increase in tilt was reliably captured by searching for the first point of intersection between the ϕ-θ curve and the line $\phi = C\theta$, where

$C < 1$ is a numerical prefactor. If C is set to be large enough, the intersection point avoids the range of slow increase in tilt at low θ, and correctly captures the abrupt increase in slope near the purported critical force angle. The expected large-angle behavior meanwhile restricts C to be smaller than one. If our estimation is robust, we would expect to find an intermediate range of C values for which the intersection, and therefore the θ_{c} estimate, does not significantly change with C because the two curves cross within the region of steep increase in ϕ with θ. We indeed find that our criterion generates θ_{c} estimates that do not change significantly in the range $0.1 \lesssim C \lesssim 0.4$ (Fig. A.1). When C is much smaller than 0.1, the point of intersection falls within the region of shallow slope in the ϕ-θ for some parameter values and the resulting estimate varies strongly with C. At C values larger than 0.4, the point of intersection falls far to the right of the region of steep increase, leading to a systematic overestimate of the critical angle. These patterns are apparent in the variations in estimated θ_{c} as the value of C is changed in Fig. A.1. We use the finite spacing of the simulated θ values to quantify the uncertainty in this estimate.

In the main text, we use the curve-line intersection criterion with $C = 0.1$ (the smallest value which reliably captures the abrupt increase in ϕ across all simulations) to extract critical angle estimates for comparison with the theoretical results in Fig. 2.4. However, our conclusions would be unchanged if we used other values of C within the range $0.1 \lesssim C \lesssim 0.4$, as the estimates would still agree with the theoretical prediction within the uncertainty, as shown in Fig. A.1. Note that there are no fitting parameters; the theory curve is completely determined by the system parameters.

A.3 Deriving the diffusion equation

To obtain the differential equation whose solution provides the partition function in Eq. (2.2), we consider the evolution of Ψ for a small change in the τ coordinate, $\tau \to \tau+\epsilon$. Since the energy of the polymer is built up of purely local terms, $E[x;0,\tau+\epsilon] = E[x;0,\tau] + E[x;\tau,\tau+\epsilon]$ for any ϵ. As a result, Ψ obeys the useful 'Markovian' recursive relation [33],

$$\Psi(x_\tau, x_0, \tau+\epsilon) \sim \int dx_\epsilon \Psi(x_\tau, x_\tau + x_\epsilon, \epsilon)\Psi(x_\tau + x_\epsilon, x_0, \tau). \tag{A.1}$$

The partition function can now be evaluated iteratively [33]. For small ϵ we can expand the left hand side as $\Psi(x_\tau, x_0, \tau) + \epsilon\partial_\tau\Psi(x_\tau, x_0, \tau) + \mathcal{O}(\epsilon^2)$. We also perform the expansion,

$$\Psi(x_\tau + x_\epsilon, x_0, \tau) \approx \left(1 + x_\epsilon\partial_x + \frac{x_\epsilon^2}{2}\partial_x^2\right)\Psi(x_\tau, x_0, \tau). \tag{A.2}$$

Finally as the field does not change appreciably during the evolution by ϵ we replace $E[x;\tau,\tau+\epsilon]$ by its mean value to get,

$$\Psi(x_\tau, x_\tau + x_\epsilon, \epsilon) \sim e^{-\beta\epsilon[\frac{F}{2}(-\frac{x_\epsilon}{\epsilon}-\theta)^2 + V(x_\tau)]}. \tag{A.3}$$

(We change notation by omitting the initial condition x_0 and replacing x_ϵ by x.)

Plugging everything in, performing the Gaussian integral, and discarding $\mathcal{O}(\epsilon^2)$ terms gives the diffusion equation, Eq. (2.3). Note that this connects to the assumption of the existence of a microscopic scale over which the external fields are constant and the polymer segment obeys Gaussian statistics.

A.4 The full many-body system

The full many-body problem is easily solved once the single-body wave functions above are known. Using Girardeau's mapping [91], the many-body Hamiltonian, Eq. (2.6) reduces to a sum of single-body Hamiltonians provided the many-body wave function obeys the constraint, $\Psi(\boldsymbol{x}) = \Psi(x_1, x_2, ..., x_N) = 0$ whenever any $x_i = x_j$. This constraint is satisfied by the Slater determinant of the single-body wave functions (the Bloch waves with complex momenta).

To get real-valued solutions, we note that since the Hamiltonian, Eq. (2.6), is real, its normalized eigenstates $\Psi_n(\boldsymbol{x})$ are either real or come in complex conjugate pairs. Thus we just need to ensure that the Slater determinant has either real eigenstates or pairs of complex conjugate ones.

For a filled band it is useful to define the solution in terms of Wannier functions rather than Bloch waves. The descriptions are equivalent since the determinant of a matrix of solutions is invariant on multiplication with a Unitary matrix. The Slater determinant in terms of the single-body Wannier functions, $\Phi_X(x)$, is

$$S(\boldsymbol{x}) = \frac{1}{\sqrt{N!}} \sum_{\sigma \in S_N} \operatorname{sgn}(\sigma) \prod_{i=1}^{N} \Phi_{X_i}(\sigma(x_i)), \tag{A.4}$$

where the Wannier functions, $\Phi_X(x)$, are related to the Bloch functions, $\Psi_k(x)$, by

$$\Phi_X(x) = \frac{1}{\sqrt{N}} \sum_k e^{-ikX} \Psi_k(x); X \in \{a, 2a, \ldots, Ma\}. \tag{A.5}$$

While the above defined functions are not unique (due to the freedom in choice of global phase for the Bloch functions) a unique set of real-valued Wannier functions can always be found [3].

Finally, since the polymers are distinguishable we restrict the domain of the constructed wave-function:

$$\Psi(\boldsymbol{x}) = \begin{cases} \sqrt{N!} S(\boldsymbol{x}) & \text{if } \boldsymbol{x} \in \mathcal{R}_0 \\ 0 & \text{elsewhere,} \end{cases} \tag{A.6}$$

where $\mathcal{R}_0$ is defined by the inequalities, $x_1 < x_2 < ... < x_N \pmod{Ma}$, and is the physical region allowed in our non-crossing problem [14]. This redefining does not interfere with the wave function being an eigenstate since it still satisfies the eigenvalue equation and is still continuous. (The derivative of the wave function is allowed to be discontinuous because of the singular terms, $\delta(x_i - x_j)$, in the Hamiltonian.)

Note that while Girardeau's fermion-to-boson mapping requires the determinant $S(\boldsymbol{x})$ be multiplied with an anti-symmetry factor, $A(\boldsymbol{x}) \in \{\pm 1\}$, to render it symmetric [91], this is not required since our wave function is non-zero only in $\mathcal{R}_0$.

A.5 Computation of band-structure and the critical angle

The band structure, $\varepsilon_n(k)$ at complex k can be computed using any electronic-structure calculations software such as Ref. [218] as used in Ref. [219].

In our case, we used the fact that exact solutions for the cosine potential, $V(x) = V_0 \cos(2\pi x/a)$ are known in terms of the Mathieu functions [147], which are implemented with high precision in computational software such as `Mathematica`. To generate Fig. 2.3, Fig. 2.5, and Fig. A.2, we computed the Floquet exponent (also called the Mathieu characteristic exponent for the specific case of the cosine potential) for different complex values of the energy eigenvalue ε. The imaginary part of the Floquet exponent is the same as $\operatorname{Im} k$ up to numerical factors. After computing a fine mesh of Floquet exponents for a range of energy eigenvalues, we interpolate the values to generate smooth sheets/curves. For Fig. 2.4, we used the fact that $\varepsilon_n(k)$ is real for k in the line segment joining $\frac{\pi}{a} - i\frac{\mu}{a}$ to $\frac{\pi}{a} + i\frac{\mu}{a}$ [35]. To find μ for any fixed value of potential strength, V_0, we then had to increase the value of $\operatorname{Im} k$ (with $\operatorname{Re} k$ fixed to π/a) until the corresponding value of ε became complex-valued.

A.6 DERIVATION OF POLYMER TILT

A.6.1 Tilt from energy eigenvalues

In Refs. [15, 65], the tilt angle of a polymer in a single-particle eigenstate Ψ_m of the Hamiltonian $\mathcal{H}(g)$ was shown to be related to the dependence of the energy eigenvalue on the force angle:

$$\phi = -\frac{\partial \varepsilon_m}{\partial g} = -\frac{1}{F}\frac{\partial \varepsilon_m}{\partial \theta}.$$

The expression was derived by defining a current operator in terms of a derivative of the Hamiltonian with respect to the vector potential strength g. Here, we provide an alternative derivation of this expression using classical probability currents under periodic boundary conditions, and also show that it describes the average tilt of the many-body system.

We begin by evaluating the change in the probability density function along the τ direction:

$$\begin{aligned}\frac{\partial p(x,\tau)}{\partial \tau} &\equiv \partial_\tau p(x,\tau) = \frac{1}{Z}\left[\widetilde{\Psi}\partial_\tau \Psi + \Psi \partial_\tau \widetilde{\Psi}\right] \\ &= \frac{1}{Z}\left[\frac{1}{2\beta F}\left(\widetilde{\Psi}\partial_x^2\Psi - \Psi\partial_x^2\widetilde{\Psi}\right) - \theta\left(\widetilde{\Psi}\partial_x\Psi + \Psi\partial_x\widetilde{\Psi}\right)\right].\end{aligned}$$

This change in density generates a local probability current $j(x,t)$ along the x direction through the continuity equation

$$\begin{aligned}&\partial_\tau p + \partial_x j = 0 \\ &\Rightarrow j(x,\tau) = \frac{1}{Z}\left[-\frac{1}{2\beta F}\left(\widetilde{\Psi}\partial_x\Psi - \Psi\partial_x\widetilde{\Psi}\right) + \theta\left(\widetilde{\Psi}\Psi\right)\right].\end{aligned}$$

The integrated probability current provides the rate of change in the average polymer position along the τ direction, which is the local tilt angle: $\partial_\tau\langle x\rangle = \int dx\, x\partial_\tau p = -\int dx\, x\partial_x j = \int dx\, j$, where the last step involves integration by parts on the periodic domain $0 \leq x < L_x$. Therefore, we obtain

$$\begin{aligned}\partial_\tau \langle x \rangle &= \int_0^{L_x} dx\, j(x,\tau) \\ &= -\frac{1}{2\beta F Z}\int_0^{L_x} dx \left(\widetilde{\Psi}\partial_x \Psi - \Psi \partial_x \widetilde{\Psi}\right) + \frac{\theta}{Z}\int_0^{L_x} dx\, \widetilde{\Psi}\Psi \\ &= -\frac{1}{\beta F Z}\int_0^{L_x} dx \left(\widetilde{\Psi}\partial_x \Psi\right) + \theta, \end{aligned} \tag{A.7}$$

where the last step again involves integration by parts. To understand the origin of the constant term, consider a single polymer wandering across a featureless substrate $V(x) = 0$ at a nonzero force angle with free ends. The aggregated density profile is a constant over all space so $\partial_x \Psi = 0$, yet the polymer aligns to the force direction on average so the tilt equates to θ.

To express the above equation in terms of the eigenvalues we first note that,

$$\begin{aligned}\mathcal{H}(g) &= \frac{(p+ig)^2}{2m} + V(x) \\ &= -\frac{1}{2\beta^2 F}\partial_x^2 + \frac{\theta}{\beta}\partial_x - \frac{F\theta^2}{2} + V(x), \end{aligned} \tag{A.8}$$

such that,

$$\partial_\theta \mathcal{H}(g) = \frac{1}{\beta}\partial_x - F\theta. \tag{A.9}$$

Now we expand the equation $\partial_\theta(\mathcal{H}\Psi_n) = \partial_\theta(\varepsilon_n \Psi_n)$, multiply both sides by $\widetilde{\Psi}_m(x)$ and integrate,

$$\int dx\, (\widetilde{\Psi}_m (\partial_\theta \mathcal{H})\Psi_n + (\varepsilon_m - \varepsilon_n)\widetilde{\Psi}_m \partial_\theta \Psi_n) = \delta_{mn}\partial_\theta \varepsilon_m. \tag{A.10}$$

We used $\mathcal{H}^\dagger \widetilde{\Psi}_m^* = \varepsilon_m^* \widetilde{\Psi}_m^*$ to simplify $\widetilde{\Psi}_m \mathcal{H} = \varepsilon_m \widetilde{\Psi}_m$. If $m = n$ (we will be using ground-state dominance), we get,

$$\partial_\theta \varepsilon_m = \int dx\, \widetilde{\Psi}_m (\partial_\theta \mathcal{H})\Psi_m = \frac{1}{\beta}\int dx\, \widetilde{\Psi}_m \partial_x \Psi_m - F\theta. \tag{A.11}$$

Given specific boundary conditions at the polymer ends, we can write the tilt of an arbitrary polymer state using the spectral expansion introduced in the main text; this

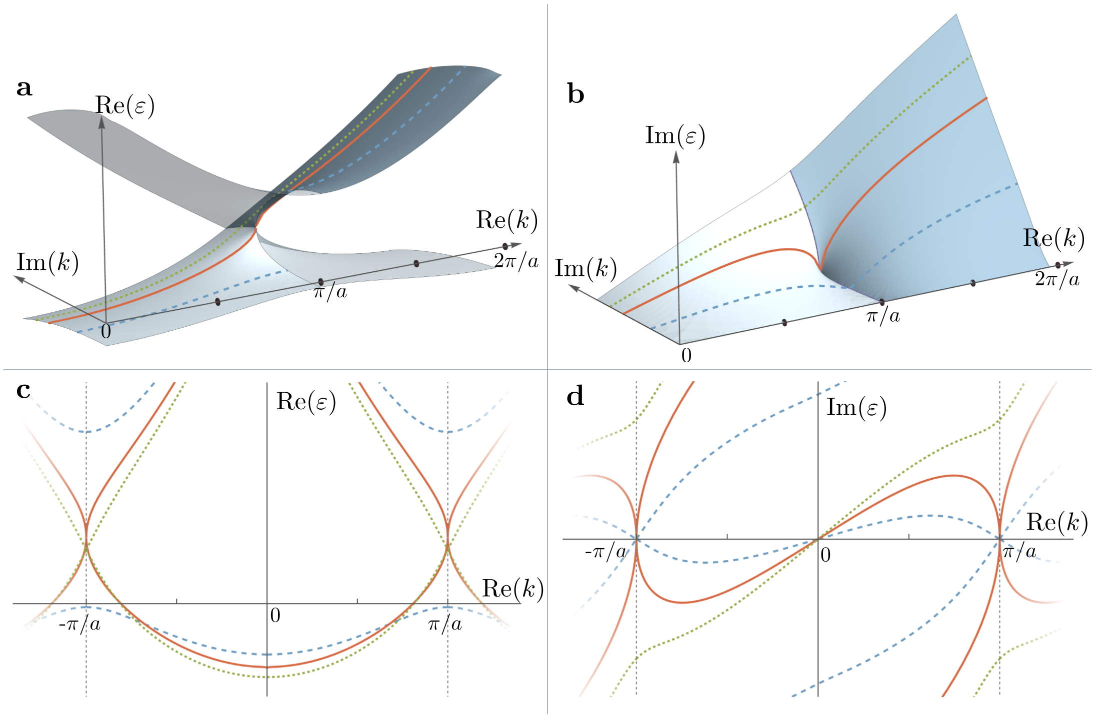

Figure A.2. The complex band-structure $\varepsilon(k)$ of the Hamiltonian, $\frac{p^2}{2m} + V(x)$ with $V(x) = \cos(x)$ as a function of complex k. Panels **a** and **b** show the real and imaginary parts, respectively, of the lowest two bands (Riemann sheets ordered by the real part of the energy) of $\varepsilon(k)$. The lowest band is plotted as a solid surface in the interval $0 < \mathrm{Re}\, k < \pi/a$ and the next band is plotted in the interval $\pi/a < \mathrm{Re}\, k < 2\pi/a$. In panel **a**, the other band in each region is shown as a translucent surface. Only the region with $\mathrm{Re}\, k \geq 0$ and $\mathrm{Im}\, k \geq 0$ is shown since on changing the sign of either $\mathrm{Re}\, k$ or of $\mathrm{Im}\, k$, $\varepsilon(k)$ turns into $\varepsilon(k)^*$ [3]. The three contours are at $\mathrm{Im}\, k = 0.5\mu/a$ (blue, dashed), $\mathrm{Im}\, k = \mu/a$ (red, solid) which corresponds to the critical shear, and $\mathrm{Im}\, k = 1.25\mu/a$ (green, dotted). Panels **c** and **d** show these contours in the full Brillouin zone, illustrating that $\varepsilon(k)$ is periodic upon advancing $\mathrm{Re}(k)$ by $2\pi/a$.

would give a local tilt angle dependent on the vertical coordinate τ. In the interior of a long polymer, however, ground-state dominance dictates that $(\Psi, \widetilde{\Psi}) \to (\Psi_0, \widetilde{\Psi}_0)$ and, on substituting Eq. (A.11) in Eq. (A.7), the local tilt angle becomes a constant,

$$\partial_\tau \langle x \rangle = -\frac{1}{F}\frac{\partial \varepsilon_0}{\partial \theta} \to \phi. \tag{A.12}$$

We equate this to the measured tilt angle, ϕ, in the simulations.

For a system of many polymers, we now have N probability currents j_n and the continuity equation is transformed to

$$\partial_\tau p(\boldsymbol{x};\tau) + \sum_{i=1}^{N} \partial_{x_i} j_i(\boldsymbol{x};\tau) = 0.$$

The local tilt angle associated with the nth polymer is obtained by integrating the corresponding current:

$$\begin{aligned}\partial_\tau \langle x_n \rangle &= -\int_0^{L_x} d\boldsymbol{x}\, x_n \sum_i \partial_{x_i} j_i(\boldsymbol{x};\tau) \\ &= \int_0^{L_x} d\boldsymbol{x}\, j_n(\boldsymbol{x};\tau) \\ &= -\frac{1}{\beta F \boldsymbol{Z}} \int_0^{L_x} d\boldsymbol{x} \left(\widetilde{\Psi} \partial_{x_n} \Psi\right) + \theta,\end{aligned}$$

where $\boldsymbol{Z} = \int d\boldsymbol{x}\, (\widetilde{\Psi}\Psi)$. Since all the polymers are statistically identical, the equilibrium tilt of an individual polymer is the same as the average tilt of all the polymers, which decomposes into a sum of single-particle terms under the mapping we use for noncrossing polymers:

$$\begin{aligned}\overline{\partial_\tau \langle x_n \rangle} &= \frac{1}{N}\sum_n \left[-\frac{1}{\beta F \boldsymbol{Z}} \int_0^{L_x} d\boldsymbol{x} \left(\widetilde{\Psi} \sum_n \partial_{x_n} \Psi\right) + \theta\right] \\ &= \frac{1}{NF\boldsymbol{Z}} \int_0^{L_x} d\boldsymbol{x}\, \widetilde{\Psi} \left(\partial_\theta \sum_n \mathcal{H}_n(g)\right) \Psi. \end{aligned} \tag{A.13}$$

Under ground-state dominance the average tilt angle again depends solely on the many-body energy eigenstate with the lowest real part and we obtain Eq. (2.24) of the main text:

$$\phi = -\frac{1}{NF}\frac{\partial \boldsymbol{\varepsilon}_0}{\partial \theta}.$$

A.6.2 Using the analytical properties of the complex band structure

Eqn. (2.28) of the main text establishes that the tilt can be simplified to,

$$\phi = \frac{\beta a}{\pi}\,\mathrm{Im}\left(\varepsilon_0\left(\frac{\pi}{a} + i\beta F\theta\right)\right).$$

The multivalued function $\varepsilon(k)$ is also periodic upon advancing $\mathrm{Re}(k)$ by $2\pi/a$ [3]. At constant $\mathrm{Im}(k) = \beta F\theta$ with $\theta < \theta_\mathrm{c}$, the Riemann sheet $\varepsilon_0(k)$ is well-separated from its adjacent sheets (which form higher bands), and is itself periodic with the same periodicity as $\varepsilon(k)$ (see Fig. A.2**a**). This implies that $\varepsilon_0\left(-\frac{\pi}{a} + i\beta F\theta\right) = \varepsilon_0\left(\frac{\pi}{a} + i\beta F\theta\right)$, and the average tilt (Eq. (2.27)) evaluates to zero.

By contrast, when $\mathrm{Im}(k) > \mu_0/a = \beta F\theta_\mathrm{c}$, i.e., for force angles above the critical angle, the real part of the lowest band touches the next band at $\mathrm{Re}(k) = \pm\pi/a$ (see Fig. A.2). Now, although the multivalued function $\varepsilon(k)$ is still periodic along the $\mathrm{Re}(k)$ axis, the sheet $\varepsilon_0(k)$ with the lowest real part of the energy is no longer periodic. Upon smoothly following ε_0 from one endpoint of the contour to the other, the real component returns to its starting value, whereas the imaginary component is nonzero at either endpoint. This feature is apparent in the shapes of the dashed lines in Fig. 2.3 above the critical contour: the oval corresponding to the lowest band opens up when it merges with the next band, but remains symmetric about the $\mathrm{Re}(\varepsilon)$ axis. Therefore, the average tilt becomes nonzero when $\theta > \theta_\mathrm{c}$, since the closed oval corresponding to the lowest band 'opens up' by merging with the next band and $\varepsilon_0\left(\frac{\pi}{a} + i\beta F\theta\right)$ becomes complex-valued.

We can deduce additional features of the ϕ–θ curve near θ_c from known analytic properties of $\varepsilon(k)$. Near the branch point $k_0 = \pi/a + iF\beta\theta_\mathrm{c}$, the energy behaves as $\varepsilon_0(k) = \varepsilon_0(k_0) + Ae^{i\frac{\pi}{4}}(k - k_0)^{1/2}$ to lowest order in $(k - k_0)$, where A is a nonzero real constant [3, 35]. Since $\varepsilon_0(k_0)$ is real, the imaginary part of $\varepsilon_0(\frac{\pi}{a} + i\beta F\theta)$ has the following behavior near θ_c:

$$\mathrm{Im}\left(\varepsilon_0\left(\frac{\pi}{a} + i\beta F\theta\right)\right) = \begin{cases} 0 & \theta < \theta_\mathrm{c} \\ \frac{A}{\sqrt{2}}\sqrt{F\beta a(\theta - \theta_\mathrm{c})} & \theta > \theta_\mathrm{c} \end{cases} \tag{A.14}$$

Immediately after the transition, therefore, the tilt is expected to grow as $\phi \sim (\theta - \theta_\mathrm{c})^{1/2}$ in the limit of large system sizes.

Finally, for very large values of the force angle and hence of $\mathrm{Im}(k)$, the momentum term dominates the Hamiltonian and we can ignore the potential term. The eigenfunctions of $\hat{H}$ are of the form e^{ikx} with energy-momentum relation $\varepsilon(k) = \frac{k^2}{2\beta^2 F}$. For $\theta \gg \theta_\mathrm{c}$, we therefore expect

$$\begin{aligned} \mathrm{Im}\left(\varepsilon_0\left(\frac{\pi}{a} + i\beta F\theta\right)\right) &= \frac{1}{2\beta^2 F}\,\mathrm{Im}\left(\left(\frac{\pi}{a} + i\beta F\theta\right)^2\right) \\ &= \frac{\pi}{\beta a}\theta, \end{aligned} \tag{A.15}$$

from which we obtain $\phi = \theta$ from Eq. (2.28).

The calculations can be easily generalized to arbitrary fillings too. For N polymers and M potential wells, where N is odd, we get,

$$\begin{aligned} \phi = -\frac{1}{NF}\frac{\partial \boldsymbol{\varepsilon}_0}{\partial\theta} &= -\frac{M\beta a}{N2\pi}\int_{-\frac{\pi(N-1)}{Ma}}^{\frac{\pi(N-1)}{Ma}} dk\,\frac{\partial\,\mathrm{Re}(\varepsilon_0(k))}{\partial\,\mathrm{Im}(k)}, \\ &= \frac{M}{N}\frac{\beta a}{\pi}\,\mathrm{Im}\left(\varepsilon_0\left(\frac{\pi(N-1)}{Ma} + i\beta F\theta\right)\right). \end{aligned} \tag{A.16}$$

This corresponds to the path along increasing values of $\mathrm{Im}\,k$ at constant $\mathrm{Re}\,k = \frac{\pi(N-1)}{Ma}$ in Fig. A.2**b**. When N is even, the many-body ground-state eigenvalues and eigenstates come in complex-conjugate pairs. In that case, the generalization of the calculation requires forming appropriate superpositions of the two complex-conjugate states, in terms of their real and imaginary parts, to keep the probability density, $p(\boldsymbol{x}, \tau)$, real.

The calculations in this Appendix rely on generic features of the complex band structures of one-dimensional periodic potentials as detailed in Refs. [3], [35] and [4]. We can verify these general predictions for the specific (cosine) potential we have used in our study, for which we can compute the complex-valued energy bands following Appendix A.5. Figure A.2 shows the three distinct behaviors for Eq. (2.28) as the force angle is increased.

APPENDIX B

APPENDICES TO **Chapter III** ON PARAMETRIC OSCILLATORS

B.1 Generalizations to other mechanical systems

B.1.1 Hamiltonian approach to deriving symmetries

A classical mechanical system is described by n coordinates x_i and n canonically conjugate momenta p_i. The classical-mechanical Hamiltonian $\mathcal{H}(\boldsymbol{x},\boldsymbol{p})$ governs the dynamics via the equations

$$\frac{dx_i}{dt} = +\frac{\partial\mathcal{H}}{\partial p_i} \quad \text{and} \quad \frac{dp_i}{dt} = -\frac{\partial\mathcal{H}}{\partial x_i} \tag{B.1}$$

which can be written in matrix form as

$$\frac{d}{dt}\begin{pmatrix}\boldsymbol{x}\\ \boldsymbol{p}\end{pmatrix} = \begin{pmatrix}0 & \mathbb{I}_n\\ -\mathbb{I}_n & 0\end{pmatrix}\begin{pmatrix}\nabla_{\boldsymbol{x}}\mathcal{H}\\ \nabla_{\boldsymbol{p}}\mathcal{H}\end{pmatrix}. \tag{B.2}$$

If the Hamiltonian is a quadratic function, the equations of motion would be linear. A general quadratic Hamiltonian is

$$\mathcal{H} = \sum_{i,j}\left(\frac{a_{ij}}{2}x_i x_j + \frac{b_{ij}}{2}p_i p_j + c_{ij}x_i p_j\right) \tag{B.3}$$

where $a_{ij} = a_{ji}$ and $b_{ij} = b_{ji}$. The coefficients above, which may in general be time-dependent, define the real matrices A, B, and C, where A and B are symmetric. For such a Hamiltonian we have

$$\begin{pmatrix}\nabla_{\boldsymbol{x}}\mathcal{H}\\ \nabla_{\boldsymbol{p}}\mathcal{H}\end{pmatrix} = \begin{pmatrix}A & C\\ C^T & B\end{pmatrix}\begin{pmatrix}\boldsymbol{x}\\ \boldsymbol{p}\end{pmatrix}. \tag{B.4}$$

Our linear system is then

$$\frac{d}{dt}\begin{pmatrix}\boldsymbol{x}\\ \boldsymbol{p}\end{pmatrix} = \begin{pmatrix}C^T & B\\ -A & -C\end{pmatrix}\begin{pmatrix}\boldsymbol{x}\\ \boldsymbol{p}\end{pmatrix}. \tag{B.5}$$

All linear systems which can be written in this form enjoy the internal symmetries discussed in this work. We show below how mechanical systems with velocity-dependent forces or dissipation can be accomodated, under some assumptions, to match the form above.

B.1.2 Effect of gyroscopic forces

In the presence of (time-independent) gyroscopic forces, the equations of motion generalize to [18]

$$\ddot{\boldsymbol{x}} = -K(t)\boldsymbol{x} + \Gamma\dot{\boldsymbol{x}}. \tag{B.6}$$

Here, Γ is a real and skew-symmetric matrix ($\Gamma^T = -\Gamma$) which accounts for the frictionless forces that break reciprocity, such as the Lorentz force and the Coriolis force. Such forces take the form $\vec{F} = \vec{\Omega} \times \dot{\vec{x}} = \sum_{jkl} \epsilon_{jkl}\Omega_j \dot{x}_k \hat{e}_l$ where $\sum_j \epsilon_{jkl}\Omega_j$ indeed reverses its sign upon the interchange of k and l [21].

To reach the desired form we define the vector $\boldsymbol{v} = \dot{\boldsymbol{x}} - \frac{\Gamma}{2}\boldsymbol{x}$ such that

$$\dot{\boldsymbol{v}} = \left(-K(t) + \frac{\Gamma^2}{4}\right)\boldsymbol{x} + \frac{\Gamma}{2}\boldsymbol{v}. \tag{B.7}$$

Thus,

$$\begin{pmatrix} \dot{\boldsymbol{x}} \\ \dot{\boldsymbol{v}} \end{pmatrix} = \begin{pmatrix} \frac{\Gamma}{2} & I_n \\ -K(t) + \frac{\Gamma^2}{4} & \frac{\Gamma}{2} \end{pmatrix} \begin{pmatrix} \boldsymbol{x} \\ \boldsymbol{v} \end{pmatrix}, \tag{B.8}$$

which is of the same form as Eq. (B.5).

B.1.3 Effect of dissipation due to friction

In the presence of dissipation due to friction the Hamiltonian changes to

$$H_{\mathrm{d}}(t) = -i \begin{pmatrix} 0 & -\mathbb{I}_n \\ K(t) & \gamma \end{pmatrix} \tag{B.9}$$

where γ is a diagonal matrix with the j^{th} term in the diagonal being the dissipation constant corresponding to the j^{th} momenta. The trace-less matrix

$$\tilde{H}(t) = H_{\mathrm{d}}(t) + \frac{i}{2}\begin{pmatrix} \gamma & 0 \\ 0 & \gamma \end{pmatrix} = -i\begin{pmatrix} -\frac{1}{2}\gamma & -\mathbb{I}_n \\ K(t) & \frac{1}{2}\gamma \end{pmatrix} \tag{B.10}$$

has the same symmetries as the frictionless Hamiltonian $H(t)$ in Eq. (3.9) of the main text. That is, $\tilde{H}(t)$ is also purely imaginary and it also satisfies the pseudo-Hermiticity condition, $G\tilde{H}(t)G^{-1} = \tilde{H}^{\dagger}(t)$, as in Eq. (3.7) of the main text [161]. Essentially, we converted $H_{\mathrm{d}}(t)$ to a matrix $\tilde{H}(t)$ with balanced gain and loss.

However, for such a transformation to be permissible in a time-dependent system, we have to assume that the dissipation is uniform, i.e., the dissipation coefficient is the same for all oscillators such that $\tilde{H}(t) = H_{\mathrm{d}}(t) + \frac{i}{2}\gamma\mathbb{I}_{2n}$ where γ now denotes a real number. In this case, we can transform our coordinates via

$$\begin{pmatrix} \tilde{\boldsymbol{x}}(t) \\ \tilde{\boldsymbol{p}}(t) \end{pmatrix} = e^{\frac{\gamma t}{2}}\begin{pmatrix} \boldsymbol{x}(t) \\ \boldsymbol{p}(t) \end{pmatrix} \tag{B.11}$$

to get as a new equation of motion

$$i\frac{d}{dt}\begin{pmatrix} \tilde{\boldsymbol{x}}(t) \\ \tilde{\boldsymbol{p}}(t) \end{pmatrix} = \tilde{H}(t)\begin{pmatrix} \tilde{\boldsymbol{x}}(t) \\ \tilde{\boldsymbol{p}}(t) \end{pmatrix}. \tag{B.12}$$

B.2 REVIEW OF FLOQUET METHODS

B.2.1 Long-time behavior of system

The equation $U(t+T) = U(t)U(T)$ can be derived as (with $\mathcal{T}$ being the time-ordering operator),

$$\begin{aligned} U(t+T) &= \mathcal{T}\left[\exp\left(-i\int_0^{t+T} dt' H(t')\right)\right] \\ &= \mathcal{T}\left[\exp\left(-i\int_T^{t+T} dt' H(t')\right)\right] U(T) \\ &= \mathcal{T}\left[\exp\left(-i\int_0^{t} dt' H(t')\right)\right] U(T) \\ &= U(t)U(T). \end{aligned} \tag{B.13}$$

This implies $U(mT) = U(T)^m$ where m is any positive integer.

Given initial conditions $\{\boldsymbol{x}(0), \boldsymbol{p}(0)\}$, the coordinates of the system after m time-periods is given by

$$\begin{pmatrix} \boldsymbol{x}(mT) \\ \boldsymbol{p}(mT) \end{pmatrix} = U(mT) \begin{pmatrix} \boldsymbol{x}(0) \\ \boldsymbol{p}(0) \end{pmatrix} = U(T)^m \begin{pmatrix} \boldsymbol{x}(0) \\ \boldsymbol{p}(0) \end{pmatrix}. \tag{B.14}$$

Let $|v_i\rangle$ be the eigenvectors of $U(T)$, i.e. the Floquet eigenvectors, with eigenvalues λ_i, the Floquet multipliers. If the Floquet eigenvectors span all space, we can write the initial conditions as a superposition of these eigenvectors.

$$\begin{pmatrix} \boldsymbol{x}(0) \\ \boldsymbol{p}(0) \end{pmatrix} = \sum_i \alpha_i |v_i\rangle, \tag{B.15}$$

such that the equation above reduces to

$$\begin{pmatrix} \boldsymbol{x}(mT) \\ \boldsymbol{p}(mT) \end{pmatrix} = \sum_i \alpha_i \lambda_i^m |v_i\rangle. \tag{B.16}$$

The Floquet multipliers then determine the long time behavior of the system. A similar statement is true even in the case of an exceptional point when the Floquet eigenvectors do not span the whole space [28]. For example, let $U(T)$ have a two-fold exceptional point degeneracy at λ_j. We can then define the generalized eigenvector $|w_j\rangle$ at λ_j by

$$\begin{aligned} U(T)|v_j\rangle &= \lambda_j|v_j\rangle, \\ U(T)|w_j\rangle &= \lambda_j|w_j\rangle + |v_j\rangle. \end{aligned} \tag{B.17}$$

The vectors $\{|w_j\rangle, |v_1\rangle, \ldots, |v_{n-1}\rangle\}$ span all space and we can write our initial conditions as

$$\begin{pmatrix} \boldsymbol{x}(0) \\ \boldsymbol{p}(0) \end{pmatrix} = \sum_i \alpha_i |v_i\rangle + \beta_j |w_j\rangle, \tag{B.18}$$

such that

$$\begin{pmatrix} \boldsymbol{x}(mT) \\ \boldsymbol{p}(mT) \end{pmatrix} = \sum_i \alpha_i \lambda_i^m |v_i\rangle + \beta_j \left(\lambda_j^m |w_j\rangle + m\lambda_j^{m-1}|v_j\rangle \right). \tag{B.19}$$

B.2.2 Frequency of Floquet modes

When initial conditions of the oscillators are set to one of the Floquet eigenvectors, we call the ensuing motion a Floquet mode. We saw above that, in the absence of exceptional points, the dynamics of the system can be decomposed into the Floquet modes much like how the dynamics of a static system can be decomposed into its normal modes. The frequency of oscillations of a Floquet mode depends both on the modulation frequency and the Floquet multiplier for that eigenvector. For example, with initial conditions $\begin{pmatrix} \boldsymbol{x}(0) \\ \boldsymbol{p}(0) \end{pmatrix} = |v_i\rangle$, the system evolves as

$$\begin{pmatrix} \boldsymbol{x}(t) \\ \boldsymbol{p}(t) \end{pmatrix} = U(t)|v_i\rangle = U(mT + t_0)|v_i\rangle = U(t_0)\lambda_i^m |v_i\rangle. \tag{B.20}$$

Here, $t = mT + t_0$ with m a non-negative integer and $0 \leq t_0 < T$. Expressing, the Floquet multiplier as $\lambda_i = e^{(\alpha_i - i\omega_i)T}$ with α_i and ω_i real, we have

$$\begin{pmatrix} \boldsymbol{x}(t) \\ \boldsymbol{p}(t) \end{pmatrix} = U(t_0) e^{-im\omega_i T} e^{m\alpha_i T} |v_i\rangle. \tag{B.21}$$

We see that the coordinates of the oscillators return to the scaled value of their initial coordinates when $U(t_0)$ equals identity and $e^{-im\omega_i T}$ equals one. The first time this happens is at time equal to the least common multiple of the modulation time-period T and $\frac{2\pi}{\omega_i}$. This least common multiple is the time-period of the Floquet mode.

We consider two specific cases. When parametric amplification occurs due to a Krein collision of eigenvalues at $+1$, the Floquet multipliers for the nascent modes have $\omega_i = 0$. The frequency of these modes are then locked to the modulation frequency. On the other hand, when the collision occurs at -1, the Floquet multipliers for the nascent modes have $\omega_i = \frac{\pi}{T}$, and their frequency is locked to twice the modulation frequency.

B.3 Derivation of generalized Floquet theorem in the presence of space-time symmetry

The matrix S, which cyclically shifts each oscillator's coordinates by one position to the left, satisfies

$$S \begin{pmatrix} x_1 \\ x_2 \\ \vdots \\ x_n \\ p_1 \\ p_2 \\ \vdots \\ p_n \end{pmatrix} = \begin{pmatrix} x_2 \\ \vdots \\ x_n \\ x_1 \\ p_2 \\ \vdots \\ p_n \\ p_1 \end{pmatrix}. \tag{B.22}$$

For the time-propogation operator, we have (with $\mathcal{T}$ being the time-ordering operator),

$$\begin{aligned} U(t+T/n) &= \mathcal{T}\left[\exp\left(-i\int_0^{t+T/n} dt' H(t')\right)\right] \\ &= \mathcal{T}\left[\exp\left(-i\int_{T/n}^{t+T/n} dt' H(t')\right)\right] U(T/n) \\ &= \mathcal{T}\left[\exp\left(-i\int_0^{t} dt' S^{-1} H(t') S\right)\right] U(T/n) \\ &= S^{-1}U(t)SU(T/n). \end{aligned} \tag{B.23}$$

The derivation for Floquet systems in **Section B.2** is a special case of this derivation above.

B.4 Dependence of resonance on functional form and strength of parameter modulation

APPENDIX C

APPENDICES TO **Chapter II** ON PSEUDO-HERMITIAN MATRICES

C.1 Proofs for statements in **Section 5.3**

In this section, $U = e^{-iH}$ such that $G = U^\dagger G U$ [see Eq. (5.14)].

Lemma 1. *Let* λ *be an eigenvalue of* H *such that* $\operatorname{Im}\lambda \neq 0$ *and* $|v\rangle$ *a corresponding eigenvector. Then,* $\langle v|G|v\rangle = 0$*.*

Proof. We have

$$\begin{aligned}\langle v|G|v\rangle &= \langle v|U^\dagger G U|v\rangle \\ &= \langle v|e^{+i\lambda^*} G e^{-i\lambda}|v\rangle \\ &= e^{2\mathrm{Im}\lambda}\langle v|G|v\rangle.\end{aligned} \tag{C.1}$$

Since, $e^{2\mathrm{Im}\lambda} \neq 1$ we have $\langle v|G|v\rangle = 0$. □

Lemma 2. *Let* λ *be a real eigenvalue of* H *with geometric multiplicity less than algebraic multiplicity (an exceptional point). Then,* $\langle v|G|v\rangle = 0$ *for some corresponding eigenvector* $|v\rangle$*.*

Proof. Since the algebraic multiplicity of λ is greater than its geometric multiplicity, we can define at least two linearly independent vectors $|v\rangle$ and say $|w\rangle$ such that

$$H|v\rangle = \lambda|v\rangle \quad \text{or} \quad U|v\rangle = e^{-i\lambda}|v\rangle, \text{ and} \tag{C.2}$$

$$H|w\rangle = \lambda|w\rangle + |v\rangle \quad \text{or} \quad U|w\rangle = e^{-i\lambda}|w\rangle - ie^{-i\lambda}|v\rangle. \tag{C.3}$$

$|w\rangle$ is called a generalized eigenvector and satisfies $(H - \lambda\mathbb{I})^k|w\rangle = 0$ with $k > 1$. [The second part of Eq. (C.3) follows from $H^n|w\rangle = \lambda^n|w\rangle + n\lambda^{n-1}|v\rangle$, which can be proven by mathematical induction.] Then,

$$\begin{aligned}\langle v|G|w\rangle &= ((\langle v|U^\dagger)G(U|w\rangle)) \\ &= e^{+i\lambda^*}\langle v|G(e^{-i\lambda}|w\rangle - ie^{-i\lambda}|v\rangle) \\ &= \langle v|G|w\rangle - i\langle v|G|v\rangle, \end{aligned} \tag{C.4}$$

implying $\langle v|G|v\rangle$ is zero. □

C.2 Proof of Krein-Gel'fand-Lidskii Theorem

Let $H(\boldsymbol{k})$ be a parameterized pseudo-Hermitian matrix such that $G(\boldsymbol{k})H(\boldsymbol{k}) = H^\dagger(\boldsymbol{k})G(\boldsymbol{k})$. $H(\boldsymbol{k})$ and $G(\boldsymbol{k})$ are continuous functions of the parameter(s) $\boldsymbol{k}$, and $G(\boldsymbol{k})$ is Hermitian and invertible for all values of $\boldsymbol{k}$. Note that the case of $G(\boldsymbol{k}) = G$ being constant is automatically covered as a special case.

C.2.1 Proof of sufficiency

To show that if $\langle v|G(\boldsymbol{k} = \boldsymbol{k}_0)|v\rangle \neq 0$ for all eigenvectors associated with λ_0, a real eigenvalue of $H(\boldsymbol{k} = \boldsymbol{k}_0)$, then λ_0 stays real and diabolic upon small perturbations of $\boldsymbol{k}$.

Proof. Suppose the contrary. Then there exists a sequence of matrices, $H_1, H_2, \cdots \to H_0 = H(\boldsymbol{k}_0)$ and $G_1, G_2, \cdots \to G_0 = G(\boldsymbol{k}_0)$ such that an eigenvalue λ_m of H_m has either non-zero imaginary part or algebraic multiplicity strictly more than geometric multiplicity. In either case, $\langle v_m|G_m|v_m\rangle = 0$ where $H_m|v_m\rangle = \lambda_m|v_m\rangle$ and $G_mH_m = H_m^\dagger G_m$.

While the sequence $|v_1\rangle, |v_2\rangle, \cdots \to |v_0\rangle$ may not be convergent, we can select a subsequence such that $|v_{m_j}\rangle \to |v\rangle$ as $m_j \to \infty$. By suitably changing the notation, we have $|v_m\rangle \to |v\rangle$ as $m \to \infty$. Letting $m \to \infty$ in the above equalities, we obtain

$$H_0|v\rangle = \lambda_0|v\rangle \quad \text{with } \langle v|G_0|v\rangle = 0. \tag{C.5}$$

But we assumed $\langle v|G_0|v\rangle \neq 0$ for all eigenvectors associated with λ_0. □

This proof closely follows the one given in Chapter III of Ref. [28]. An alternate proof can be found in Ref. [164].

C.2.2 Proof of necessity

To show that if $H(\boldsymbol{k} = \boldsymbol{k}_0)$ has real eigenvalues and $\langle v|G(\boldsymbol{k} = \boldsymbol{k}_0)|v\rangle = 0$ for some eigenvector associated to an eigenvalue λ, then it is possible to perturb $\boldsymbol{k}$ in such a way that λ splits into complex conjugate eigenvalues.

Proof. We write $H(\boldsymbol{k} = \boldsymbol{k}_0) := H(0)$ in its Jordan normal form, $H(0) = PJP^{-1}$. The columns of the matrix P are the generalized right eigenvectors of $H(0)$ which we denote by $|R_i\rangle$. The rows of the matrix P^{-1} are the generalized left eigenvectors of $H(0)$, which we denote by $\langle L_i|$. Evidently, $\langle L_i|R_j\rangle = \delta_{ij}$ since $P^{-1}P$ is the identity. We will work with this biorthonormal basis.

Case of diabolic point. We consider the case of a diabolic point at λ such that $H(0)$ is diagonalizable at least in the associated root subspace. This case will, in particular, also prove that an exceptional point is not necessary for symmetry breaking to occur.

For simplicity we will assume that the degeneracy in λ is twofold,

$$H(0) = (\lambda|R_1\rangle\langle L_1| + \lambda|R_2\rangle\langle L_2|) \oplus \tilde{H}, \tag{C.6}$$

where $\tilde{H}$ is the projection of the matrix in the rest of the space. A general Hermitian matrix can be expressed in terms of the left eigenvectors of H as $M = \sum_{i,j} m_{ij}|L_i\rangle\langle L_j|$.

We claim that G can be written as

$$G = (\eta_1 |L_1\rangle\langle L_1| + \eta_2 |L_2\rangle\langle L_2|) \oplus \tilde{G} \tag{C.7}$$

$$:= G_\lambda \oplus \tilde{G}, \tag{C.8}$$

where $\tilde{G}$ is the projection of G in the subspace spanned by $\{|L_3\rangle, |L_4\rangle, \dots\}$.

To show that there are no cross terms such as $|L_i\rangle\langle L_1|$ or $|L_i\rangle\langle L_2|$, with $i > 2$, in the expression above, we need to show that $\langle R_i|G|R_1\rangle = \langle R_i|G|R_2\rangle = 0$ for $i > 2$. If $|R_i\rangle$ is an eigenvector, we have

$$\begin{aligned}\langle R_i|G|R_1\rangle &= \langle R_i|U(t)^\dagger G U(t)|R_1\rangle \\ &= \langle R_i|e^{+i\lambda_i^* t} G e^{-i\lambda t}|R_1\rangle \\ &= e^{i(\lambda_i^* - \lambda)t}\langle R_i|G|R_1\rangle.\end{aligned} \tag{C.9}$$

Since $\lambda_i \neq \lambda$, $e^{i(\lambda_i^* - \lambda)t} \neq 1$ at all times t, and thus $\langle R_i|G|R_1\rangle = 0$. Similarly, $\langle R_i|G|R_2\rangle = 0$. If on the other hand, $|R_i\rangle$ is a generalized eigenvector we proceed similar to Lemma 2.

We can now choose $|L_1\rangle$ and $|L_2\rangle$ appropriately to diagonalize G in this subspace. Since G is Hermitian and invertible and $\langle R|G|R\rangle = 0$ for some eigenvector associated with λ, we must have $\eta_1 = \langle R_1|G|R_1\rangle$ and $\eta_2 = \langle R_2|G|R_2\rangle$ being real, nonzero, and of opposite signs.

The proof is now simply done by construction. A Hamiltonian which is pseudo-Hermitian with respect to G_λ, $H^\dagger G_\lambda = G_\lambda H$, is

$$\begin{aligned}H = &\; a|R_1\rangle\langle L_1| + \eta_2(b + ic)|R_1\rangle\langle L_2| \\ &+ \eta_1(b - ic)|R_2\rangle\langle L_1| + d|R_2\rangle\langle L_2|\end{aligned} \tag{C.10}$$

with a, b, c, d being arbitrary real constants. We now set $a = d = \lambda \cos(x), b = \frac{\lambda \sin(x)}{\sqrt{|\eta_1 \eta_2|}}, c = 0$ to get

$$\begin{aligned} H(x) = \lambda\Bigg(& \cos(x)|R_1\rangle\langle L_1| + \eta_2 \frac{\sin(x)}{\sqrt{|\eta_1\eta_2|}}|R_1\rangle\langle L_2| \\ & + \eta_1 \frac{\sin(x)}{\sqrt{|\eta_1\eta_2|}}|R_2\rangle\langle L_1| + \cos(x)|R_2\rangle\langle L_2|\Bigg) \oplus \tilde{H}, \end{aligned} \tag{C.11}$$

which has eigenvalues $\lambda e^{\pm ix}$ in the relevant subspace. These eigenvalues are complex-valued for real x and at $x = 0$ we recover the original Hamiltonian, $H(0)$.

Case of exceptional point. The proof is similar when there is an exceptional point at λ, a real eigenvalue of $H(0)$. For simplicity we will again assume that the degeneracy in λ is twofold,

$$H(0) = (\lambda|R_1\rangle\langle L_1| + \lambda|R_2\rangle\langle L_2| + |R_1\rangle\langle L_2|) \oplus \tilde{H}. \tag{C.12}$$

Here, $|R_1\rangle$ is a right eigenvector of $H(0)$ and $|R_2\rangle$ a generalized right eigenvector.

G can again be made block-diagonal in the left eigenvector basis (see the diabolic case). We now use Eqs. (C.2) and (C.3) to show that $\langle R_1|G|R_2\rangle = \langle R_2|G|R_1\rangle$,

$$\begin{aligned} \langle R_2|G|R_2\rangle &= \langle R_2|U^\dagger G U|R_2\rangle \\ &= \left(e^{i\lambda}\langle R_2| + ie^{i\lambda}\langle R_1|\right) G \left(e^{-i\lambda}|R_2\rangle - ie^{-i\lambda}|R_1\rangle\right) \\ &= \langle R_2|G|R_2\rangle + i\langle R_1|G|R_2\rangle - i\langle R_2|G|R_1\rangle. \end{aligned} \tag{C.13}$$

Since G_λ is Hermitian and invertible, and $\langle R_1|G|R_1\rangle = 0$ by Lemma 2, we must have

$$G_\lambda = \eta_1|L_2\rangle\langle L_1| + \eta_1|L_1\rangle\langle L_2| + \eta_2|L_2\rangle\langle L_2|, \tag{C.14}$$

where $\eta_1 = \langle R_1|G|R_2\rangle$ and $\eta_2 = \langle R_2|G|R_2\rangle$ are real and η_1 is nonzero. A Hamiltonian which is pseudo-Hermitian with respect to G_λ, $H^\dagger G_\lambda = G_\lambda H$, is

$$\begin{aligned} H &= ((a-ib)\eta_1 - c\eta_2)\,|R_1\rangle\langle L_1| + (d\eta_1 - ib\eta_2)|R_1\rangle\langle L_2| \\ &\quad + c\eta_1|R_2\rangle\langle L_1| + (a+ib)\eta_1|R_2\rangle\langle L_2|, \end{aligned} \tag{C.15}$$

with a, b, c, d being arbitrary real constants. We now set $a = \frac{\lambda\cos(x)}{\eta_1}, b = \frac{\lambda\sin(x)}{\eta_1}, c = 0, d = \frac{\cos(x)}{\eta_1}$ to get

$$\begin{aligned} H(x) &= \lambda e^{-ix}|R_1\rangle\langle L_1| + \left(\cos(x) - \frac{i\lambda\eta_2\sin(x)}{\eta_1}\right)|R_1\rangle\langle L_2| \\ &\quad + \lambda e^{+ix}|R_2\rangle\langle L_2|, \end{aligned} \tag{C.16}$$

which has eigenvalues $\lambda e^{\pm ix}$ in the relevant subspace. □

The complete proof covering r-fold degeneracies is similar and can be found in Chapter III of Ref. [28] and in Ref. [164].

C.3 CONTINUITY OF THE KIND OF EIGENVALUES

Let $H(x)$ be a parameterized pseudo-Hermitian matrix such that $G(x)H(x) = H^\dagger(x)G(x)$, where $H(x)$ and $G(x)$ are continuous functions of x, and $G(x)$ is Hermitian and invertible. Here we show that eigenvalues of $H(x)$, which are of positive (or negative) kind, retain their kind on the variation of the parameter x. For accounting purposes, an eigenvalue λ with $\operatorname{Im}\lambda > 0$ will be considered of positive kind, and if $\operatorname{Im}\lambda < 0$, it is of negative kind. We will assume the following Lemma the proof of which can be found in Ref. [28].

Lemma 3. *If $G(x)$ has p positive eigenvalues and q negative eigenvalues then $H(x)$ has p eigenvalues of positive kind and q eigenvalues of negative kind (after counting multiplicities). The converse is also true.*

A corollary of this is the following (with the proof in Ref. [28]).

Lemma 4. *Let p eigenvalues of $H(x)$ of positive kind and q eigenvalues of negative kind meet at λ. Let P be the eigenprojection operator associated with λ (which projects any vector to the root subspace of λ) [21]. Then $G(x)P$ has p positive eigenvalues and q negative eigenvalues. The converse is also true.*

We are now ready to prove the continuity of the kind of eigenvalues.

Proof. Let γ_j describe small non-intersecting disks of radius ϵ around every *distinct* eigenvalue, λ_j, of $H(0)$. We must show that for arbitrarily small $\epsilon > 0$ we can find a $\delta = \delta(\epsilon)$ such that $H(\delta)$ has the same number of eigenvalues of the first kind and the same number of eigenvalues of the second kind inside each γ_j as $H(0)$ does.

Let λ be a k-fold eigenvalue of $H(0)$. If $\operatorname{Im}\lambda > 0$ we keep ϵ small enough that the corresponding disk γ does not touch the real axis. Now, by the continuity of eigenvalues one can choose a δ small enough that $H(\delta)$ also has k eigenvalues inside γ. A similar procedure works when $\operatorname{Im}\lambda < 0$.

Now we consider the case where λ is a real k-fold eigenvalue of $H(0)$ where p eigenvalues of first kind and $q = k - p$ eigenvalues of second kind meet. Let $\Omega(0)$ and $\Omega(\delta)$ denote the sum of the root subspaces corresponding to the eigenvalues of $H(0)$ and $H(\delta)$, respectively, which lie inside γ. Let $P(0)$ and $P(\delta)$ denote the projection matrices corresponding to $\Omega(0)$ and $\Omega(\delta)$ respectively.

To define the projection matrices explicitly we make use of the resolvent $R(z) = (M - z\mathbb{I}_n)^{-1}$ of a matrix, M. The resolvent is analytic in a region that does not contain any eigenvalues of M [21]. Since λ is an isolated eigenvalue the projection matrices above can be related to the resolvent through [21, 220]

$$P(0) = \frac{i}{2\pi}\int_{\tau} dz\ (H(0) - z\mathbb{I}_n)^{-1} \tag{C.17}$$

and

$$P(\delta) = \frac{i}{2\pi} \int_\tau dz \, \left(H(\delta) - z\mathbb{I}_n\right)^{-1}, \tag{C.18}$$

where τ is the circumference of γ. We see that $P(0)$ can be made as close as desired to $P(\delta)$ provided $H(0)$ is sufficiently close to $H(\delta)$. By Lemma 4, $G(0)P(0)$ has p positive and q negative eigenvalues. By the continuity of eigenvalues, $G(\delta)P(\delta)$ also has p positive and q negative eigenvalues. Thus, by Lemma 4 again, $H(\delta)$ has p eigenvalues of positive kind and q eigenvalues of negative kind inside γ. □

This proof closely follows the one given in Chapter III of Ref. [28].

C.4 FINDING THE INTERTWINING OPERATOR

For any pseudo-Hermitian matrix, H, the intertwining operator G is not unique. Given a Hermitian matrix G_n such that $H = G_n^{-1} H^\dagger G_n$ we can construct another intertwining operator, $G_{n+1} = G_n H$ which is also Hermitian [192].

An exhaustive method to find all possible solutions G for the equation $AG = GB$ is,

$$\begin{aligned} AG &= GB, \\ (I \otimes A) \operatorname{vec} G &= (B^T \otimes I) \operatorname{vec} G, \\ (I \otimes A - B^T \otimes I) \operatorname{vec} G &= 0. \end{aligned} \tag{C.19}$$

Here $\otimes$ is the Kronecker product and $\operatorname{vec} G$ is created by arranging the entries of the matrix G in a column, $(g_{11}, g_{12}, \ldots, g_{21}, \ldots)^T$. Evidently the solutions for G form a vector space since $\operatorname{vec} G$ forms the null space of a matrix.

Our results apply to every Hermitian intertwining operator that one can find for a pseudo-Hermitian matrix H.

C.5 FORMULATION IN TERMS OF GENERALIZED $\mathcal{PT}$ SYMMETRY

Pseudo-Hermitian matrices commute with the generalized $\mathcal{PT}$ symmetry operator, $H = SH^*S^{-1} = S\mathcal{T}H\mathcal{T}^{-1}S^{-1}$ [see Eq. (5.2)]. Formulating the results of this paper in terms of S and $\mathcal{T}$ is, however, not straightforward, partly due to the complications of $\mathcal{T}$ being an antilinear operator [221].

Since we are concerned with symmetry breaking, let us assume H starts off with all real eigenvalues and no exceptional point degeneracies. We can then diagonalize H as

$$H = \sum_i \lambda_i |R_i\rangle\langle L_i|. \tag{C.20}$$

The transpose of H is $H^T = \sum_i \lambda_i |L_i\rangle^* \langle R_i|^*$. Every matrix is similar to its transpose and in this case the similarity transformation is given by,

$$H = KH^TK^{-1} \quad \text{where} \tag{C.21}$$

$$K = \sum_i e^{i\phi_i} |R_i\rangle\langle R_i|^* \quad \text{and} \tag{C.22}$$

$$K^{-1} = \sum_i e^{-i\phi_i} |L_i\rangle^* \langle L_i|. \tag{C.23}$$

Here, each $e^{i\phi_i}$ is an arbitrary phase factor. Note that Eq.(C.22) is *not* invariant under a change in absolute phase of any eigenvector, $|R_i\rangle \to e^{i\theta}|R_i\rangle$. Now

$$H = G^{-1}H^\dagger G = G^{-1}(K^{-1})^* H^* K^* G, \tag{C.24}$$

implying $S = G^{-1}(K^{-1})^*$. Now that we have expressed S in terms of G all that remains is to translate results in terms of G to S.

We note that $\tilde{H} = H^\dagger$ is pseudo-Hermitian with respect to the Hermitian matrix G^{-1}. Symmetry breaking of $H^\dagger$ is characterized by the sign of $\langle \tilde{R}_i|G^{-1}|\tilde{R}_i\rangle = \langle L_i|G^{-1}|L_i\rangle = \langle L_i|SK^*|L_i\rangle$ since the right eigenvector of $H^\dagger$ is the left eigenvector of H. In fact, symmetry breaking in $H^\dagger$ is equivalent to it occurring in H implying that the sign of $\langle L_i|SK^*|L_i\rangle$ characterizes the kind of any eigenvector $|R_i\rangle$ of H. We can simplify this further,

$$\langle L_i|SK^*|L_i\rangle = e^{-i\phi_i}\langle L_i|S|R_i\rangle^* \tag{C.25}$$

$$= e^{-i\phi_i}\langle L_i|S\mathcal{T}|R_i\rangle. \tag{C.26}$$

The arbitrary phase $e^{-i\phi_i}$ in the first equation above is problematic. Eq. (C.26) also generates additional phase factors on the transformation $|R_i\rangle \to e^{i\theta}|R_i\rangle$ since $\mathcal{T}$ is antilinear and $\mathcal{T}e^{i\theta}|R_i\rangle = e^{-i\theta}|R_i\rangle^* \neq e^{i\theta}|R_i\rangle^*$. These complications suggest that a possible formulation in terms of S and $\mathcal{T}$ may require phase fixing (gauge fixing) of the eigenvectors and we leave this to future work.

C.6 DETAILS FOR CHARACTERIZING THE POINTS OF SYMMETRY BREAKING

C.6.1 Neighborhood of a point of symmetry breaking

We start from the matrices in Eq. (5.10) and Eq. (5.11) and make an infinitesimal displacement in parameter space such that the intertwining operator changes to

$$G(\epsilon) = \begin{pmatrix} \eta_1 + \epsilon\tilde{\eta}_1 & 0 \\ 0 & -\eta_2 - \epsilon\tilde{\eta}_2 \end{pmatrix} = G_0 + \epsilon \begin{pmatrix} \tilde{\eta}_1 & 0 \\ 0 & -\tilde{\eta}_2 \end{pmatrix}, \tag{C.27}$$

where $\tilde{\eta}_1$ and $\tilde{\eta}_2$ are arbitrary real numbers and $\epsilon > 0$ is arbitrarily small. A general pseudo-Hermitian matrix with respect to $G(\epsilon)$ and which reduces to H_0 when $\epsilon = 0$ is given by $H(\epsilon) =$

$$\begin{pmatrix} \lambda + a + \epsilon(\tilde{\lambda} + \tilde{a}) & (\eta_2 + \epsilon\tilde{\eta}_2)(b + \epsilon\tilde{b})e^{i(\theta + \epsilon\tilde{\theta})} \\ -(\eta_1 + \epsilon\tilde{\eta}_1)(b + \epsilon\tilde{b})e^{-i(\theta + \epsilon\tilde{\theta})} & \lambda - a + \epsilon(\tilde{\lambda} - \tilde{a}) \end{pmatrix} \tag{C.28}$$

where $b = \frac{a}{\sqrt{\eta_1\eta_2}}$ and $\tilde{a}, \tilde{b}, \tilde{\theta}, \tilde{\lambda}$ are real. Again we see that the eigenvalues do not depend on $\theta + \epsilon\tilde{\theta}$, and are trivially shifted by $\lambda + \epsilon\tilde{\lambda}$ which controls the overall trace of the matrix. We therefore set these terms to zero without loss of generality to get

$H(\epsilon) =$

$$\begin{pmatrix} a+\epsilon\tilde{a} & (\eta_2+\epsilon\tilde{\eta}_2)\left(\frac{a}{\sqrt{\eta_1\eta_2}}+\epsilon\tilde{b}\right) \\ -(\eta_1+\epsilon\tilde{\eta}_1)\left(\frac{a}{\sqrt{\eta_1\eta_2}}+\epsilon\tilde{b}\right) & -a-\epsilon\tilde{a} \end{pmatrix}. \tag{C.29}$$

We first consider the case where $a = 0$ and H_0 had a diabolic degeneracy. In this case $H(\epsilon)$ is given by

$$H(\epsilon) = \epsilon \begin{pmatrix} \tilde{a} & (\eta_2+\epsilon\tilde{\eta}_2)\tilde{b} \\ -(\eta_1+\epsilon\tilde{\eta}_1)\tilde{b} & -\tilde{a} \end{pmatrix}. \tag{C.30}$$

This has the same form as a general pseudo-Hermitian matrix in Eq. (5.11) (with the overall trace and phase factor removed) and can therefore admit all permitted eigenvalues including from the strongly stable regions $(+,-)$ and $(-,+)$.

Now we consider the case where $a \neq 0$ and H_0 had an exceptional degeneracy. In order to prove our statement we only need to consider perturbations which create real eigenvalues. Our strategy would be to show that the larger of these eigenvalues cannot change its kind regardless of the kind of perturbation applied.

Now for any matrix, $M = \begin{pmatrix} x & y \\ z & w \end{pmatrix}$, with real eigenvalues, the larger eigenvalue is given by $\frac{x-w+\sqrt{D}}{2}$ where the discriminant, $D = (x-w)^2 + 4yz$, is positive by the assumption of real eigenvalues. The corresponding eigenvector is $|v\rangle = \begin{pmatrix} x-w+\sqrt{D} \\ 2z \end{pmatrix}$. The kind of this eigenspace with respect to $G(\epsilon)$ is given by the sign of

$$\langle v|G(\epsilon)|v\rangle = |x-w+\sqrt{D}|^2(\eta_1+\epsilon\tilde{\eta}_1) - 4|z|^2(\eta_2+\epsilon\tilde{\eta}_2). \tag{C.31}$$

On evaluating this quantity for the matrix in Eq. (C.29) and expanding in orders of ϵ, we find that the $\mathcal{O}(\epsilon^0)$ is zero since we started with a degeneracy of indefinite kind at $\epsilon = 0$. The next term is order $\mathcal{O}(\epsilon^{\frac{1}{2}})$ given by $4a\eta_1\sqrt{D}$ (one can check that

D is $\mathcal{O}(\epsilon)$). Since $\eta_1 > 0$ by assumption of invertibility of $G(\epsilon)$, $a \neq 0$ by assumption of exceptional point, and $D > 0$ by assumption of real eigenvalues, this is indeed the leading term with its sign being the same as the sign of a.

C.6.2 Topological characterization of exceptional points in the boundaries

For the purposes of this section we will consider a constant intertwining operator

$$G = \begin{pmatrix} +1 & 0 \\ 0 & -1 \end{pmatrix} = \sigma_3, \tag{C.32}$$

which is Hermitian as well as unitary and follow the procedure first laid out in Ref. [222]. The pseudo-Hermitian matrix (upto overall trace) is given by

$$H = \begin{pmatrix} a & be^{i\theta} \\ -be^{-i\theta} & -a \end{pmatrix}, \tag{C.33}$$

where a and b are real. We define the Hermitian matrix

$$\mathcal{H} = \begin{pmatrix} 0 & iH \\ -iH^\dagger & 0 \end{pmatrix}, \tag{C.34}$$

which satisfies two Hermitian chiral symmetries, $\mathcal{H}U_1 + U_1\mathcal{H} = 0$ and $\mathcal{H}U_2 + U_2\mathcal{H} = 0$. Here,

$$U_1 = \begin{pmatrix} \mathbb{I}_2 & 0 \\ 0 & -\mathbb{I}_2 \end{pmatrix} \quad \text{and} \quad U_2 = \begin{pmatrix} 0 & G \\ G & 0 \end{pmatrix} \tag{C.35}$$

are both unitary. We can block diagonalize the Hamiltonian $\mathcal{H}$ with plus and minus sectors of $U := iU_1U_2$. That is, we find a unitary transformation so that in the new basis,

$$U = \begin{pmatrix} \mathbb{I}_2 & 0 \\ 0 & -\mathbb{I}_2 \end{pmatrix} \quad \text{and} \quad \mathcal{H} := \begin{pmatrix} H_+ & 0 \\ 0 & H_- \end{pmatrix}. \tag{C.36}$$

This gives $H_+ = -i\sigma_2 H \sigma_1$ and $H_- = i\sigma_2 H \sigma_1$. The number of eigenvectors corresponding to negative eigenvalues of H_+ gives the relevant topological index—the zeroth Chern number. The eigenvalues of H_+ are $a \pm b$. Thus when $b^2 = a^2$ (at the exceptional point) the Chern number is 0 when $a > 0$ and 1 when $a < 0$.

The proof here relies on the unitary of G. When G is not unitary we may use the results from Ref. [152], which provide a method to continuously deform (in a symmetry-respecting way) any invertible Hamiltonian H into a unitary matrix U, where U is given by the unitary matrix in the polar decomposition of $H = UP$ and $P = H^\dagger H$ is positive-definite. Thus, we expect these results to hold even when G was originally only Hermitian and not unitary.

References Cited

[1] M. S. Rudner and N. H. Lindner, Nature reviews physics **2**, 229 (2020).

[2] R. El-Ganainy, K. G. Makris, M. Khajavikhan, *et al.*, Nature Physics **14**, 11 (2018).

[3] W. Kohn, Phys. Rev. **115**, 809 (1959).

[4] E. Prodan, Phys. Rev. B **73**, 035128 (2006).

[5] P. M. Chaikin, T. C. Lubensky, and T. A. Witten, *Principles of condensed matter physics*, Vol. 10 (Cambridge university press Cambridge, 1995).

[6] W. Van Saarloos, V. Vitelli, and Z. Zeravcic, *Soft Matter: Concepts, Phenomena, and Applications* (Princeton University Press, 2024).

[7] M. Kardar, *Statistical physics of fields* (Cambridge University Press, 2007).

[8] J. Cardy, *Scaling and renormalization in statistical physics*, Vol. 5 (Cambridge university press, 1996).

[9] M. C. Marchetti, J. F. Joanny, S. Ramaswamy, *et al.*, Rev. Mod. Phys. **85**, 1143 (2013).

[10] S. Shankar, A. Souslov, M. J. Bowick, *et al.*, Nature Reviews Physics **4**, 380 (2022).

[11] L. K. Davis, K. Proesmans, and E. Fodor, Phys. Rev. X **14**, 011012 (2024).

[12] X. Mao and T. C. Lubensky, Annual Review of Condensed Matter Physics **9**, 413 (2018).

[13] C. Santangelo, Bulletin of the American Physical Society (2024).

[14] P.-G. de Gennes, The Journal of Chemical Physics **48**, 2257 (1968).

[15] N. Hatano and D. R. Nelson, PRL **77**, 570 (1996).

[16] D. Z. Rocklin, S. Tan, and P. M. Goldbart, Phys. Rev. B **86**, 165421 (2012).

[17] C. L. Kane and T. C. Lubensky, Nature Physics **10**, 39 (2014).

[18] R. Süsstrunk and S. D. Huber, Proceedings of the National Academy of Sciences, U.S.A. **113**, E4767 (2016).

[19] E. Tang, J. Agudo-Canalejo, and R. Golestanian, Physical Review X **11**, 031015 (2021).

[20] T. Kitagawa, E. Berg, M. Rudner, and E. Demler, Phys. Rev. B **82**, 235114 (2010).

[21] Y. Ashida, Z. Gong, and M. Ueda, Advances in Physics **69**, 249 (2020).

[22] I. I. Arkhipov, A. Miranowicz, F. Minganti, *et al.*, Nature communications **14**, 2076 (2023).

[23] C.-K. Chiu, J. C. Y. Teo, A. P. Schnyder, and S. Ryu, Rev. Mod. Phys. **88**, 035005 (2016).

[24] K. Kawabata, K. Shiozaki, M. Ueda, and M. Sato, Phys. Rev. X **9**, 041015 (2019).

[25] C. C. Wojcik, X.-Q. Sun, T. Bzdušek, and S. Fan, Phys. Rev. B **101**, 205417 (2020).

[26] H. C. Po, H. Watanabe, and A. Vishwanath, Phys. Rev. Lett. **121**, 126402 (2018).

[27] R. Zhang, H. Qin, and J. Xiao, Journal of Mathematical Physics **61**, 012101 (2020).

[28] V. Yakubovich, V. Starzhinskii, and G. Schmidt, *On Linear Differential Equations with Periodic Coefficients*, Vol. 1 (Wiley, London, 1976) pp. 222–222.

[29] A. Melkani, Phys. Rev. Res. **5**, 023035 (2023).

[30] D. R. Nelson and V. M. Vinokur, Phys. Rev. B **48**, 13060 (1993).

[31] N. Bartelt, T. Einstein, and E. D. Williams, Surface Science **240**, L591 (1990).

[32] D. Z. Rocklin, *Directed-polymer systems explored via their quantum analogs*, Ph.D. thesis (2013).

[33] M. W. Matsen, Self-consistent field theory and its applications, in *Soft Matter: Polymer Melts and Mixtures* (John Wiley & Sons, New York NY, 2005) Chap. 2, pp. 87–178.

[34] P. W. Anderson, Phys. Rev. **109**, 1492 (1958).

[35] V. Heine, Proceedings of the Physical Society **81**, 300 (1963).

[36] F. Zangeneh-Nejad and R. Fleury, Reviews in Physics **4**, 100031 (2019).

[37] R. Fleury, D. L. Sounas, C. F. Sieck, *et al.*, Science **343**, 516 (2014).

[38] H. Nassar, B. Yousefzadeh, R. Fleury, *et al.*, Nature Reviews Materials , 1 (2020).

[39] L. Landau and E. Lifshitz, *Mechanics: Volume 1*, v. 1 (Elsevier Science, 1982).

[40] Q. Gao and Q. Niu, Phys. Rev. Lett. **127**, 036401 (2021).

[41] Y. Peng, Phys. Rev. Lett. **128**, 186802 (2022).

[42] A. Melkani, A. Patapoff, and J. Paulose, Phys. Rev. E **107**, 014501 (2023).

[43] C. M. Bender, Reports on Progress in Physics **70**, 947 (2007).

[44] H.-K. Lau and A. A. Clerk, Nature communications **9**, 1 (2018).

[45] S. Malzard, C. Poli, and H. Schomerus, Phys. Rev. Lett. **115**, 200402 (2015).

[46] J. Schindler, Z. Lin, J. M. Lee, *et al.*, Journal of Physics A: Mathematical and Theoretical **45**, 444029 (2012).

[47] R. Thevamaran, R. M. Branscomb, E. Makri, *et al.*, The Journal of the Acoustical Society of America **146**, 863 (2019).

[48] K. Sone, Y. Ashida, and T. Sagawa, Nature Communications **11**, 5745 (2020).

[49] M. I. N. Rosa and M. Ruzzene, New Journal of Physics **22**, 053004 (2020).

[50] J. Li, A. K. Harter, J. Liu, *et al.*, Nature communications **10**, 855 (2019).

[51] D. R. Nelson and N. M. Shnerb, Physical Review E **58**, 1383 (1998).

[52] D. S. Borgnia, A. J. Kruchkov, and R.-J. Slager, Physical Review Letters **124**, 056802 (2020).

[53] N. Okuma, K. Kawabata, K. Shiozaki, and M. Sato, Phys. Rev. Lett. **124**, 086801 (2020).

[54] S. Yao and Z. Wang, Phys. Rev. Lett. **121**, 086803 (2018).

[55] Z. Gong, Y. Ashida, K. Kawabata, *et al.*, Phys. Rev. X **8**, 031079 (2018).

[56] C.-H. Liu and S. Chen, Physical Review B **100**, 144106 (2019).

[57] H. Shen, B. Zhen, and L. Fu, Phys. Rev. Lett. **120**, 146402 (2018).

[58] W. D. Heiss, Journal of Physics A: Mathematical and Theoretical **45**, 444016 (2012).

[59] A. Ghatak, M. Brandenbourger, J. van Wezel, and C. Coulais, Proceedings of the National Academy of Sciences **117**, 29561 (2020).

[60] D. Zhou and J. Zhang, Phys. Rev. Research **2**, 023173 (2020).

[61] C. Scheibner, W. T. M. Irvine, and V. Vitelli, Physical Review Letters **125**, 118001 (2020).

[62] G. Shmuel and N. Moiseyev, Physical Review Applied **13**, 024074 (2020).

[63] H. Ramezani, T. Kottos, V. Kovanis, and D. N. Christodoulides, Phys. Rev. A **85**, 013818 (2012).

[64] D. A. Abanin, E. Altman, I. Bloch, and M. Serbyn, Rev. Mod. Phys. **91**, 021001 (2019).

[65] N. Hatano and D. R. Nelson, Physical Review B **56**, 8651 (1997).

[66] N. Hatano and D. R. Nelson, Phys. Rev. B **58**, 8384 (1998).

[67] A. Amir, N. Hatano, and D. R. Nelson, Phys. Rev. E **93**, 042310 (2016).

[68] D. R. Nelson and P. Le Doussal, Phys. Rev. B **42**, 10113 (1990).

[69] T. Hwa, D. R. Nelson, and V. M. Vinokur, Phys. Rev. B **48**, 1167 (1993).

[70] K. Kim and D. R. Nelson, Phys. Rev. B **64**, 054508 (2001).

[71] I. Affleck, W. Hofstetter, D. R. Nelson, and U. Schollwöck, Journal of Statistical Mechanics: Theory and Experiment **2004**, P10003 (2004).

[72] G. Refael, W. Hofstetter, and D. R. Nelson, Phys. Rev. B **74**, 174520 (2006).

[73] M. Lankhorst, N. Poccia, M. P. Stehno, *et al.*, Phys. Rev. B **97**, 020504(R) (2018).

[74] R. Hamazaki, K. Kawabata, and M. Ueda, Physical Review Letters **123**, 090603 (2019).

[75] A. Panda and S. Banerjee, Physical Review B **101**, 184201 (2020).

[76] T. Fukui and N. Kawakami, Phys. Rev. B **58**, 16051 (1998).

[77] F. Hébert, M. Schram, R. T. Scalettar, *et al.*, The European Physical Journal B **79**, 465 (2011).

[78] A. Krajenbrink, P. Le Doussal, and N. O'Connell, Phys. Rev. E **103**, 042120 (2021).

[79] A. M. Jayannavar and N. Kumar, Phys. Rev. Lett. **48**, 553 (1982).

[80] M. P. A. Fisher, P. B. Weichman, G. Grinstein, and D. S. Fisher, Phys. Rev. B **40**, 546 (1989).

[81] R. A. Lehrer and D. R. Nelson, Phys. Rev. B **58**, 12385 (1998).

[82] C. A. Bolle, V. Aksyuk, F. Pardo, *et al.*, Nature **399**, 43 (1999).

[83] Z. Dogic, J. Zhang, a. W. C. Lau, *et al.*, Physical Review Letters **92**, 125503 (2004).

[84] R. P. Pedro, J. Paulose, A. Souslov, *et al.*, PRL **122**, 118001 (2019).

[85] J. A. Anderson, J. Glaser, and S. C. Glotzer, Computational Materials Science **173**, 109363 (2020).

[86] D. J. Luitz and Y. B. Lev, Annalen der Physik **529**, 1600350 (2017).

[87] R. Palmer, Advances in Physics **31**, 669 (1982).

[88] S. F. Edwards, Proceedings of the Physical Society **85**, 613 (1965).

[89] P. G. D. Gennes, Reports on Progress in Physics **32**, 304 (1969).

[90] G. H. Fredrickson, V. Ganesan, and F. Drolet, Macromolecules **35**, 16 (2002).

[91] M. Girardeau, Journal of Mathematical Physics **1**, 516 (1960).

[92] F. W. Wiegel, *Introduction to Path-integral Methods in Physics and Polymer Science* (World Scientific, Singapore, 1986).

[93] P.-G. De Gennes and P.-G. Gennes, *Scaling concepts in polymer physics* (Cornell University Press, Ithaca, NY, 1979).

[94] Y. Aharonov and D. Bohm, Phys. Rev. **115**, 485 (1959).

[95] J. B. Pendry and F. Forstmann, Journal of Physics C: Solid State Physics **3**, 59 (1970).

[96] J. E. Inglesfield, Reports on Progress in Physics **45**, 223 (1982).

[97] K. Yokomizo and S. Murakami, Phys. Rev. Lett. **123**, 066404 (2019).

[98] C. Brouder, G. Panati, M. Calandra, *et al.*, Phys. Rev. Lett. **98**, 046402 (2007).

[99] W. Kohn, Physical Review **133**, A171 (1964).

[100] K. Kawabata and S. Ryu, Phys. Rev. Lett. **126**, 166801 (2021).

[101] M. T. Ahari, G. Ortiz, and B. Seradjeh, American Journal of Physics **84**, 858 (2016).

[102] A. Z. Capri, American Journal of Physics **45**, 823 (1977).

[103] S. Goedecker, Rev. Mod. Phys. **71**, 1085 (1999).

[104] S. Ismail-Beigi and T. A. Arias, Phys. Rev. Lett. **82**, 2127 (1999).

[105] L. He and D. Vanderbilt, Phys. Rev. Lett. **86**, 5341 (2001).

[106] D. M. Basko, I. L. Aleiner, and B. L. Altshuler, Annals of Physics **321**, 1126 (2006).

[107] H. A. Fertig and S. Das Sarma, Physical Review B **42**, 1448 (1990).

[108] S. Roy, T. Mishra, B. Tanatar, and S. Basu, Phys. Rev. Lett. **126**, 106803 (2021).

[109] A. Padhan, M. K. Giri, S. Mondal, and T. Mishra, Phys. Rev. B **105**, L220201 (2022).

[110] P. Reimann and R. Eichhorn, Phys. Rev. Lett. **101**, 180601 (2008).

[111] S. Li, M. Li, Y. Gao, and P. Tong, Phys. Rev. B **105**, 104201 (2022).

[112] P. A. Kuchment, *Floquet Theory for Partial Differential Equations*, Vol. 60 (Birkhäuser, Switzerland, 2012).

[113] D. J. Thouless, Phys. Rev. B **27**, 6083 (1983).

[114] M. Bukov, L. D'Alessio, and A. Polkovnikov, Advances in Physics **64**, 139 (2015).

[115] S. Longhi, Journal of Physics A: Mathematical and Theoretical **50**, 505201 (2017).

[116] M. Fruchart, R. Hanai, P. B. Littlewood, and V. Vitelli, Nature **592**, 363 (2021).

[117] H. Jiang, L.-J. Lang, C. Yang, *et al.*, Phys. Rev. B **100**, 054301 (2019).

[118] T. Liu, H. Guo, Y. Pu, and S. Longhi, Physical Review B **102**, 024205 (2020).

[119] S.-B. Zhang, M. M. Denner, T. Bzdušek, *et al.*, Phys. Rev. B **106**, L121102 (2022).

[120] S. Heußen, C. D. White, and G. Refael, Phys. Rev. B **103**, 064201 (2021).

[121] A. Souslov, D. Z. Rocklin, and P. M. Goldbart, Phys. Rev. Lett. **111**, 096401 (2013).

[122] N. M. Shnerb and D. R. Nelson, Physical Review Letters **80**, 5172 (1998).

[123] R. Sarkar, S. S. Hegde, and A. Narayan, Phys. Rev. B **106**, 014207 (2022).

[124] G. Karapetrov, J. Fedor, M. Iavarone, *et al.*, Phys. Rev. Lett. **95**, 167002 (2005).

[125] L. T. Haag, G. Zechner, W. Lang, *et al.*, Physica C: Superconductivity and its Applications **503**, 75 (2014).

[126] A. McMullen, M. Holmes-Cerfon, F. Sciortino, *et al.*, Phys. Rev. Lett. **121**, 138002 (2018).

[127] S. G. Stuij, A. Biebricher, Z. Gong, *et al.*, Physical Review Materials **6**, 035603 (2022).

[128] Z. Liu, Z. Yang, X. Chen, *et al.*, JACS Au **1**, 79 (2020).

[129] A. Melkani and J. Paulose, Phys. Rev. E **110**, 015003 (2024).

[130] W. Louisell, *Coupled Mode and Parametric Electronics* (John Wiley & Sons, 1960).

[131] J. D. Huerta-Morales, M. A. Quiroz-Juárez, Y. N. Joglekar, and R. d. J. León-Montiel, Phys. Rev. A **107**, 042219 (2023).

[132] D. Rugar and P. Grütter, Physical Review Letters **67**, 699 (1991).

[133] J. P. Mathew, R. N. Patel, A. Borah, *et al.*, Nature Nanotechnology **11**, 747 (2016).

[134] G. Trainiti, Y. Xia, J. Marconi, *et al.*, Phys. Rev. Lett. **122**, 124301 (2019).

[135] T. L. Heugel, M. Oscity, A. Eichler, *et al.*, Physical Review Letters **123**, 124301 (2019).

[136] N. Y. Yao, C. Nayak, L. Balents, and M. P. Zaletel, Nature Physics **16**, 438 (2020).

[137] Z. Wang, A. Marandi, K. Wen, *et al.*, Phys. Rev. A **88**, 063853 (2013).

[138] T. Inagaki, K. Inaba, R. Hamerly, *et al.*, Nature Photonics **10**, 415 (2016).

[139] L. Bello, M. Calvanese Strinati, E. G. Dalla Torre, and A. Pe'er, Phys. Rev. Lett. **123**, 083901 (2019).

[140] A. Roy and M. Devoret, Comptes Rendus Physique Quantum Microwaves / Micro-ondes Quantiques, **17**, 740 (2016).

[141] E. Buks and M. Roukes, Journal of Microelectromechanical Systems **11**, 802 (2002).

[142] M. H. Matheny, J. Emenheiser, W. Fon, *et al.*, Science **363**, eaav7932 (2019).

[143] B. L. Kim, C. Chong, S. Hajarolasvadi, *et al.*, Physical Review E **107**, 034211 (2023).

[144] Y.-F. Wang, Y.-Z. Wang, B. Wu, *et al.*, Applied Mechanics Reviews **72**, 10.1115/1.4046222 (2020).

[145] W. Magnus and S. Winkler, *Hill's Equation*, Interscience Tracts in Pure and Applied Mathematics (Interscience Publishers, 1966).

[146] L. Ruby, American Journal of Physics **64**, 39 (1996).

[147] I. Kovacic, R. Rand, and S. Mohamed Sah, Applied Mechanics Reviews **70**, 10.1115/1.4039144 (2018).

[148] H. Broer and M. Levi, Archive for rational mechanics and analysis **131**, 225 (1995).

[149] G. Salerno, T. Ozawa, H. M. Price, and I. Carusotto, Physical Review B **93**, 085105 (2016), 1510.04697 .

[150] M. Calvanese Strinati, L. Bello, A. Pe'er, and E. G. Dalla Torre, Phys. Rev. A **100**, 023835 (2019).

[151] N. Kruss and J. Paulose, Phys. Rev. Appl. **17**, 024020 (2022).

[152] H. Zhou and J. Y. Lee, Phys. Rev. B **99**, 235112 (2019).

[153] A. Mostafazadeh, Journal of Mathematical Physics **43**, 205 (2002).

[154] S. Xu and C. Wu, Phys. Rev. Lett. **120**, 096401 (2018).

[155] E. Galiffi, P. A. Huidobro, and J. B. Pendry, Physical Review Letters **123**, 206101 (2019).

[156] A. Blaikie, D. Miller, and B. J. Alemán, Nature Communications **10**, 1 (2019).

[157] J. C. Budich and E. J. Bergholtz, Phys. Rev. Lett. **125**, 180403 (2020).

[158] J. Wiersig, Phys. Rev. Research **4**, 033179 (2022).

[159] C. M. Bender, M. Gianfreda, i. m. c. K. Özdemir, *et al.*, Phys. Rev. A **88**, 062111 (2013).

[160] M. Oudich, Physical Review Research **1**, 10.1103/PhysRevResearch.1.033069 (2019).

[161] T. Yoshida and Y. Hatsugai, Phys. Rev. B **100**, 054109 (2019).

[162] C. M. Bender, P. E. Dorey, C. Dunning, *et al.*, *PT Symmetry* (World Scientific Europe, 2019).

[163] A. Wang, Z. Meng, and C. Q. Chen, Science Advances **9**, eadf7299 (2023).

[164] W. A. Coppel and A. Howe, Journal of the Australian Mathematical Society **5**, 169–195 (1965).

[165] C.-H. Liu, H. Hu, and S. Chen, Phys. Rev. B **105**, 214305 (2022).

[166] J. E. Howard and R. S. MacKay, Journal of Mathematical Physics **28**, 1036 (1987).

[167] H. Wu and J.-H. An, Phys. Rev. B **102**, 041119 (2020).

[168] J. Yu, R.-X. Zhang, and Z.-D. Song, Nature Communications **12**, 5985 (2021).

[169] M. Zhang, W. Sweeney, C. W. Hsu, *et al.*, Phys. Rev. Lett. **123**, 180501 (2019).

[170] G. Xu, X. Zhou, Y. Li, *et al.*, Phys. Rev. Lett. **130**, 266303 (2023).

[171] L. Ge and A. D. Stone, Phys. Rev. X **4**, 031011 (2014).

[172] K. L. Turner, S. A. Miller, P. G. Hartwell, *et al.*, Nature **396**, 149 (1998).

[173] B. M. Goldsberry, S. P. Wallen, and M. R. Haberman, Physical Review Applied **17**, 034050 (2022).

[174] A. Metelmann and A. A. Clerk, Physical Review X **5**, 021025 (2015).

[175] R. Lin, T. Tai, L. Li, and C. H. Lee, Frontiers of Physics **18**, 53605 (2023).

[176] H. Gao, H. Xue, Z. Gu, *et al.*, Phys. Rev. B **106**, 134112 (2022).

[177] F. Grossmann, T. Dittrich, P. Jung, and P. Hänggi, Phys. Rev. Lett. **67**, 516 (1991).

[178] H. P. Breuer, K. Dietz, and M. Holthaus, Zeitschrift für Physik D Atoms, Molecules and Clusters **8**, 349 (1988).

[179] R. Adlakha and M. Nouh, Smart Materials and Structures **32**, 074001 (2023).

[180] X. Wen, X. Zhu, A. Fan, *et al.*, Communications physics **5**, 18 (2022).

[181] T. T. Koutserimpas and R. Fleury, Phys. Rev. Lett. **120**, 087401 (2018).

[182] C. Coulais, R. Fleury, and J. van Wezel, Nature Physics **17**, 9 (2021).

[183] M. Brandenbourger, C. Scheibner, J. Veenstra, *et al.*, Limit cycles turn active matter into robots (2022), arXiv:2108.08837 [cond-mat.soft] .

[184] J. Arkinstall, M. H. Teimourpour, L. Feng, *et al.*, Phys. Rev. B **95**, 165109 (2017).

[185] A. M. Marques, L. Madail, and R. G. Dias, Phys. Rev. B **103**, 235425 (2021).

[186] A. Mostafazadeh, Int. J. Geom. Methods Mod. Phys. **07**, 1191 (2010).

[187] S. Shankar, M. J. Bowick, and M. C. Marchetti, Phys. Rev. X **7**, 031039 (2017).

[188] K. Kawabata, S. Higashikawa, Z. Gong, *et al.*, Nature communications **10**, 1 (2019).

[189] Ş. K. Özdemir, S. Rotter, F. Nori, and L. Yang, Nature materials **18**, 783 (2019).

[190] C. M. Bender, Contemporary Physics **46**, 277 (2005).

[191] W. Wang and Z. Ma, Phys. Rev. B **106**, 115306 (2022).

[192] F. Ruzicka, K. S. Agarwal, and Y. N. Joglekar, Journal of Physics: Conference Series **2038**, 012021 (2021).

[193] K. Kawabata, T. Bessho, and M. Sato, Phys. Rev. Lett. **123**, 066405 (2019).

[194] H. Hu, S. Sun, and S. Chen, Phys. Rev. Research **4**, L022064 (2022).

[195] H. Langer and C. Tretter, Czechoslovak Journal of Physics **54**, 1113 (2004).

[196] R. Zhang, H. Qin, R. C. Davidson, *et al.*, Physics of Plasmas **23**, 072111 (2016).

[197] Y. Chang, Y. Long, and J. Wang, Annales de l'Institut Henri Poincaré C **36**, 75 (2019).

[198] K. Mochizuki, K. Mizuta, and N. Kawakami, Phys. Rev. Res. **3**, 043112 (2021).

[199] V. P. Flynn, E. Cobanera, and L. Viola, Europhysics Letters **131**, 40006 (2020).

[200] V. Peano and H. Schulz-Baldes, Journal of Mathematical Physics **59**, 031901 (2018), https://doi.org/10.1063/1.5002094 .

[201] V. P. Flynn, E. Cobanera, and L. Viola, New Journal of Physics **22**, 083004 (2020).

[202] O. Mustafa and S. H. Mazharimousavi, International Journal of Theoretical Physics **47**, 446 (2008).

[203] A. Mostafazadeh, Journal of Physics A: Mathematical and General **36**, 7081 (2003).

[204] A. P. Seyranian, O. N. Kirillov, and A. A. Mailybaev, Journal of Physics A: Mathematical and General **38**, 1723 (2005).

[205] P. Delplace, T. Yoshida, and Y. Hatsugai, Phys. Rev. Lett. **127**, 186602 (2021).

[206] T. Yoshida, R. Peters, N. Kawakami, and Y. Hatsugai, Progress of Theoretical and Experimental Physics **2020**, 12A109 (2020).

[207] P. Woit, Introduction and overview, in *Quantum Theory, Groups and Representations: An Introduction* (Springer International Publishing, Cham, 2017) pp. 1–14.

[208] W. Xiong, Z. Li, Y. Song, *et al.*, Phys. Rev. A **104**, 063508 (2021).

[209] W. Xiong, Z. Li, G.-Q. Zhang, *et al.*, Phys. Rev. A **106**, 033518 (2022).

[210] L. Li, S. Mu, C. H. Lee, and J. Gong, Nature communications **12**, 5294 (2021).

[211] P. Zhang and Y. Chen, Phys. Rev. B **105**, L241106 (2022).

[212] C. Weis, M. Fruchart, R. Hanai, *et al.*, Coalescence of attractors: Exceptional points in non-linear dynamical systems, arXiv:2207.11667 .

[213] J. C. Budich, J. Carlström, F. K. Kunst, and E. J. Bergholtz, Phys. Rev. B **99**, 041406(R) (2019).

[214] M. Stålhammar and E. J. Bergholtz, Phys. Rev. B **104**, L201104 (2021).

[215] T. Tai and C. H. Lee, Phys. Rev. B **107**, L220301 (2023).

[216] Z. Xiao, K. Kawabata, X. Luo, *et al.*, Phys. Rev. Res. **4**, 043196 (2022).

[217] F. L. Metz, I. Neri, and T. Rogers, Journal of Physics A: Mathematical and Theoretical **52**, 434003 (2019).

[218] P. Giannozzi *et al.*, Journal of Physics: Condensed Matter **21**, 395502 (2009).

[219] A. Smogunov, A. Dal Corso, and E. Tosatti, Phys. Rev. B **70**, 045417 (2004).

[220] T. Kato, Perturbation theory in a finite-dimensional space, in *Perturbation theory for linear operators* (Springer, Berlin, 1966) pp. 62–126.

[221] A. Uhlmann, Science China Physics, Mechanics & Astronomy **59**, 1 (2016).

[222] T. Yoshida, R. Peters, N. Kawakami, and Y. Hatsugai, Phys. Rev. B **99**, 121101 (2019)